TU Delft

Delft University of Technology

Document Version
Final published version

Licence
CC BY

Citation (APA)
Castino, F. (2026). *Eco-efficient aircraft trajectories to reduce aviation non-CO_2 climate effects under varying atmospheric conditions.* [Dissertation (TU Delft), Delft University of Technology]. https://doi.org/10.4233/uuid:b0b6fcf1-99b9-4e2c-bee9-f9f8fc417e9e

Important note
To cite this publication, please use the final published version (if applicable).
Please check the document version above.

Copyright
In case the licence states “Dutch Copyright Act (Article 25fa)”, this publication was made available Green Open Access via the TU Delft Institutional Repository pursuant to Dutch Copyright Act (Article 25fa, the Taverne amendment). This provision does not affect copyright ownership.
Unless copyright is transferred by contract or statute, it remains with the copyright holder.

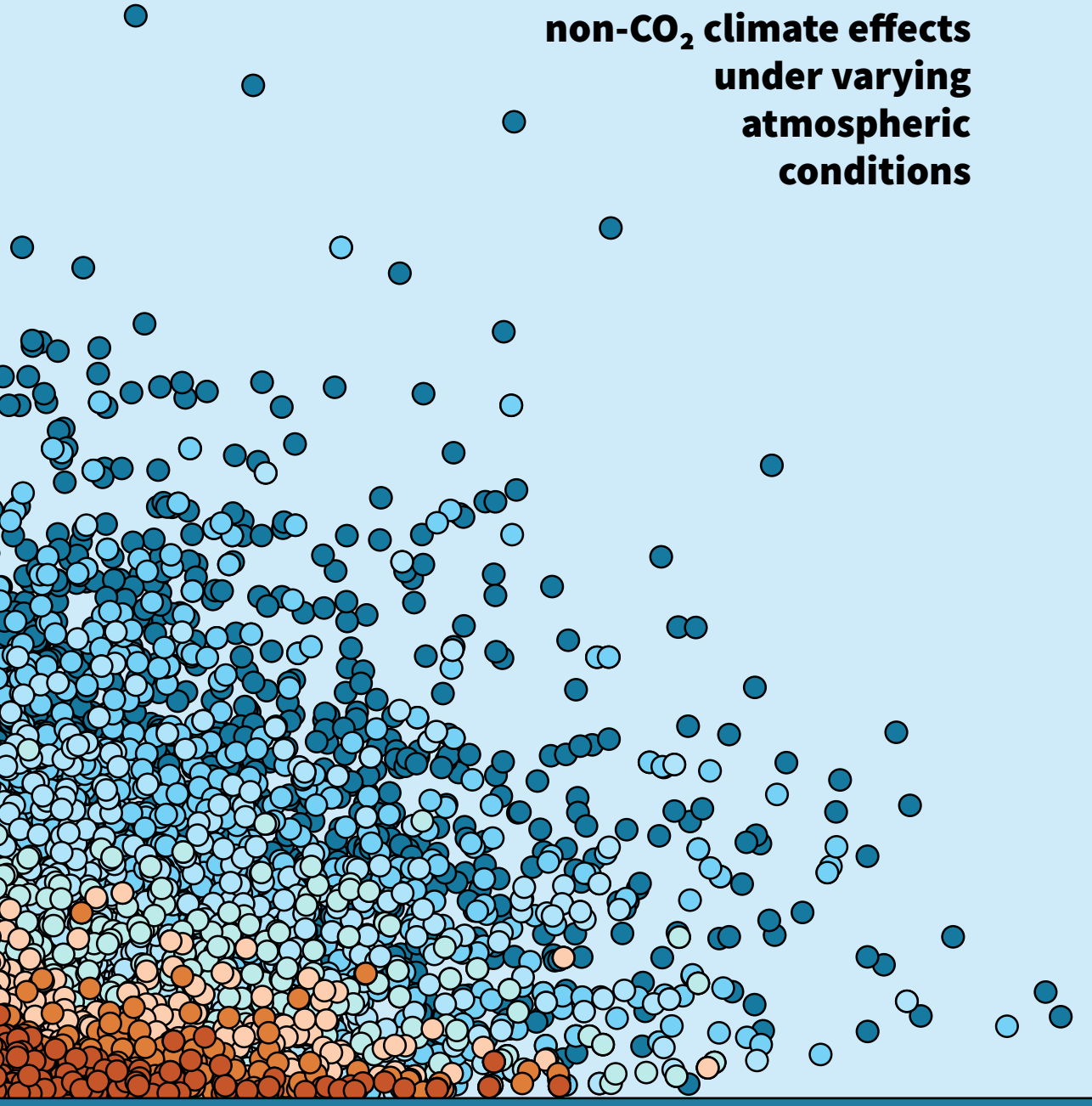
Sharing and reuse
Other than for strictly personal use, it is not permitted to download, forward or distribute the text or part of it, without the consent of the author(s) and/or copyright holder(s), unless the work is under an open content license such as Creative Commons.

Takedown policy
Please contact us and provide details if you believe this document breaches copyrights.
We will remove access to the work immediately and investigate your claim.

This work is downloaded from Delft University of Technology.

ECO-EFFICIENT AIRCRAFT TRAJECTORIES

to reduce aviation non-CO_2 climate effects under varying atmospheric conditions



Federica Castino

Eco-efficient aircraft trajectories to reduce aviation non-CO_2 climate effects under varying atmospheric conditions

Eco-efficient aircraft trajectories to reduce aviation non-CO_2 climate effects under varying atmospheric conditions

Dissertation

for the purpose of obtaining the degree of doctor
at Delft University of Technology
by the authority of the Rector Magnificus, prof. dr. ir. H. Bijl,
Chair of the Board for Doctorates
to be defended publicly on
Friday, 4 September 2026 at 10:00.

by

Federica CASTINO

This dissertation has been approved by the (co)promotors.

Composition of the doctoral committee:

Rector Magnificus,	chairperson
Prof. dr. V. Grewe,	Delft University of Technology, *promotor*
Dr. F. Yin,	Delft University of Technology, *copromotor*
Independent members:	
Prof. dr. L. L. A. Vermeersen,	Delft University of Technology
Prof. dr. A. P. Siebesma,	Delft University of Technology
Prof. dr. M. F. Soler,	Universidad Carlos III de Madrid
Dr. F. Linke,	Deutsches Zentrum für Luft- und Raumfahrt
Prof. dr. A. Gangoli Rao,	Delft University of Technology, *reserve member*

The work in the thesis has been supported by the SESAR Joint Undertaking under grant number 891317 (FlyATM4E) and by the Horizon Europe Research and Innovation Actions programme under grant number 101056885 (BeCoM).



Keywords:	aviation climate impact, non-CO_2 effects, aircraft trajectory optimization, decision-making strategies, contrails, nitrogen oxides
Printed by:	Proefschriftspecialist
Cover:	Visualization of data presented in Chapter 4, Figure 4.6.
Style:	TU Delft House Style, with modifications by Moritz Beller https://github.com/Inventitech/phd-thesis-template

An electronic version of this dissertation is available at http://repository.tudelft.nl/.

Alla mia famiglia,
per il supporto incondizionato e costante.

Contents

Summary **xi**

Samenvatting **xiii**

1 Introduction **1**
1.1 Overview and research gap. . . . 1
1.2 Objective and research questions. . . . 4
1.3 Thesis structure 4

2 Background **7**
2.1 Atmospheric composition and structure 7
2.1.1 Radiative forcing 9
2.2 Climate effects of aircraft emissions 10
2.3 Contrail and contrail cirrus. . . . 12
2.3.1 Formation of contrail and contrail cirrus 12
2.3.2 Radiative forcing of persistent contrails 15
2.4 NO_x emissions 16
2.5 Aircraft trajectory optimization as a climate impact mitigation strategy . . 18

3 Methodology **21**
3.1 Introduction to EMAC 22
3.2 AirTraf submodel 23
3.3 CONTRAIL submodel 26
3.3.1 Ice supersaturated regions and potential contrail coverage 26
3.3.2 Resulting frequency and spatio-temporal variability of ISSRs. . . . 31
3.4 The ACCF submodel 32
3.4.1 Datasets used for the aCCFs derivation. . . . 32
3.4.2 Development of the algorithmic Climate Change Functions (aCCFs v1.0) 34
3.4.3 The EMAC submodel ACCF v1.0 36
3.5 Summary. . . . 39

4 Model development: SolFinder 1.0 decision-making tool and its application in AirTraf 3.0 **41**
4.1 Introduction 42
4.2 Multi-objective optimization with AirTraf 43
4.3 SolFinder module. . . . 44
4.3.1 VIKOR method 45
4.3.2 Strategy using VIKOR method to identify eco-efficient trajectories . 47
4.3.3 Sensitivity of VIKOR parameterization 49

4.3.4 Target percentage change in one of the objective functions. 51
4.3.5 Hybrid option: VIKOR method with target percentage change in one of the objectives 51
4.3.6 Selecting one extreme of Pareto-optimal set 53
4.4 Application of decision-making method to analyse trajectories' variability along Pareto-front 53
4.4.1 Simulations set-up 53
4.4.2 Results 55
4.5 Discussion 65
4.6 Summary. 67

5 Mitigation potential of contrail avoidance and its dependency on weather patterns 69
5.1 Introduction 69
5.2 Methods 71
5.2.1 Model overview 71
5.2.2 Simulations setup 72
5.2.3 Weather pattern classification 74
5.3 Results 77
5.3.1 Seasonality of contrail avoidance. 77
5.3.2 Dependency of contrail avoidance on typical winter weather patterns 79
5.3.3 Potential contrail cirrus coverage under different weather patterns. 81
5.3.4 Properties of optimized trajectories under different weather patterns 83
5.4 Discussion 84
5.5 Conclusions 87

6 Seasonal variability of aircraft trajectories reducing NO_x-climate impacts 89
6.1 Introduction 90
6.2 Methods 90
6.2.1 Base model. 90
6.2.2 Sub-model AirTraf 90
6.2.3 Routing optimization strategies 91
6.3 Results 92
6.3.1 Mean flight altitudes and horizontal paths 92
6.3.2 Time-evolution of changes in fuel use and flight time 94
6.3.3 Changes in climate impact of NO_x emissions. 95
6.3.4 Relation between climate benefits and economic costs 98
6.4 Discussion 99
6.5 Conclusion. 99

7 Discussion 101
7.1 Quantifying aviation non-CO_2 effects with fast assessment models. 101
7.2 Multi-objective optimization of aircraft trajectories. 104
7.3 Trade-offs between reducing CO_2 and non-CO_2 effects. 105

8 Conclusions **107**

A Appendix A: Supplementary material on SolFinder v1.0 **113**
A.1 Background information 114
A.2 Installation 114
A.3 Get started 114
A.4 Example application 115

B Appendix B: Supplementary material on the analysis of contrail avoidance mitigation potential and its dependency on weather patterns **117**
B.1 Comparison of weather pattern type frequencies 118
B.2 Seasonality of potential contrail coverage over Europe 118
B.3 Weather pattern analysis over the meteorological winter, DJF (December, January, February) 119
B.4 Vertical profiles of potential contrail coverage under different weather pattern classes 121
B.5 Vertical profiles of IAGOS data 121

Acknowledgments **139**

Curriculum Vitæ **143**

List of Publications **145**

Summary

Global mobility offers significant benefits to our society. It enables solutions to reduce inequalities, for example, providing access to high quality education and work opportunities. From this point of view, aviation plays a crucial role in the social and economic development. However, only a small fraction of the global population currently accounts for more than half of the total civil aviation emissions, which negatively affects local air quality and the Earth's climate. In recent years, there has been an increasing pressure to mitigate the environmental damages from aviation, mainly by limiting its carbon dioxide (CO_2) emissions. This greenhouse gas is responsible for long-term warming effects, as it remains in the atmosphere for years to millennia.

However, carbon dioxide is only one of the species emitted by aircraft. In fact, other climate effects of aviation, the so-called *non-CO_2 effects*, are also expected to significantly contribute to the climate impact of a flight. These effects include the formation of condensation trails (contrails) behind the aircraft, and the variations in the concentrations of atmospheric ozone (O_3) and methane (CH_4) due to nitrogen oxides (NO_x) emissions. The net climate impact caused by these non-CO_2 effects of aviation is highly dependent on the background atmospheric conditions. For example, contrails persist in the atmosphere for more than a few minutes only in the presence of the right ambient conditions, i.e. if ice-supersaturation occurs. Therefore, the net climate impact of a flight can be reduced not only with improvements in the characteristics of aircraft and engines, but also by optimizing aircraft trajectories to avoid regions of the atmosphere where non-CO_2 effects of aviation are particularly strong.

Considering the mitigation potential of operational measures, the main objective of this doctoral thesis is to define, identify, and analyse *"eco-efficient"* aircraft trajectories, which lead to significant climate impact reductions at small penalties in terms of additional fuel consumption and flight time. In particular, the aim is to improve the understanding of their variability over the range of natural atmospheric variability, considering a large number of weather conditions.

The first phase of this doctoral research focused on the development of a strategy to identify eco-efficient aircraft trajectories within long-term model simulations. This resulted in the implementation of a decision-making tool, SolFinder 1.0, within the air traffic optimizer AirTraf 3.0, which is coupled with the ECHAM/MESSy Atmospheric Chemistry (EMAC) model. SolFinder includes different strategies to select a single option among a set of equally optimal alternatives, i.e. a Pareto set. This selection takes into account high-level information provided by the decision maker to rank the solutions of a multi-objective optimization problem, e.g. minimizing fuel consumption while limiting contrail formation along the flight.

The properties of eco-efficient trajectories under varying atmospheric conditions are then analysed conducting long-term simulations, optimizing 100 flights over the North Atlantic on every day from 1 December 2015 to 31 December 2018. Various routing

options are compared. Firstly, this thesis analyses the influence of meteorological variability on trajectory optimization strategies that reduce contrail formation with limited changes in fuel use. This work offers insights on which conditions are linked to high mitigation potential from contrail avoidance, in order to identify them in advance. Focusing on winter days, a well-established weather pattern classification based on the North Atlantic Oscillation (NAO) and East Atlantic (EA) patterns is applied to distinguish the simulated days into five classes. One of these average weather patterns, showing a weak and tilted jet stream, is found to be linked to the highest ratio between benefit (contrail reduction) and penalties (extra fuel burnt).

Secondly, the relation between NO_x-climate impacts and routing strategies is explored under varying meteorological conditions. A reference scenario, represented by trajectories minimizing fuel consumption and flight time, is compared with solutions that reduce the expected climate impact from NO_x emissions, identified using a set of prototype algorithmic Climate Change Functions (aCCFs). The seasonal and latitudinal variability of the properties of these optimized trajectories is analysed, highlighting its relation to the variability of the tropopause height. In winter, the potential of reducing the climate impact of NO_x emissions via trajectory optimization is found to be larger than in summer, due to stronger vertical gradients in the background atmospheric conditions at typical flight altitudes over the North Atlantic.

The results presented in this thesis suggest the existence of trade-offs between the reduction of different climate impact effects via operational strategies, when benefits and penalties are computed with respect to fuel-optimal solutions. Improving the understanding of the seasonal and weather variability of these potential benefits and penalties, this thesis provides useful insights to air traffic management on how to mitigate non-CO_2 effects aviation.

Samenvatting

Wereldwijde mobiliteit biedt aanzienlijke voordelen voor onze samenleving. Het maakt oplossingen mogelijk om ongelijkheden te verminderen, bijvoorbeeld door toegang te bieden tot hoogwaardig onderwijs en werkgelegenheid. Vanuit dit perspectief speelt de luchtvaart een cruciale rol in de sociale en economische ontwikkeling. Echter, slechts een klein deel van de wereldbevolking is momenteel verantwoordelijk voor meer dan de helft van de totale uitstoot van de burgerluchtvaart, wat een negatieve invloed heeft op de lokale luchtkwaliteit en het klimaat op aarde. De laatste jaren is er steeds meer druk om de milieuschade van de luchtvaart te beperken, met name door de uitstoot van koolstofdioxide (CO_2) te verminderen. Dit broeikasgas is verantwoordelijk voor een opwarming voor een lange tijd, omdat het jaren tot millennia in de atmosfeer blijft.

Koolstofdioxide is echter slechts één van de stoffen die door vliegtuigen worden uitgestoten. Andere klimaateffecten van de luchtvaart, de zogenaamde *niet-CO_2-effecten*, zullen naar verwachting ook een aanzienlijke bijdrage leveren aan de klimaatimpact van een vlucht. Deze effecten omvatten de vorming van condenssporen achter het vliegtuig (contrails) en de variaties in de concentraties van atmosferische ozon (O_3) en methaan (CH_4) als gevolg van de uitstoot van stikstofoxiden (NO_x). De netto klimaatimpact van deze niet-CO_2-effecten van de luchtvaart is sterk afhankelijk van de atmosferische omstandigheden. Contrails blijven bijvoorbeeld alleen langer dan een paar minuten in de atmosfeer hangen onder de juiste omstandigheden, dat wil zeggen bij ijsoververzadiging. De netto klimaatimpact van een vlucht kan dus niet alleen worden verminderd door verbeteringen in de eigenschappen van vliegtuigen en motoren, maar ook door de vliegroutes te optimaliseren om gebieden in de atmosfeer te vermijden waar de niet-CO_2-effecten van de luchtvaart bijzonder sterk zijn.

Gezien het mitigatiepotentieel van operationele maatregelen, is de hoofddoelstelling van dit proefschrift het definiëren, identificeren en analyseren van *"eco-efficiënte"* vliegtuigtrajecten die leiden tot een significante vermindering van de klimaatimpact met slechts geringe nadelen in termen van extra brandstofverbruik en vliegtijd. In het bijzonder is het doel om het begrip van hun variabiliteit over het gehele spectrum van natuurlijke atmosferische variabiliteit te verbeteren, rekening houdend met een groot aantal weersomstandigheden.

De eerste fase van dit promotieonderzoek richtte zich op de ontwikkeling van een strategie om milieuvriendelijke vliegtuigtrajecten te identificeren binnen langetermijnmodelsimulaties. Dit resulteerde in de implementatie van een besluitvormingstool, SolFinder 1.0, binnen de luchtverkeersoptimalisatiesoftware AirTraf 3.0, die gekoppeld is aan het ECHAM/MESSy Atmospheric Chemistry (EMAC) model. SolFinder omvat verschillende strategieën om één optie te selecteren uit een reeks gelijkwaardige optimale alternatieven, oftewel een Pareto-set. Deze selectie houdt rekening met informatie op hoog niveau die door de besluitnemer wordt verstrekt om de oplossingen van een multiobjectief optimalisatieprobleem te rangschikken, bijvoorbeeld het minimaliseren van het

brandstofverbruik en tegelijkertijd het beperken van de vorming van contrails tijdens de vlucht.

De eigenschappen van eco-efficiënte trajecten onder variërende atmosferische omstandigheden worden vervolgens geanalyseerd door middel van langetermijnsimulaties, waarbij voor elke dag 100 vluchten over de Noord-Atlantische Oceaan worden geoptimaliseerd in de periode van 1 december 2015 tot en met 31 december 2018. Verschillende routeopties worden vergeleken. Ten eerste analyseert dit proefschrift de invloed van meteorologische variabiliteit op trajectoptimalisatiestrategieën die de vorming van contrails verminderen met beperkte veranderingen in brandstofverbruik. Dit werk biedt inzicht in welke omstandigheden gekoppeld zijn aan een hoog potentieel voor het voorkomen van contrails, zodat deze vooraf kunnen worden geïdentificeerd. Met de focus op winterdagen wordt een gevestigde weerpatroonclassificatie op basis van de Noord-Atlantische Oscillatie (NAO) en Oost-Atlantische (EA) patronen toegepast om de gesimuleerde dagen in vijf klassen te verdelen. Een van deze gemiddelde weerpatronen, met een zwakke en gekantelde straalstroom, blijkt gekoppeld te zijn aan de hoogste verhouding tussen voordeel (vermindering van contrails) en nadeel (extra brandstofverbruik).

Ten tweede wordt de relatie tussen de klimaatimpact van NO_x en routeplanningsstrategieën onderzocht onder verschillende meteorologische omstandigheden. Een referentiescenario, weergegeven door trajecten die het brandstofverbruik en de vliegtijd minimaliseren, wordt vergeleken met oplossingen die de verwachte klimaatimpact van NO_x emissies verminderen. Deze oplossingen worden geïdentificeerd met behulp van een reeks prototype algoritmische klimaatveranderingsfuncties (aCCF's). De seizoensgebonden en breedtegraadvariabiliteit van de eigenschappen van deze geoptimaliseerde trajecten wordt geanalyseerd, waarbij de relatie met de variabiliteit van de tropopauzehoogte wordt benadrukt. In de winter blijkt het potentieel om de klimaatimpact van NO_x-emissies te verminderen door middel van trajectoptimalisatie groter te zijn dan in de zomer, vanwege sterkere verticale gradiënten in de atmosferische omstandigheden op typische vlieghoogtes boven de Noord-Atlantische Oceaan.

De resultaten die in dit proefschrift worden gepresenteerd, suggereren dat er afwegingen bestaan tussen de vermindering van verschillende klimaateffecten door middel van operationele strategieën, wanneer de baten en kosten worden berekend ten opzichte van brandstofoptimale oplossingen. Door het inzicht in de seizoensgebonden en weersafhankelijke variabiliteit van deze potentiële baten en kosten te verbeteren, biedt dit proefschrift nuttige inzichten voor luchtverkeersleiding over hoe de niet-CO_2-effecten van de luchtvaart kunnen worden beperkt.

1

Introduction

"Wonder is the beginning of wisdom."
Socrates

1.1 Overview and research gap

Aviation contributes positively to social and economic development, providing rapid connections between distant regions of the world. The benefits of aviation can be assessed by considering its contribution to the United Nations Sustainable Development Goals (UN SDGs; Perryman et al., 2022). For example, reliable global mobility enables access to quality education and work opportunities (UN SDGs 4 and 8), and it has the potential of reducing inequalities within and among countries (UN SDGs 10). However, access to air transportation is currently limited to a small portion of the global population, and more than half of the total civil aviation emissions are attributed to the most frequent flyers, accounting for just ~ 1% of the population (Gössling et al., 2020). Ensuring that more people benefit from the advantages provided by air transportation is challenging, as civil aviation is facing several critical issues. The demand for air traffic is increasing (International Air Transport Association (IATA), 2024), while the sector is struggling to mitigate its environmental effects. As more scientific evidence of the dangerous consequences of anthropogenic emissions is gathered, the pressure to reduce the environmental impact of flights increases.

Specifically, aircraft emissions affect the Earth's climate mainly through the following physical and chemical processes: (1) formation, spreading and persistence of condensation trail (contrail) cirrus, (2) perturbation of ozone, methane, and stratospheric water vapour caused by NO_x emissions, (3) emission of green-house gases, mainly CO_2 and H_2O, (4) aerosol interactions with radiation and clouds. Because of their different properties, the processes listed above are usually distinguished between CO_2 and non-CO_2 climate effects of aviation. Overall, air traffic is estimated to have contributed to ~3.5% of the total effective radiative forcing from anthropogenic emissions between 1940 and 2011 (Lee et al., 2021). About two thirds of this radiative forcing are attributed to non-CO_2 effects, with large uncertainties. In the past decades, CO_2 emissions have

been limited by improvements in aircraft fuel efficiency, driven by the aim of containing operational costs (Penner et al., 1999; Kharina et al., 2015; Yin et al., 2020).

More recently, several pathways have been determined to achieve carbon neutrality or climate goals for the sector. The former target, carbon neutrality, only addresses CO_2 emissions, while climate goals can extend to other climate effects of aviation. Climate-mitigation strategies for aviation can be classified into:

- technological improvements, e.g. lean-burn combustion and advanced aircraft engine design;
- use of new energy carriers, such as Sustainable Aviation Fuels (SAF), liquid hydrogen, or battery electric systems;
- operational practices, optimizing the aircraft flight trajectories;
- market-based measures, such as the EU Emissions Trading System (ETS) or the ICAO Carbon Offsetting and Reduction Scheme for International Aviation (CORSIA).

Each strategy for mitigating the aviation climate impact presents specific advantages and disadvantages. In the case of technological improvements, the main limit consists in the expected implementation timeline, considering that an aircraft has a typical lifetime of two/three decades, and about the same time is needed to develop and produce a new aircraft (Lee et al., 2023). Technological improvements have usually targeted reductions in the economic costs, e.g., by reducing the fuel consumption. As a result, these improvements have also significantly reduced the climate impact from CO_2 emissions. However, the consequences of their implementation on other aviation climate effects was often less investigated. This is crucial in order to understand their net benefits towards sustainability goals, since the literature shows that trade-offs exist when one aims at reducing different climate effects. For example, CO_2 emissions decrease with increasing overall propulsion efficiency, but the likelihood of forming contrails is predicted to increase (see Section 2.3).

Some mitigation strategies intended to reduce net carbon emissions might indirectly decrease the impact of other climate effects of aviation, leading to win-win situations. This could be the case, for example, of using Sustainable Aviation Fuels (SAF). The intended advantage of using SAF is that, if they are produced using biomass, the carbon emitted during the fuel combustion has been recently absorbed by plants from the atmosphere. The resulting cut in net CO_2 emissions can be estimated, also considering those emissions linked to fuel production and transport. Simultaneously, using SAF results in a reduction in the amount of emitted (soot) particles, thus affecting the radiative properties of contrails (Moore et al., 2017; Burkhardt et al., 2018). However, the net effect of SAF on the contrails climate impact is currently being investigated. Nevertheless, the use of SAF presents its own disadvantages, and it is limited by the availability of those resources that are needed to produce SAF sustainably.

Operational strategies offer the great advantage of not requiring a fleet renewal, thus their implementation could occur on shorter time-scales. Moreover, these strategies allow to address both CO_2 and non-CO_2 effects from aviation. The latter can be reduced considering that atmospheric conditions at the time and location of emission play a crucial role in determining the magnitude, and even the sign (cooling vs. warming

effects), of the radiative forcing terms due to the non-CO_2 effects of aviation. For example, only regions that are supersaturated with respect to ice can sustain the persistence of contrails (Schumann, 1996). The complex interactions between solar radiation, atmospheric circulation, and background chemistry control the processes of ozone formation and methane depletion, which are perturbed by NO_x emissions (Köhler et al., 2008). Moreover, the residence time of the water vapour emitted during a flight may vary significantly, e.g. depending on distance of the emission location from the tropopause (Manen et al., 2019). Because of its high dependency on time and location of emission, the total aviation radiative forcing could be reduced by avoiding regions of the atmosphere characterized by high non-CO_2 effects, defined as *climate-sensitive* regions. This concept explains the rising interest in investigating the potential of using operational measures to mitigate non-CO_2 effects from aviation, including optimizing aircraft trajectories to minimize their climate impact (see Section 2.5). However, the implementation of these measures is currently restricted by crucial knowledge gaps, e.g. weather forecast uncertainties (Gierens et al., 2020), and low level of scientific understanding of aviation non-CO_2 effects (Lee et al., 2021). Moreover, if more fuel is used to avoid a *climate-sensitive* region, one should weight the relative importance of limiting the long-term climate impact of CO_2 emissions and the short-term non-CO_2 effects (Lee et al., 2023).

Earth System Models (ESMs) have been employed to evaluate the mitigation potential of aircraft trajectory optimization. For example, previous studies developed the concept of Climate Change Functions, to represent the dependency of the climate impact of a specific emission on its time and location (Grewe et al., 2014a). After computing the values of the climate change functions, these data were used to derive climate-optimized trajectories, and the feasible trade-off between climate impact and operational costs (Figure 1.1). Grewe et al. (2014b) demonstrated that it may be possible to identify *eco-efficient trajectories*, i.e. trajectories causing a significantly lower climate impact than those optimized with respect to operating costs, at relatively small cost variations. For example, for westbound trans-Atlantic flights, on a representative winter day, a 25% reduction in the climate impact would be achieved, with a ~ 0.5% increase in the operational costs (Grewe et al., 2014b).

Other studies confirmed that aircraft climate impact and operating cost are expected to be conflicting optimization strategies (Yamashita et al., 2021). Limiting operating costs penalties brings not only economic advantages. In fact, it also corresponds to limiting extra CO_2 emissions, as the increase in operating cost is driven by changes in fuel used and flight time. Obtaining a certain mitigation level can be less expensive, if only specific flights are redirected to avoid climate-sensitive conditions (Teoh et al., 2020). For applications in the European airspace, most of the overall mitigation potential appears to be obtained from a small fraction of the total air traffic (Matthes et al., 2020). Therefore, **new tools should be developed to identify and select such critical trajectories, also named as *"eco-efficient"* solutions,** and avoid additional penalties that are not compensated by significant advantages in terms of climate impact reduction. The characteristics of these eco-efficient solutions should then be studied under a multitude of weather patterns, to analyse their properties over the range of atmospheric natural variability, as the effects of aircraft trajectory optimization are expected to show a large spatial and temporal variability (Yin et al., 2018a). Therefore, eco-efficient trajectories

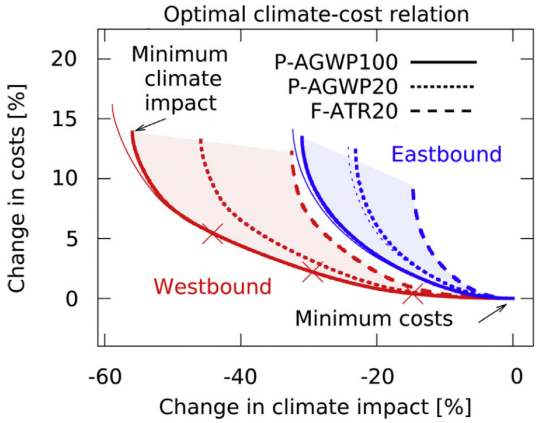


Figure 1.1: Optimal climate-cost relations obtained optimizing the trans-Atlantic air traffic, under the weather conditions of a representative winter day. The climate impact is measured using different emissions (pulse (P), or future emission scenarios (F)), metrics (absolute global warming potential (AGWP), or average temperature response (ATR)), and time horizons (20 or 100 years). Figure from Grewe et al. (2014b).

should be analysed over different atmospheric conditions and regions of the airspace, in order to fully evaluate their actual benefits and costs. Moreover, considering a wide range of weather conditions, it would be possible to investigate if specific patterns lead to larger mitigation potential at lower costs: if a correlation exists, it would be relevant information for the Air Traffic Management. This doctoral project will address these research gaps, as highlighted in the next section.

1.2 Objective and research questions

The main objective of this doctoral project is to **define, identify, and analyse *"eco-efficient"* trajectories,** which lead to significant climate impact reductions at small penalties in terms of additional fuel consumption and flight time. Considering the research gaps highlighted in Section 1.1, the following questions will be addressed:

1. How can we identify eco-efficient aircraft trajectories?
2. How do eco-efficient aircraft trajectories change over the range of atmospheric natural variability?
3. Are eco-efficient aircraft trajectories more beneficial under specific weather patterns?
4. How are different climate effects of aviation reduced by eco-efficient aircraft trajectories?

1.3 Thesis structure

First, Chapter 2 provides an overview of the background knowledge necessary to evaluate the approach and results of the doctoral research. Then, Chapter 3 describes the methods

chosen in the initial phase of this research to address the objective. These methods were further developed within this thesis to enable the identification of eco-efficient aircraft trajectories, as described in Chapter 4. Subsequently, this modelling chain was employed to investigate how varying atmospheric conditions affect contrail avoidance (Chapter 5) and the minimization of NO_x climate effects via trajectory optimization (Chapter 6). These results are discussed and summarized in the last two chapters of this thesis (Chapter 7 and Chapter 8).

2 Background

"Avoiding climate breakdown will require cathedral thinking.
We must lay the foundation
while we may not know exactly
how to build the ceiling."
Greta Thunberg [1]

2.1 Atmospheric composition and structure

The Earth's atmosphere is composed by a large number of elements, but just three of them constitute almost the entire volume of dry air: nitrogen (78%), oxygen (21%), and argon (0.93%). All other compounds are called *trace gases* and, even if present in small quantities, also play crucial roles in the atmospheric physical and chemical processes. In this thesis, we are mainly interested in the chemical compounds emitted or interacting with emissions from aircraft: 1) water, 2) carbon dioxide, 3) ozone, and 4) methane. In the following paragraphs, a brief introduction of each of these components is provided.

Water (H_2O) is present in the atmosphere in different phases: vapour, liquid droplets, and ice particles. It enters and leaves the atmosphere via the *water cycle*, which transfers water from one reservoir to another (oceans, soil, biosphere, atmosphere, etc.). The atmosphere holds just a small fraction (0.001%) of the H_2O available on the planet, as water is quickly removed via precipitation (Chahine, 1992). In fact, the average residence time of water in the atmosphere is about 8-10 days (Gimeno et al., 2021). As a comparison, oceans store about 97% of the total H_2O, which has an average residence time of more than three millennia in this reservoir (Chahine, 1992). In the atmosphere, the content of water varies significantly with time and space. The variable *relative humidity* is commonly used to describe how moist the atmosphere is at a certain location and time. This variable describes the flux of H_2O molecules between different phases, e.g. gaseous and liquid. When this flux is at equilibrium, the relative humidity is 100%, indicating that *saturation* has been reached. Relative humidity is defined as the ratio

[1] From Greta Thunberg's speech to British Parliament on April 23, 2019. A transcript of the full speech is available at https://www.theguardian.com/environment/2019/apr/23/greta-thunberg-full-speech-to-mps-you-did-not-act-in-time, last accessed on July 8, 2025.

between the amount of water present locally, and the amount corresponding to saturation conditions, for example, measured as partial pressure. The saturation partial pressure of water varies with temperature, since warm air can hold more water than cold air before reaching saturation. An increase in H_2O atmospheric concentration affects the water cycle and the climate system with direct warming, since H_2O is the main contributor to the natural greenhouse gas effect.

Carbon dioxide (CO_2) is likely the most well-known greenhouse gas. Similarly to water, CO_2 is exchanged between different reservoirs through the so called *carbon cycle*. For example, the atmosphere constantly exchanges CO_2 with the biosphere via respiration and photosynthesis. Human activities perturb the natural carbon cycle, leading to an accumulation of CO_2 in the atmosphere. The Intergovernmental Panel on Climate Change (IPCC, 2021) reports that anthropogenic emissions caused an increase in CO_2 atmospheric concentrations from about 280 parts per million (ppm) - pre-industrial levels, before the year 1750 - to 410 ppm in 2019. Even though carbon sinks (oceans, biosphere) have mitigated this perturbation and delayed the resulting changes in the climate system, the atmospheric lifetime of CO_2 is generally very long, varying from years to millennia. Because of this long residence time, CO_2 is homogeneously distributed around the globe.

Ozone (O_3) is present in the atmosphere in small quantities, varying from 10^{-6}% to 10^{-3}% of its volume. Almost all the O_3 is located at high altitudes (15-35 km, Hegglin et al. 2015), forming the so-called *ozone layer*. The ozone layer is crucial for the survival of the biosphere. In fact, it filters solar ultraviolet (UV) radiation that would otherwise reach the surface. Absorbing solar radiation, the ozone layer also warms the local environment. This drives the temperature vertical profile and the general atmospheric circulation. Therefore, the ozone layer is a fundamental element of the climate system. A minor fraction of the atmospheric O_3 (about 10%) is found closer to the surface, where its concentration rises locally due to anthropogenic pollution (Intergovernmental Panel on Climate Change (IPCC), 2023). Here, O_3 is harmful to the biosphere, e.g. causing respiratory health issues and damaging plants. Therefore, high ozone concentrations close to the Earth's surface drastically reduce the local air quality.

Methane (CH_4) is present in the atmosphere due to both natural and anthropogenic sources. Major natural sources include wetlands, volcanic activities, and wildfires. However, human activities (e.g. production and use of fuels, industrial agriculture) currently dominate the annual methane emissions (Jackson et al., 2020). Methane is stronger than CO_2 with respect to its greenhouse gas warming potential, but it has a much shorter average life-time of about 7-12 years.

The processes involving the chemical compounds described above and, therefore, their residence time, are highly affected by where they are located in the atmosphere. In fact, the atmosphere is structured into different layers, characterized by different physical and chemical characteristics. The layer located closest to the surface is called *troposphere*, from the Greek word *"tropos"*, meaning "rotation", "movement". The troposphere is in constant transformation, as most of the weather phenomena that we observe occur within this layer. The layer above the troposphere is called *stratosphere*. In the stratosphere, dynamical processes are slower than in the troposphere, thus the residence time of chemical compounds is generally much longer. Water, for example, has

a residence time of a few days in the troposphere (Gimeno et al., 2021) and of a few years in the stratosphere (Zhou et al., 2024; Pletzer et al., 2024). The two layers are separated by the *tropopause*, which has an altitude that varies with time and location. Different definitions of the tropopause are available, based on temperature gradients (thermal tropopause), potential vorticity threshold values (dynamic tropopause), or gradients in chemical concentrations, e.g. ozone (chemical tropopause). The significant differences between troposphere and stratosphere explain the different impact that aircraft emissions cause when they occur below or above the tropopause (see Chapters 5 and 6).

2.1.1 Radiative forcing

An important concept employed in this thesis is the *radiative forcing* (RF). This section provides a summary of the RF description included in the Fifth Assessment Report of the Intergovernmental Panel on Climate Change (IPCC AR5, 2013). The RF is defined in the IPCC AR5 as the *"net change in the energy balance of the Earth system due to some imposed perturbation"*. This quantity is a convenient metric to measure the impact of an agent (emission, cloudiness, etc.) on the climate. However, it is crucial to completely define what this quantity refers to. For example, RF can be calculated considering the flux changes at the top of the atmosphere or at the tropopause. Moreover, important distinctions exist between instantaneous, adjusted, and effective RF, as explained below.

The initial flux change (*instantaneous* RF, see IPCC, 2021, their Figure TS.14) is not a direct indicator of the surface temperature response to a perturbation. In fact, depending on the nature of the perturbation, the initial change in the radiative flux evolves differently over time, as a result of specific alterations in the climate system. Ultimately, the same instantaneous RF may cause different temperature responses.

The concept of *adjusted* RF aims at partially taking into account this issue. In fact, the standard definitions of RF used throughout the IPCC report refers to the *stratospherically adjusted* RF, measuring the flux changes at the tropopause after stratospheric temperatures have adjusted to a new radiative equilibrium. This RF definition still neglects adjustments occurring in other elements of the system because of the perturbation, such as tropospheric and surface temperatures, cloudiness, vegetation, etc. Among these effects, it is possible to distinguish rapid adjustments, occurring immediately after the perturbation, and other responses triggered by changes in surface temperature resulting from the initial perturbation.

The commonly used *effective* RF (ERF) accounts for all rapid adjustments, and neglects the indirect feedbacks caused by the ocean surface temperature change resulting from the perturbation. Distinctions are also reported in the ERF calculation approaches across different studies, which may fix the surface temperature everywhere, or include rapid adjustments over land. In the latter case, only ocean temperatures are fixed to the field characterising the unperturbed system.

This brief summary highlights the variety of approaches employed to measure the radiative imbalance caused by a perturbation, e.g. aircraft emissions. When evaluating and comparing different effects of human activities, it is therefore important to employ RF calculations and metrics based on the same assumptions, and that are relevant indicators of the resulting climate impact.

2.2 Climate effects of aircraft emissions

Aircraft jet engines burning kerosene emit several chemical compounds, that affect the local environment and determine changes in the climate system. The products of the ideal combustion of kerosene (C_xH_y) with air (mainly O_2 and N_2, see Section 2.1) are CO_2 and H_2O, following to the stoichiometric balance below[2]:

$$C_xH_y + (x + y/4)(O_2 + nN_2) \longrightarrow xCO_2 + (y/2)H_2O + n(x + y/4)N_2 \tag{2.1}$$

However, the engine plume includes several other chemical components:

- carbon monoxide (CO), unburned hydrocarbons (UHC) and soot (C) originating from the incomplete combustion of kerosene;
- nitrogen oxides (NO_x = NO + NO_2), a by product of the high temperatures reached during combustion;
- fuel impurities (sulfur, aromatics), leading to the production of sulfate aerosols and soot.

These emissions from jet engines have complex interactions with the local environment, impacting the local air quality as well as the climate of our planet. In this section, an overview of the climate effects due to aircraft emissions is provided.

Aviation is estimated to contribute 3-5% to the total anthropogenic global warming (Lee et al., 2021). Aircraft emissions affect the radiative budget of our planet through several effects, which are usually distinguished between carbon dioxide (CO_2) and non-CO_2 effects (Lee et al., 2010). Non-CO_2 effects account for about 2/3 of the aviation net effective radiative forcing (Lee et al., 2021). These effects include the radiative forcing from contrail cirrus (Section 2.3), the perturbations in the atmospheric concentrations of ozone (O_3) and methane (CH_4) caused by nitrogen oxide (NO_x) emissions (Section 2.4), and the emission of water vapour (H_2O) in the stratosphere, where it has a long life-time.

Figure 2.1 visualizes estimates of their effective radiative forcing (ERF, mW m^{-2}) as presented by Lee et al. (2021). These values are relative to the species emitted by the global air traffic from 1940 to 2018. Looking at Figure 2.1a, it is evident that non-CO_2 effects are associated to larger uncertainties than the ERF from CO_2 emissions. In particular, the 5-95 % confidence interval of contrail cirrus ERF extends from 17 to 98 mW m^{-2}. The best estimate (57 mW m^{-2}) ranks contrails as the largest single contributor to aviation climate impact (see Figure 2.1b). However, the relative importance of contrail cirrus may be lower or higher when compared to the other main effects of aviation, considering the wide confidence interval (Figures 2.1c-d). Contrarily, the direct impact of H_2O emissions appears to be negligible, since civil aircraft mainly fly in the troposphere or lower stratosphere. As a result, H_2O emissions of most flights are quickly removed via the hydrological cycle.

[2]The content of this section includes notes of the course *Aircraft Emissions and Climate Effects*, lectures from V. Grewe and M. Merlens.

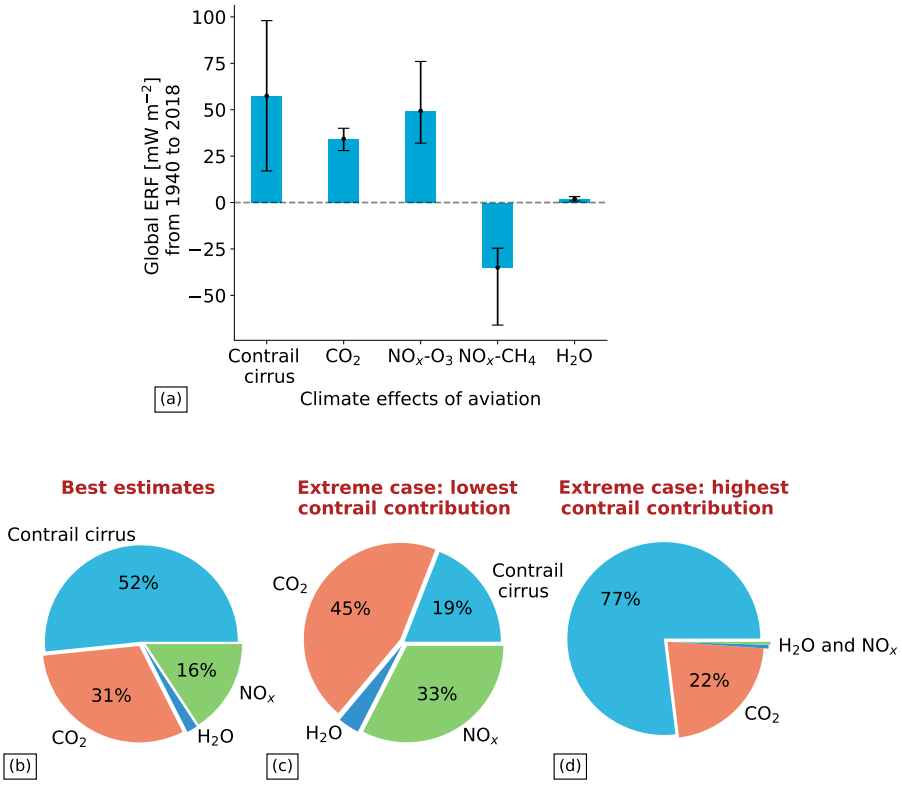


Figure 2.1: Estimates provided by Lee et al. (2021) of the global effective radiative forcing (ERF, mW m^{-2}) from the main climate effects of aviation, considering the impact cumulated over the period 1940-2018. In Figure 2.1a, NO_x-O_3 refers to the short-term reduction of atmospheric ozone concentrations due to NO_x emissions, while NO_x-CH_4 includes the impact of NO_x emissions on methane and its feedback on the production of ozone (long-term reduction) and stratospheric water vapour. Figures 2.1b-d visualize the variability in the relative importance of different effects, when considering the best estimates (panel b), or edges of the confidence intervals (panels c-d). Figure 2.1c represents the lowest edge for contrail cirrus and the highest edges of all other effects, while Figure 2.1d shows the highest edge for contrail cirrus and the lowest edges of all other effects. Adapted from Table 2 and Figure 3 of Lee et al. (2021).

Note that the relative importance of different climate effects of a subset of flights (e.g., European flights in 2015) can be very different from the one presented by Lee et al. (2021), which is relative to the emission inventory from global air traffic between 1940 and 2018. This is due to the impacts that atmospheric variability and aircraft/engine characteristics have on CO_2 and non-CO_2 effects. These dependency are explained in the following Sections, describing the formation of contrails and their associated radiative forcing (Section 2.3), and the climate effects of NO_x emissions (Section 2.4). Lastly, Section 2.5 provides an overview on the literature related to climate-optimized aircraft trajectories.

2.3 Contrail and contrail cirrus

As discussed in the previous Section, contrail cirrus are associated with the largest best estimate of effective radiative forcing among the climate effects of aviation. However, this estimate is provided with a large confidence interval and low level of scientific understanding. In this Section, the complex processes involved in the formation of contrails and contrail cirrus are described. Subsequently, the competing positive and negative radiative forcings of contrails and contrail cirrus clouds are explained.

2.3.1 Formation of contrail and contrail cirrus

Numerous studies have investigated the processes that lead to the formation of contrails (Schmidt, 1941; Appleman, 1953; Schumann, 1996; Kärcher, 2018). Here, the main findings reported in the literature are summarized. The formation of contrails is described from a thermodynamic point of view by the Schmidt-Appleman criterion (Schmidt, 1941; Appleman, 1953; Schumann, 1996). Figure 2.2 provides a schematic representation of this criterion, which is described in the following paragraphs.

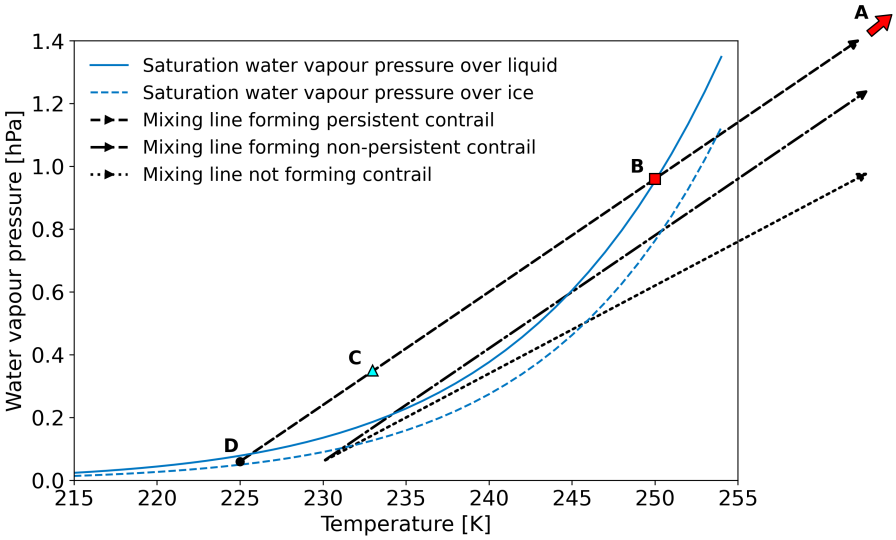


Figure 2.2: Schematic representation of the Schmidt-Appleman Criterion.

Aircraft emissions are the result of the combustion of the fuel-air mixture in the jet engine (Section 2.2), which occurs at temperatures, pressures, and humidity much higher than the atmospheric conditions. Therefore, if point A in Figure 2.2 represents the initial temperature T [K] and water vapour pressure e [hPa] of the exhaust plume, then A is located outside the area covered by the graph. The properties of the combustion process that are relevant for contrail formation are:

- the water vapour emission index;
- the specific heat content of the fuel;

- the overall propulsion efficiency.

The exhaust plume enters the atmosphere and starts cooling, while freely expanding and mixing with the ambient air. The plume cools and may reach supersaturation over liquid water (point B in Figure 2.2). At this point, water droplets form in the plume. The number of droplets formed mainly depends on the amount of aerosol particles emitted by the aircraft and present in the atmosphere, which act as water condensation nuclei. These steps occur during the so-called *jet regime* of contrail formation, over a timescale of $\mathcal{O}$(0.1 s). In the following few seconds, the exhaust plume merges with the wake vortex pair forming behind the aircraft wings. Therefore, during the *vortex regime*, contrail formation and evolution is heavily influenced not only by thermodynamic processes, but also by fluid-dynamics.

If the plume cools to a temperature below a threshold value for formation of ice particles - typically 233 K (Kärcher, 2018) - then a visible linear contrail is formed behind the aircraft (point C in Figure 2.2). At this point, ambient conditions determine if the ice particles formed in the first minutes after emission will sublimate or grow (point D in Figure 2.2). Meanwhile, the linear contrail descends to altitudes lower than the flight level at which it formed, as it is entrained with the vortex pair. The length of the descent is in the order of $\mathcal{O}$(100 m), potentially reaching warmer and ice sub-saturated air in the lower part of the wake. As a consequence, sublimation would occur, leading to a loss of ice particles. However, if ice-supersaturation conditions are present in the upper part of the wake, ice crystals grow and the contrail is still visible after the initial minutes of formation stage. A linear shaped contrail with a lifetime longer than about 10 minutes is referred to as *persistent contrail* (Kärcher, 2018).

Lastly, the background atmospheric conditions (winds, temperature, relative humidity) determine the life-time and spreading of a persistent contrail. If the contrail loses its original linear shape, it transitions into a so-called *contrail cirrus*. Contrail cirrus clouds can extend over an area of $\mathcal{O}$(100 km) and perturb the atmosphere for $\mathcal{O}$(10 h), thus they are expected to be associated with a large radiative forcing (Section 2.3.2).

Thermodynamic considerations can be used to determine whether a persistent contrail will form. As one can see in Figure 2.2, the mixing line slope and ambient conditions determine whether (1) water condensates into liquid droplets, (2) freezing occurs, (3) and if ice supersaturation supports the growth and persistence of the contrail. The Schmidt-Appleman criterion (Schmidt, 1941; Appleman, 1953; Schumann, 1996) provides a formula to compute the mixing line slope G in terms of atmospheric pressure p and properties of the aircraft, engine, and fuel used[3]. The slope G is defined as the ratio of the differences between the ambient temperature and water vapour partial pressure (T_{amb}, e_{amb}) and those at the engine exhaust (T_{exit}, e_{exit}):

$$G = \frac{e_{exit} - e_{amb}}{T_{exit} - T_{amb}} \tag{2.2}$$

The partial pressure of water vapour e can be rewritten in terms of mass mixing ratio q and atmospheric pressure p, since $e = \frac{p}{\epsilon} q$, where $\epsilon = 0.622$ is the ratio of the molar masses of water and air.

[3]The derivation of the slope G is based on course material from Volker Grewe and Klaus Gierens.

Therefore:

$$e_{exit} = \frac{p}{\epsilon} \frac{\text{water vapour mass flux}}{\text{air mass flux}} \tag{2.3}$$

$$= \frac{p}{\epsilon} \frac{\dot{m}_a q_a + \dot{m}_f EI_{H_2O}}{\dot{m}_a + \dot{m}_f} \tag{2.4}$$

$$e_{amb} = \frac{p}{\epsilon} q_a \tag{2.5}$$

where $\dot{m}_a$ is the air mass flux after instantaneous mixing of the bypass and core air fluxes, $\dot{m}_f$ is the air mass flux from fuel combustion, q_a is the ambient water mass mixing ratio, and EI_{H_2O} is the water emission index (for kerosene, EI_{H_2O}=1.23). Considering that $q_a << EI_{H_2O}$, the numerator of Eq.2.2 can be rewritten as:

$$e_{exit} - e_{amb} \approx \frac{p}{\epsilon} \frac{\dot{m}_f EI_{H_2O}}{\dot{m}_a + \dot{m}_f} \tag{2.6}$$

The denominator of Eq.2.2 can be rewritten considering that, as energy is conserved, the chemical energy of the fuel is equal to the sum of work obtained, thermal energy of the exhaust, and kinetic energy of the exhaust. Neglecting the last term, which is on order of magnitude smaller than the other terms, we find that:

$$(1-\eta)\dot{m}_f Q = c_p \dot{m}_a (T_{exit} - T_{amb}) + c_p \dot{m}_f T_{exit} \tag{2.7}$$

$$= c_p \dot{m}_a (T_{exit} - T_{amb}) + c_p \dot{m}_f (T_{exit} - T_{amb}) + c_p \dot{m}_f T_{amb} \tag{2.8}$$

where η [-] is the overall propulsion efficiency, Q [J/kg] is the specific heat content (for kerosene, Q = 43.2 MJ/kg), and c_p [KJ kg^{-1} K^{-1}] is the specific heat capacity. Neglecting the enthalpy of ambient air ($c_p T_{amb}$) with respect to the other terms allows to rewrite the denominator of Eq.2.2 as follows:

$$T_{exit} - T_{amb} = \frac{\dot{m}_f}{c_p(\dot{m}_a + \dot{m}_f)}(1-\eta)Q \tag{2.9}$$

And, in conclusion:

$$G = \frac{e_{exit} - e_{amb}}{T_{exit} - T_{amb}} = \frac{c_p}{\epsilon} p \frac{1}{1-\eta} \frac{EI_{H_2O}}{Q} \tag{2.10}$$

Looking at Eq.2.10, we can observe the slope G and, subsequently, the formation of contrails depends on:

- the background conditions at the time and location of the flight, since it is proportional to the atmospheric pressure p;
- the aircraft/engine configuration, as it is inversely proportional to the overall propulsion efficiency η;

- the fuel used, which determine the water vapour emission index EI_{H_2O} and the specific heat content Q.

This formulation of G allows to predict several characteristics of contrail formation, e.g. that contrail formation becomes more likely when the overall propulsion efficiency η increases. Note that the mixing line is an approximation of the real evolution of the temperature T and partial pressure e conditions within the plume. In reality, the mixing of exhaust and ambient air will not follow a straight line: as the water condensates when liquid water super-saturation is reached (point B in Figure 2.2), the conditions in the plume will evolve approximately along the curve of water saturation, as phase change ensures equilibrium between gaseous and liquid phase. Similarly, when water droplets freeze and turn into ice particles, the conditions will approach those along the curve of ice saturation. Nevertheless, these approximations should not affect the outcome, as they do not affect the regions of the graph where points A, B, C, and D are located in Figure 2.2, that are relevant to determine if a persistent contrail forms.

2.3.2 Radiative forcing of persistent contrails

Contrails perturb the radiative balance of our atmosphere by (1) reflecting the incoming short-wave solar radiation, and (2) changing the outgoing longwave radiation flux at the top of the atmosphere. The former is linked to a negative radiative forcing, RF_{SW}, while the latter leads to a positive radiative forcing, RF_{LW}. Taking into account both components, the net impact of a contrail can be evaluated. This is a challenging task, because the explicit computation of the radiative forcing terms is complex and computationally expensive.

To overcome this limit, an empirical parameterization have been developed by Schumann et al. (2012). Here, RF_{SW} is approximated as being proportional to the solar direct irradiance, and dependent on five properties: (1) the contrail optical depth at 550 nm, (2) the cosine of the solar zenith angle, (3) the effective albedo of the Earth–atmosphere system, (4) the effective contrail ice particle radius, and (5) optical depth at 550 nm of the cirrus above the contrails. Therefore, RF_{SW} is highly dependent not only on the properties of the contrail, but also on the time of the day at which it is present. As a result, RF_{SW} is affected by a large diurnal variability. During the night, RF_{SW} is null, and the impact of contrails is fully determined by RF_{LW}. Therefore, nighttime contrails can only be warming contrails. The calculation of RF_{LW} is simplified by Schumann et al. (2012) via the following empirical formula:

$$RF_{LW} = (OLR - k_T(T - T_0))(1 - e^{\alpha})E_{LW} \geq 0 \tag{2.11}$$

where:

- OLR is the outgoing longwave radiation at the top of the atmosphere
- the term $k_T(T - T_0)$ approximates the change in outgoing longwave radiation due to the difference between the contrail temperature T and the brightness temperature of the atmosphere without contrails (k_T and T_0 are free parameters).
- $1 - e^{\alpha}$ represents the effective emissivity of the contrail, determined by its optical properties via the exponent α, which depends on the effective contrail ice particle radius and the contrail optical depth;

- E_{LW} approximates the reduction in outgoing longwave radiation due to a cirrus above the contrail.

With Equation 2.11, the warming impact of a contrail is estimated considering its temperature, which is usually colder than the brightness temperature of the contrail-free sky (Schumann et al., 2012). The larger this difference is, the larger the resulting RF_{LW}.

2.4 NO_x emissions

Aircraft emissions of nitrogen oxides (NO_x = NO + NO_2) at cruise altitudes perturb the background atmospheric concentrations of ozone (O_3), methane (CH_4), and stratospheric water vapour (H_2O). As these are among the main greenhouse gases, changes in their concentrations significantly impact the atmospheric radiative budget, as summarized in Table 2.1. Considering the main direct effects and feedback processes, Lee et al. (2021) reported a net sensitivity to NO_x emissions of 5.5 ± 8.1 mW m^{-2} (Tg(N) $yr^{-1})^{-1}$ in terms of effective radiative forcing. Considering a global aviation emission inventory from 1940 to 2018, NO_x emissions are expected to be associated with a positive net effective radiative forcing (Lee et al., 2021).

Concentration change	Perturbation life-time	Effective radiative forcing [1]
short-term increase in O_3	weeks/months[2]	34.4 ± 9.9 mW m⁻2 (Tg (N) $yr^{-1})^{-1}$
decrease in CH_4	~10 years[3]	−18.7 ± 6.9 mW m⁻2 (Tg (N) $yr^{-1})^{-1}$
long-term decrease in O_3	~10 years[3]	−9.3 ± 3.4 mW m⁻2 (Tg (N) $yr^{-1})^{-1}$
decrease in stratospheric H_2O	~10 years[4]	−2.8 ± 1.0 mW m⁻2 (Tg (N) $yr^{-1})^{-1}$

[1] Lee et al. (2021). [2] Rosanka et al. (2020). [3] Stevenson et al. (2004).

[4] Same as CH_4, driving the perturbation (Myhre et al., 2007), plus ~ 2 years (Pletzer et al., 2024).

Table 2.1: Summary of direct and indirect effects from aviation NO_x emissions.

The chemical reactions involving NO_x emissions and the background atmospheric species are described in detail by previous studies (Crutzen, 1979; Rosanka et al., 2020). After entering the atmosphere, NO reacts with HO_2, leading to the formation of OH and NO_2:

$$HO_2 + NO \longrightarrow OH + NO_2 \tag{2.12}$$

The emitted NO_x has a life time of about a month. It reacts with HO_x, forming nitric acid (HNO_3) and peroxynitric acid (HNO_4), and these species are then removed from the atmosphere, for example, by acid rains. Before the emitted NO_x is removed, Reaction 2.12 contributes directly to two main effects: a short-term increase in tropospheric ozone, and a reduction in methane concentrations.

The first effect occurs due to the the catalytic formation of ozone (Reaction 2.14) via the photolysis of NO_2 (Reaction 2.13):

$$NO_2 + h\nu(\lambda \leq 410nm) \longrightarrow NO + O(^3P) \tag{2.13}$$

$$O(^3P) + O_2 + M \longrightarrow O_3 + M \tag{2.14}$$

The short-term increase in ozone concentration results in a positive (warming) radiative forcing. A few weeks after the time of emission, NO_x is no longer available for ozone production via Reactions 2.13-2.14, thus the initial increase in ozone concentration peaks, followed by a decrease in the O_3 concentration perturbation. The magnitude and timing of the peak in O_3 increase depend on where and when the NO_x emission occurs, as illustrated in Figure 2.3 from Maruhashi et al. (2022). This graph describes the simulated evolution of the NO_x-induced short-term O_3 mass, comparing the effects of emissions occurring at two different dates, within five geographic regions. Figure 2.3 shows that, in general, the ozone mass rapidly increases in the first ~ 15 days after emission. Slower increases for ~ 30 days are also possible, and are connected to a longer residence time.

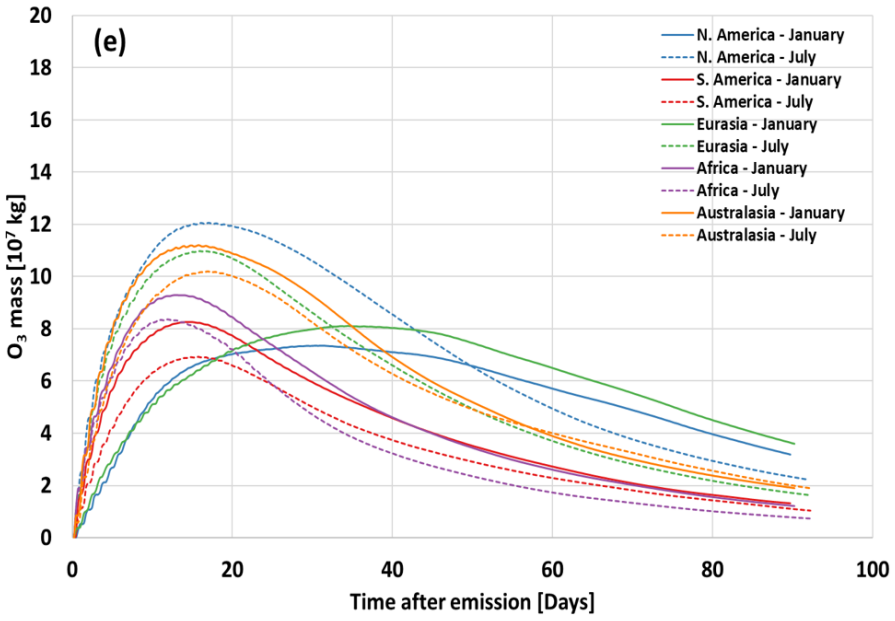


Figure 2.3: Mean temporal evolution of the NO_x-induced short-term O_3 mass [kg], averaged across 28 emissions points within each of the five regions (North America, South America, Eurasia, Africa, Australasia) for two release conditions (January, July). From Figure 15 in Maruhashi et al. (2022).

The second effect of NO_x emission is an increase in the removal of methane, as a result of the increase in its principal sink, OH:

$$CH_4 + OH \longrightarrow CH_3 + H_2O \tag{2.15}$$

The negative perturbation of methane concentration causes a negative (net-cooling) radiative forcing, and is characterized by a longer life-time (about a decade) than the perturbation in O_3. In addition to these two direct effects, NO_x emissions affect the climate system via two feedback processes: a long-term decrease in tropospheric ozone, and a decrease in stratospheric water vapour. Both these feedback processes are consequences of the induced methane depletion. The long-term decrease in ozone concentration is known as *primary mode ozone* (PMO), and it leads to a sign change in the O_3 perturbation after a couple of years from the NO_x emission (Wild et al., 2001). The second feedback process is represented by the reduction in the water vapour production in the stratosphere via methane oxidation, leading to a negative radiative forcing. The short-term increase in O_3 dominates the impact of NO_x effects on the climate system, resulting in a net warming. The other effects are expected to only partially mitigate the warming due to the short-term increase in O_3 (Lee et al., 2021).

2.5 Aircraft trajectory optimization as a climate impact mitigation strategy

The temperature perturbation resulting from CO_2 emissions is only dependent on the amount of emitted CO_2, since its atmospheric lifetimes range from years to millennia. To reduce CO_2 emissions, several solutions are currently under development, exploring, for example, the use of new propulsion technologies or alternative aviation fuels (Staples et al., 2018; Yin et al., 2020). Contrarily, non-CO_2 effects occur over short timescales, which typically range from hours (e.g., contrails) to months or years (e.g., NO_x-induced changes on O_3 and CH_4). As a consequence, the temperature perturbation caused by an aircraft unit emission is highly dependent on the time and location of the emission (Köhler et al., 2013; Frömming et al., 2021). Several studies investigated the possibility of using this time and space dependency to reduce the climate effect of a flight, for example, by optimizing its trajectory to minimize the induced temperature increase (Stevenson et al., 2009; Sridhar et al., 2011; Grewe et al., 2017b; Matthes et al., 2021). Towards the implementation of this type of operational strategies, some recent studies highlighted the main challenges and opportunities related to the avoidance of climate sensitive regions by aircraft trajectories optimization (Simorgh et al., 2022; Molloy et al., 2022). Most importantly, the current level of scientific understanding of the non-CO_2 effects of aviation is lower than the one of CO_2 effects, as demonstrated by the uncertainty ranges of the radiative forcing estimates reported by Lee et al. (2021). Moreover, the identification of climate sensitive regions (e.g., ice-supersaturated regions, supporting persistent contrails) relies on the availability of accurate weather forecast. Depending on the stability of the forecast over time, trajectories can be optimized via tactical adjustments during the flight or, preferably, in advance (e.g., one day before departure) to limit the associated penalties in operating costs, for example minimizing fuel use and workload of flight crew and air traffic controller (Grewe et al., 2017a; Molloy et al., 2022).

The earliest studies evaluating the potential of changing aircraft trajectories to reduced their climate impact focused on contrails. Both changes in departure times and flight altitudes were considered. For example, Myhre et al. (2001) considered the diurnal cycle of radiative forcing due to contrails, and found that the climate impact of contrails could be reduced by flying more at sunrise and sunset. The benefit of changing cruise altitudes (Williams et al., 2003; Fichter et al., 2005; Mannstein et al., 2005) and lateral paths (Klima, 2005) to reduce contrail formation and their climate impact was analysed since the early 2000s. Only after 2010, more studies considered the possibility of reducing the overall climate impact of aviation via air traffic management, mitigating not only the impact of contrails, but also other main non-CO_2 effects (Ng et al., 2011; Chen et al., 2014; Grewe et al., 2014b).

To evaluate the climate impact mitigation potential of changing aircraft trajectories, different approaches have been employed, which can be classified into two main categories:

- studies that perturb a reference scenario to simulate changes, e.g., in departure times, altitudes, horizontal paths;
- studies that solve optimization problems, to identify trajectories minimizing objective functions including the flight's climate impact, either directly or indirectly.

The first class includes several early studies in the field, such as Williams et al. (2003) and Irvine et al. (2014b). This approach is suitable to answer several research questions, for example, exploring whether changing the peak altitude or peak departure time of the current air traffic can lead to climate impact benefits. However, the maximum benefit achievable at a unit increase in operational cost can only be evaluated via aircraft trajectory optimization. Aircraft trajectories can be optimized with respect to their emissions (for example, as done in Celis et al., 2014) or the distance flown through ISSRs. The latter has been the preferred choice of most studies assessing contrail avoidance (e.g., Yin et al., 2018a). These quantities are not a direct measure of climate impact, because of the temporal and spatial variability of non-CO_2 effects of aviation. In fact, for example, NO_x and H_2O live longer when emitted in the stratosphere than in the troposphere, leading to a larger radiative forcing (Section 2.1). Contrails can cause cooling effects, instead of warming, under the right conditions (Section 2.3.2).

To directly account for the aircraft climate impact in an objective function, climate metrics are necessary. Table 2.2 lists the most widely used climate metrics.

Climate metric	**Definition**
Radiative Forcing (RF)	$\mathrm{RF}(t_0 + H)$
Global Warming Potential (GWP)	Integrated RF over the time horizon H
Global Temperature Change Potential (GTP)	$\Delta T(t_0 + H)$
Average Temperature Response (ATR)	Average ΔT over the time horizon H

Table 2.2: List of the most commonly used climate metrics.

To fully define a climate metric, two elements must be specified:

1. the time horizon H (see Table 2.2);
2. the emission scenario, such as Pulse emission (P), or a Future scenario (F) representing a realistic evolution of the air traffic over the years.

The most suitable choice of metric, time horizon, and emission scenario depends on the research question addressed. For example, GTP calculated with short time horizons (e.g., 20 years) can be employed to assess the risk of exceeding target limits in anthropogenic global warming, such as those set by the Paris Agreement in 2015. Longer time horizons (e.g., 100 years) assign more importance to the long-lived effects from CO_2 emissions, rather than on short-lived effects from contrails and NO_x emissions. Megill et al. (2024) provides an extensive comparison of different climate metrics, assessing them based on requirements such as temporal stability and compatibility with existing climate policies. Therefore, Megill et al. (2024) offers valuable guidance in the selection of a climate metric.

3

Methodology

"Remember that all models are wrong;
the practical question is
how wrong do they have to be
to not be useful."
George E. P. Box

The research presented in this thesis employs and further develops pre-existing concepts and methods. In this Chapter, an overview of such approaches is given, focusing on those aspects that are most relevant to understanding the findings of this doctoral project. This thesis aims at identifying and analysing the properties of eco-efficient trajectories, under a large number of weather conditions. In the initial phase of this doctoral research, the ECHAM/MESSy Atmospheric Chemistry (EMAC) model has been selected as a suitable model to address the research questions presented in Chapter 1, because of its unique capability to simulate both atmospheric processes and air transport. To achieve this, EMAC (Chapter 3.1) is coupled with an air traffic optimizer, AirTraf (Chapter 3.2). The submodel AirTraf was in this thesis further developed to solve decision-making problems within multi-objective optimizations (as described in Chapter 4), in order to efficiently identify eco-efficient flights. Multi-annual simulations can be conducted with the EMAC and AirTraf models within an appropriate computational time (i.e. a 1-year simulation is completed within ~2 weeks running on the TU Delft High Performance Cluster, HPC12). In addition, AirTraf can optimize aircraft trajectories based on several objective functions, including contrail distance and climate effects. The former is computed via coupling to the CONTRAIL submodel (Chapter 3.3), which is responsible for the identification of regions of the atmosphere supporting persistent contrails. Climate effects are estimated by the ACCF submodel (Chapter 3.4) in terms of average temperature response over 20 years (ATR20). This modelling chain is therefore suitable for conducting the experiments described in Chapters 5 and 6 of this thesis. To correctly interpret these results, this Chapter describes relevant characteristics of the EMAC model and its three submodels AirTraf, CONTRAIL, and ACCF.

3.1 Introduction to EMAC

The EMAC model is a numerical climate model system that includes sub-models describing tropospheric and middle-atmosphere processes and their interaction with oceans, land and human influences (Jöckel et al., 2010). This system relies on the second version of the Modular Earth Submodel System (MESSy2) to connect multi-institutional computer codes, while the core atmospheric model is the 5th generation European Centre Hamburg general circulation model (ECHAM5, Roeckner et al., 2006). In this thesis, EMAC (ECHAM5 version 5.3.02, MESSy version 2.55.0) was employed in the T42L31ECMWF resolution. This resolution has a spherical truncation of T42 (corresponding to a quadratic Gaussian grid of approximately 2.8 by 2.8 degrees in latitude and longitude), and includes 31 vertical hybrid pressure levels up to 10 hPa (i.e., to an altitude of approximately 30 km). Figure 3.1 illustrates the relation between the EMAC model and the three submodels that have a major relevance in this research: CONTRAIL (Frömming et al., 2014), ACCF (Yin et al., 2023), and AirTraf (Yamashita et al., 2020).

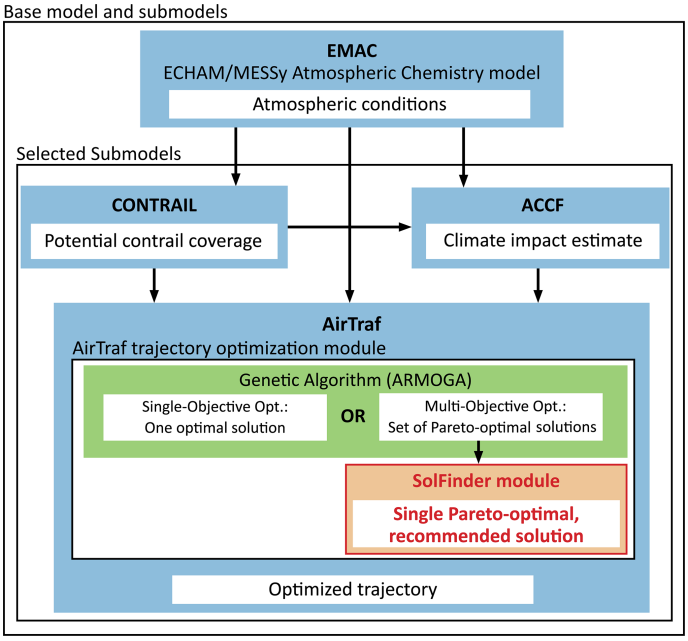


Figure 3.1: Overview of the relations between EMAC and the three submodels AirTraf (Chapter 4.2), CONTRAIL (Chapter 3.3), and ACCF (Chapter 3.4). In this thesis, AirTraf has been developed to solve decision-making problems within multi-objective optimizations using the SolFinder module (Chapter 4), which is highlighted in red in the diagram.

The EMAC model provides the atmospheric conditions at a specific time and location (e.g., wind, temperature, potential vorticity, relative humidity) to the other submodels, which use them as input to determine fuel consumption, emission indices, climate effects, and other relevant fields. To obtain weather conditions aligned with those

observed over specific time periods (e.g., January 2018 in Chapter 4), the simulations are conducted nudging by Newtonian relaxation the prognostic variables of divergence, vorticity, temperature, and the (logarithm of the) surface pressure down to the surface towards reanalysis data (Dee et al., 2011; Jöckel et al., 2016; Hersbach et al., 2020).

The CONTRAIL submodel computes the potential contrail coverage, i.e., the fraction of the model grid-box where persistent contrails can exist (Burkhardt et al., 2008). The ACCF submodel employs the algorithmic Climate Change Functions (aCCFs) in order to deliver the estimated spatially and temporally resolved climate effect of aviation emissions to AirTraf (Yin et al., 2023). Lastly, the AirTraf submodel identifies the optimal aircraft trajectories with respect to the routing strategy selected by the user. The optimization process is performed in two steps: (1) a genetic algorithm - Adaptive Range Multi-Objective Genetic Algorithms (ARMOGA, Sasaki et al., 2005) - is employed to solve a single- or multi-objective optimization problem; (2) if a multi-objective optimization is solved, it is possible that more than one optimal solution is found, thus a decision-making module developed during this thesis (SolFinder, Castino et al., 2024) intervenes to select a single recommended trajectory, based on the preferences of the user. These submodels of EMAC are described more in detail in the following sections.

3.2 AirTraf submodel

The air traffic simulator AirTraf is responsible for the optimization of the aircraft trajectories, according to the routing strategy prescribed by the user. The submodel requires as input information on:

- the atmospheric conditions at the time and location of the flight (e.g., temperature and wind fields);
- the air traffic sample, including the location of the airports of departure and arrival, the departure time of each flight, and characteristics of the aircraft and engine type to be simulated (Yamashita et al., 2016).

Once this information is collected, a genetic algorithm intervenes to identify an optimal trajectory. The number of design variables of the optimization problem is fixed to 11, since the model describes each aircraft trajectory as a B-spline curve defined by three control points on the horizontal domain (three pairs of coordinates) and five on the vertical cross-section (as illustrated in Figure 3.2). The domains of the horizontal control points are centered on the great circle connecting the airports of departure and arrival, while the vertical control points are bounded by the flight levels at 29000 ft (FL290) and at 41000 ft (FL410), corresponding to altitudes of about 8.8 and 12.5 km.

To calculate the flight properties along a candidate trajectory, the path is divided in flight segments by $n_{\mathrm{wp}} = 101$ waypoints. In particular, to calculate the fuel used at each flight segment, AirTraf uses the aircraft performance model of Eurocontrol's Base of Aircraft Data (BADA Revision 3.9, Eurocontrol, 2011) and the Deutsches Zentrum für Luft- und Raumfahrt (DLR) fuel flow method (Yamashita et al., 2016). A daily air traffic sample is repeated on every simulation day, and the flights included in this sample are optimized individually. Various routing strategies are available: each option aims at

optimising the trajectories based on a specific objective function, estimating e.g. fuel used, operating cost, or the climate impact of a flight.

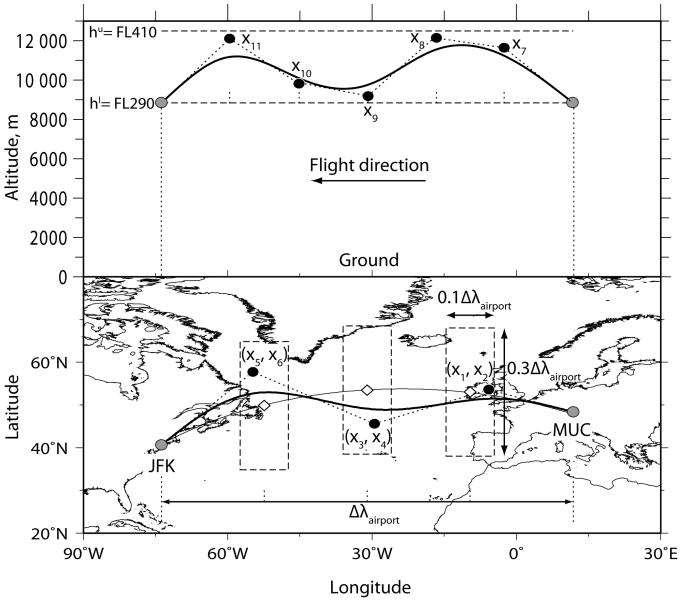


Figure 3.2: Geometry definition of the flight trajectory in the AirTraf sub-model. A trajectory from MUC to JFK is used as example (bold solid lines). Top: the vertical cross section; the dashed lines indicate the lower/upper variable bounds in altitude. Bottom: projection on the Earth; the dashed boxes define the rectangular domains of the three control points. Figure from Yamashita et al. (2016).

The procedure followed to optimize the aircraft trajectories is explained in detail in Yamashita et al. (2016), and summarized here. First of all, it is important to highlight that the trajectory is only optimized at the model timestep corresponding to flight departure, and it is not re-optimized along the route. In other words, the optimal trajectory is identified assuming that the atmospheric conditions along the flight are those simulated by the model at departure time, without considering that the situation might evolve while the aircraft moves towards its destination. The reason for this assumption is that the optimization is performed by a stochastic optimization algorithm, the Adaptive Range Multi-Objective Genetic Algorithm (ARMOGA, Sasaki et al., 2005), which is computationally expensive. On the other hand, this method brings crucial benefits. Most importantly, the algorithm does not require the calculation of derivatives or gradients of the objective functions, which do not have to be continuous.

The genetic algorithm follows a few main steps to solve the optimization problem at hand. In its initialization step, random values within the domain are assigned to the design variables to obtain a *population* of n_{pop} initial solutions. Then, the following operators are used in the optimization loop:

- *evaluation*: for each trajectory in the population, the objective function is calculated;

- *selection*: based on the values of the objective functions, all solutions in the population are ranked using the Fonseca and Fleming's Pareto ranking method (Fonseca et al., 1993); in terms of the biological evolutionary concepts that inspired the genetic algorithm development, this ranking method assigns a *fitness* value to the individual solution, which is proportional to the number of solutions that dominate it - i.e., correspond to better objective function values;

- *crossover*: new solutions are generated, starting from the group of best solutions within the current population;

- *mutation*: to ensure that new solutions are explored in the next generation, a certain level of disturbance is added in this step.

By following this process, after a certain number of generations, the algorithm identifies a trajectory that minimizes the given objective function. Benchmarks tests were conducted to configure AirTraf, considering what is a satisfying compromise between computational effort and convergence to an optimal solution (Yamashita et al., 2016). As a result, the AirTraf sub-model successfully minimizes the selected objective function within single-objective optimization problem (Yamashita et al., 2020). Moreover, because of the chosen genetic algorithm (ARMOGA, Sasaki et al., 2005) and Pareto ranking method (Fonseca et al., 1993), the method described here can be extended to solve multi-objective optimization problem, with the addition of a decision-making module. This development of AirTraf, performed within this thesis, will be described in Chapter 4.

Yamashita et al. (2016) describes in detail the assumptions and limitations of the model. Firstly, Eurocontrol's Base of Aircraft Data (BADA Revision 3.9, Eurocontrol, 2011) with a constant Mach number is used to calculate the fuel consumption. The sensitivity of the model's results to this choice is not within the scope of this thesis, but on-going research is investigating the impact of using different aircraft performance models. The quality of the fuel use model was assessed in Yamashita et al. (2016), comparing the flight time, fuel consumption, and NO_x emission index with reference data from BADA and previous studies (e.g. Penner et al., 1999 and Grewe et al., 2014b). Since comparable values and trends are achieved, Yamashita et al. (2016) concludes that AirTraf includes a sufficiently good fuel use model.

AirTraf neglects constraints originating from conflicts and airspace structure, since it optimizes individual trajectories within a free-routing airspace. Moreover, only the cruise phase of the flight is simulated by AirTraf, thus take-off and landing are not included. This aspect is not expected to significantly impact the optimization when the cruise phase is dominating compared to the other flight phases, which is the case for the North Atlantic flights optimized in Chapter 5 and Chapter 6. The optimization of shorter flights (e.g. over Europe, see Chapter 4) might benefit from the inclusion of all flight phases, although the optimization flexibility is limited during take-off and landing (Yamashita et al., 2021).

The sign of the relative changes obtained by AirTraf under different routing strategies has been compared with previous literature by Yamashita et al. (2020). In particular, the obtained trade-offs between pairs of objectives - for example, fuel and flight time, NO_x emissions and operating costs, contrail distance and fuel, or climate impact and economic

costs - are qualitatively in agreement with those of earlier studies (e.g. Celis et al., 2014; Niklaß et al., 2017). Moreover, AirTraf computes a flight delay cost (i.e., the operating cost penalty of flying the time optimal route) which is well aligned to those reported by Cook et al. (2009).

To summarize, several tests have been performed by Yamashita et al. (2016), Yamashita et al. (2020), and Yamashita et al. (2021), demonstrating the correct implementation of AirTraf and the agreement of its results with previous literature. Considering the objective of this thesis, AirTraf is therefore chosen to address the research questions identified in Chapter 1.

3.3 CONTRAIL submodel

This section describes another submodel of EMAC, CONTRAIL, which identifies the regions of the atmosphere where contrails can form and persist (Frömming et al., 2014). First, the parameterization used to simulate ice supersaturated regions (ISSRs), contrails, and natural cirri is presented. Subsequently, the resulting spatial and temporal variability of the potential coverage of contrails, contrail cirri and natural cirri is described.

3.3.1 Ice supersaturated regions and potential contrail coverage

Ice supersaturated regions (ISSRs) play a crucial role in determining the climate impact of contrails, since their presence affects the life-time of contrails and, as a consequence, their climate impact (Chapter 2.3). Observations from radiosonde and in-flight measurements suggest that ISSRs have typical dimensions of $\mathcal{O}(100\text{ m})$ vertically and less than 100 km horizontally[1] (Gierens et al., 2000; Spichtinger et al., 2003; Kärcher, 2018). Therefore, they are usually not resolved by general circulation models. In this study, the ECHAM5 model is used with an horizontal resolution of $2.8^\circ \times 2.8^\circ$ in latitude and longitude, and a vertical resolution of about 700-900 m between 8-13 km of altitude[2] (T42L31ECMWF resolution, see Chapter 3.1). Subsequently, ice supersaturation is a sub-grid scale atmospheric condition for our model, thus it requires a parameterization to be simulated.

In the following paragraphs, the method used to represent ice supersaturated regions in the CONTRAIL submodel is described. This parameterization was first introduced by Burkhardt et al. (2008) and was later implemented in the CONTRAIL submodel, as described in Grewe et al. (2014a) and its supplement material (Frömming et al., 2014). The parameterization is based on the same assumptions used to simulate the natural cloud coverage, regarding the subgrid-scale variability of humidity. The nomenclature and calculations described here are based on Burkhardt et al. (2008) and, in particular, on its supplementary material. Firstly, it is necessary to define some essential quantities, which are visualized in Figure 3.3 and summarized in Table 3.1. This scheme assumes that the the probability density function $G(q_t)$ describes the variability of the total water vapour mass mixing ratio q_t within each model grid box. Note that q_t represents the *total* water

[1] Gierens et al. (2000) found that the mean path lengths flown inside an ISSR is 150 km, analysing 3 years of MOZAIC data (1995-1997). However, they suggested that most ISSRs might have a much smaller diameter (<10 km) due to a selection bias.

[2] This is the range of altitudes most relevant for the air traffic considered in this project. See, for example, Figure 5.4.

present in the region of atmosphere described by the model grid-box, which can include both clear-sky and cloudiness. Another variable, q_{env}, is introduced as representative (mean) water vapour mass mixing ratio for the grid-box cloud-free environment.

The probability density function $G(q_t)$ is a uniform distribution centred in $\overline{q_t}$:

$$\int_0^\infty G(q_t)dq_t = 1 \tag{3.1}$$

Assuming that *all supersaturation is immediately converted into cloudiness*, as commonly done in global general circulation models, it follows that the natural cirrus cloud cover b_{ci} is defined as:

$$b_{ci} = \int_{q_{sat}}^\infty G(q_t)dq_t \tag{3.2}$$

where q_{sat} is the ice saturation water vapour mass mixing ratio at the grid-box temperature. Note that the model grid-box mean water vapour mass mixing ratio, q, differs from the average q_t, indicated as $\overline{q_t}$. In fact, cloudy air is seen as saturated by the model, according to the assumption stated above. Therefore, q can be calculated as:

$$q = b_{ci}q_{sat} + (1 - b_{ci})q_{env} \tag{3.3}$$

One can see from Eq. (3.3) and Figure 3.3 that only if no cirrus is present ($b_{ci} = 0$), then $q = \overline{q_t} = q_{env}$. In presence of cloudiness ($b_{ci} \neq 0$), the relation $q_{env} < q < \overline{q_t}$ is true. The width w_G of the distribution $G(q_t)$ is fixed, and it is defined by the threshold value for natural cirrus formation, q_{ci}:

$$w_G = 2(q_{sat} - q_{ci}) \tag{3.4}$$

In other words, assigning a value to q_{ci} corresponds to defining the magnitude of the variability of q_t within a model grid-box. The smaller q_{ci} is, the larger the range of equally possible values of q_t becomes, and saturation will be exceeded in a fraction of the grid-box even at relatively low values of $\overline{q_t}$.

The explanation above can be summarized as follows:

$$b_{ci} = \begin{cases} 0 & if\ \overline{q_t} \leq q_{ci} \\ \beta,\ 0 < \beta < 1 & if\ q_{ci} < \overline{q_t} < q_{sat} + q_{ci} \\ 1 & if\ \overline{q_t} \geq q_{sat} + q_{ci} \end{cases} \tag{3.5}$$

Note that, in this derivation, cloud formation is initialized whenever the water vapour mass mixing ratio reaches saturation. This assumption is commonly made in general circulation models, and it correctly describes the formation of water clouds. However, cirrus clouds start forming at higher levels of ice supersaturation, when the conditions for homogeneous ice nucleation are reached. For this reason, some ice-supersaturated regions (ISSRs) support the persistence of natural cirrus clouds, but not their formation.

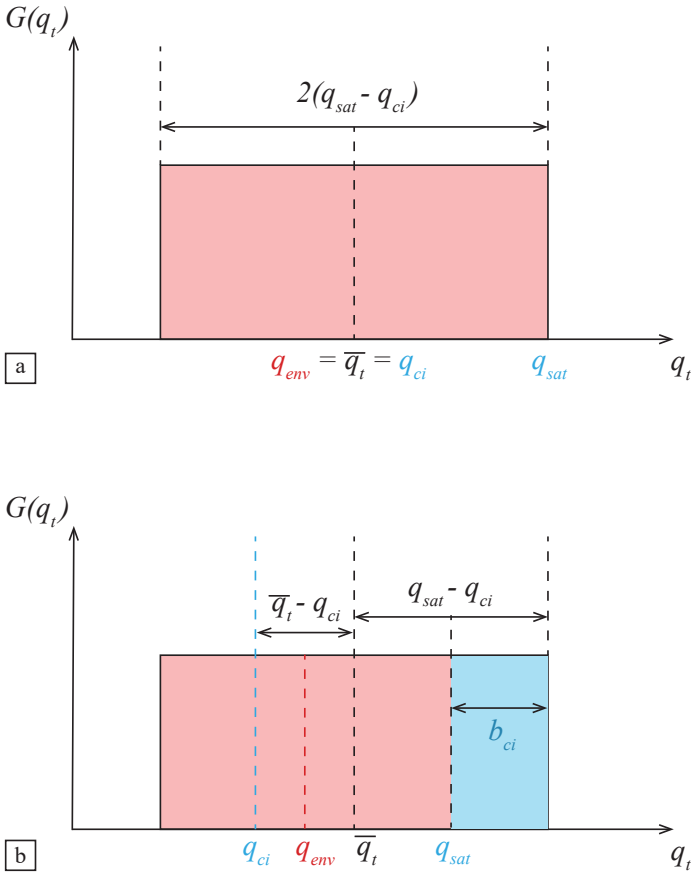


Figure 3.3: Visual representation of the probability density function of q_t, illustrating the scheme used in the CONTRAIL submodel to represent the cirrus coverage b_{ci}. Panel a illustrates the case $\overline{q_t} = q_{ci}$, while Panel b represents a scenario with $\overline{q_t} > q_{ci}$. Adapted from Figure in the Supplement material of Burkhardt et al. (2008).

Therefore, ISSRs can be observed with clear-sky conditions or cloudiness. Note that cirri can be transported to regions of lower ice supersaturation, and persist there, after their formation occurred elsewhere. To estimate the extension of ISSRs, an additional threshold value of water vapour mass mixing ratio is introduced, q_{cc}, with $q_{cc} < q_{ci}$, such that ISSRs are found for $\overline{q_t} > q_{cc}$. Note that, from this definition, it follows that q_{cc} marks the lowest value of $\overline{q_t}$ at which contrail cirrus could form. The distance between q_{cc} and q_{ci} is determined by the the relative humidity threshold for homogeneous ice nucleation $\mathrm{RH_{nuc}}$, which ranges between 1.5 and 1.7, and varies with the temperature T[K] according to the following formula (Koop, 2004):

$$\mathrm{RH_{nuc}}(T) = 2.349 - \frac{T}{259}$$

The ratio q_{cc}/q_{ci} is also controlled via the parameter α_{nuc}. When q_{cc} is calculated as

in Eq. (3.6), setting $\alpha_{nuc} = 0.9$ results in a realistic representation of ISSRs by the model (Burkhardt et al., 2008):

$$\frac{q_{cc}}{q_{ci}} = \frac{q_{cc}}{q_{sat}}\frac{q_{sat}}{q_{ci}} = \frac{RH_{cc}}{RH_{ci}} = \frac{RH_{sat}}{\alpha_{nuc}RH_{nuc}} = \frac{1}{\alpha_{nuc}RH_{nuc}} \longrightarrow q_{cc}(T) = \frac{q_{ci}}{\alpha_{nuc}RH_{nuc}(T)} \tag{3.6}$$

At this point, it is possible to derive the fraction of the grid-box where natural cirrus can form, b_{ci}, and the ice-supersaturated fraction of the grid-box, B_{cc+ci}. Within this latter fraction B_{cc+ci}, the persistence of contrails and natural cirri is possible. Moreover, contrails can form, thus B_{cc+ci} is also called *potential contrail coverage*. Considering the uniform distribution $G(q_t)$:

$$b_{ci} = \int_{q_{sat}}^{\infty} G(q_t)\, dq_t, = \begin{cases} 0, & q_{env} < q_{ci} \\ 1 - \frac{2(q_{sat}-q_{env})}{w_G} = \frac{q_{env}-q_{ci}}{q_{sat}-q_{ci}}, & q_{ci} \le q_{env} \le q_{sat} \end{cases} \tag{3.7}$$

and, considering that clouds may be present in ISSRs, we can similarly derive:

$$B_{cc+ci} = \begin{cases} 0, & q_{env} < q_{cc} \\ \frac{\overline{q_t}-q_{cc}}{w_G} = \frac{2(q_{env}-q_{cc})}{w_G} = \frac{q_{env}-q_{cc}}{q_{sat}-q_{ci}}, & q_{cc} \le q_{env} \le q_{sat} - (q_{ci} - q_{cc}) \\ 1, & q_{env} > q_{sat} - (q_{ci} - q_{cc}) \end{cases} \tag{3.8}$$

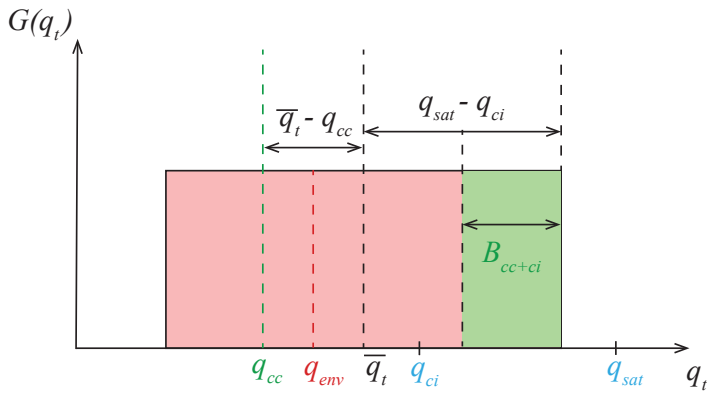


Figure 3.4: Visual representation of the probability density function of q_t, illustrating the scheme used in the CONTRAIL submodel to represent the potential contrail coverage B_{cc+ci}. Adapted from Figure in the Supplement material of Burkhardt et al. (2008).

Having the goal of describing both b_{ci} and B_{cc+ci} in terms of the model grid-box mean water vapour mass mixing ratio q, we rewrite Eq. (3.7) and Eq. (3.8) using Eq. (3.3):

$$b_{ci} = \int_{q_{sat}}^{\infty} G(q_t)\, dq_t, = \begin{cases} 0, & q < q_{ci} \\ 1 - \sqrt{\frac{q_{sat}-q}{q_{sat}-q_{ci}}}, & q_{ci} \le q \le q_{sat} \end{cases} \tag{3.9}$$

$$B_{cc+ci} = \begin{cases} 0, & q < q_{cc} \\ \frac{q-q_{cc}}{q_{sat}-q_{ci}} - b_{ci}(1-b_{ci}), & q_{cc} \le q \le q_{\star} \\ 1, & q > q_{\star} \end{cases} \tag{3.10}$$

where $q_{\star} = q_{sat} - (q_{ci} - q_{cc})^2/(q_{sat} - q_{ci})$.

Lastly, we can calculate the *potential contrail cirrus coverage* B_{cc}, defined as the region of the atmosphere that is ice-supersaturated, but where natural cirrus cannot form. From this definition, it follows that:

$$B_{cc} = B_{cc+ci} - b_{ci} \tag{3.11}$$

Symbol	Description
	water vapour mass mixing ratios
q	model grid-box mean
q_t	atmospheric total
q_{env}	cloud-free environment mean
q_{sat}	value at which water vapour is saturated w.r.t. ice
q_{ci}	threshold: if $\overline{q_t} > q_{ci}$ natural cirrus form in (part of) the grid-box
q_{cc}	threshold: if $\overline{q_t} > q_{cc}$ (part of) the grid-box is an ISSR, thus persistent contrail cirrus can be found
	other variables
$G(q_t)$	q_t probability density function
w_G	width of distribution $G(q_t)$
b_{ci}	cirrus coverage (grid-box fraction covered by natural cirri)
B_{cc+ci}	potential contrail coverage (ice-supersaturated grid-box fraction)
B_{cc}	potential contrail cirrus coverage
RH_{nuc}	relative humidity threshold for homogeneous ice nucleation
α_{nuc}	parameter determining the ratio q_{cc}/q_{ci}

Table 3.1: Symbols and descriptions of the main variables and parameters used in Chapter 3.3, following Burkhardt et al. (2008).

3.3.2 Resulting frequency and spatio-temporal variability of ISSRs

Burkhardt et al. (2008) compared the resulting supersaturation occurrences with those observed by aircraft in situ measurements and space-born remote sensing, finding a general agreement in values and patterns in the extra-tropics. A recent one-day case study performed by Peter et al. (2025) found that the potential contrail coverage areas matched with regions where contrails were observed by aircraft in situ measurements and satellite data, despite systematic biases in the EMAC temperature and humidity fields. The same study performed a comparison of the regions supporting persistent contrails identified by EMAC and ERA5 over a full spring season (March-April 2014). EMAC is found to overestimate potential contrail coverage compared to ERA5 by less than 10%, and correctly simulates the extension of areas where persistent contrails can form. Therefore, Peter et al. (2025) concludes that EMAC sufficiently well simulates contrail formation for the use in contrail avoidance studies.

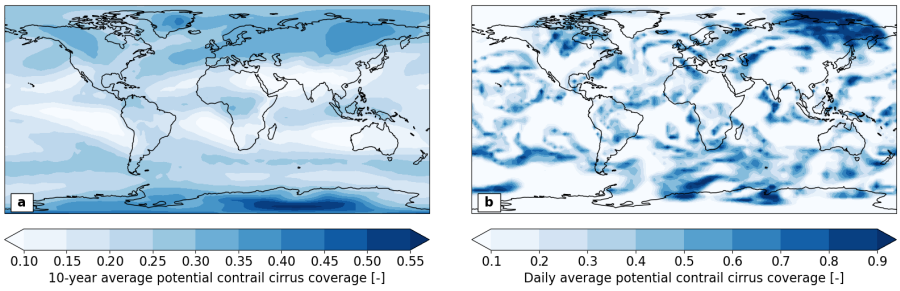


Figure 3.5: Potential contrail cirrus coverage computed by the CONTRAIL submodel: Panel a shows the mean pattern at 250 hPa, averaged over 10 years (from 1 December 2009 to 1 December 2019). Panel b provides an example of daily pattern at 250 hPa (1 December 2016).

Figure 3.5 illustrates the spatio-temporal variability of clear-sky ISSRs, i.e of the *potential contrail cirrus coverage* calculated by the CONTRAIL submodel. In particular, Figure 3.5a provides the 10-year average potential contrail cirrus coverage over the globe, interpolated at 250 hPa. Most importantly, this Figure shows that the North Atlantic and European regions, which are the focus of this research, are characterized by a relatively high frequency of ISSRs conditions, while this probability reduces moving to tropical regions. The global pattern of potential contrail cirrus coverage at 250 hPa is well aligned with the ISSRs occurrence frequency reported by Lamquin et al., 2012 (see their Figure 9), which considered the Atmospheric InfraRed Sounder (AIRS) relative humidity measurements in the period 2003–2009. In particular, the analysis from Lamquin et al. (2012) shows similar peaks over the western cost of North America, eastern coast of Greenland, and local maxima linked to the storm track and jet stream over the North Atlantic ocean.

The geographical distribution of ISSRs is characterized by strong spatio-temporal gradients, as visualized in Figure 3.5b. Here, the conditions simulated by the CONTRAIL submodel on one day (1 December 2016) are represented. Looking at this Figure, it is evident that areas supporting persistent contrails are highly localized. Therefore, if this

information is available and the weather forecast is robust, it would be possible to include such information in the flight planning and avoid ISSRs, especially in case of long flights.

To conclude, the CONTRAIL submodel is found to well simulate the likelihood of forming a persistent contrail at a specific location and time. A more detailed analysis of the vertical, seasonal, and weather pattern variability of potential contrail coverage over the North Atlantic was performed as part of the research presented in this thesis, thus further discussion on the performance of this submodel is included in Chapter 5.

3.4 The ACCF submodel

Estimating the climate impact of aviation emissions is a complex task. As described in Chapter 2.2, the climate impact of a flight results from the net effect of several processes, which operate on different spatial and temporal scales. Therefore, simulating such processes within an atmospheric-chemistry model such as EMAC is computationally expensive. For this reason, it is not feasible to explicitly calculate, for example, the climate impact from NO_x emissions, while evaluating a large number of aircraft trajectories to identify those minimizing the total flight climate impact.

To face this limit, a solution was suggested and developed within the ATM4E project[3], which consists of finding a relationship between:

- commonly available atmospheric fields, such as temperature and potential vorticity, and
- the climate response to aircraft emissions, as evaluated via comprehensive simulations with an atmospheric-chemistry model.

In this framework, a small number of variables are therefore used as proxy to estimate the climate impact of a flight. The resulting set of simple relationships, called *algorithmic climate change functions* (aCCFs), is thus very inexpensive from a computational point of view. Therefore, they are suitable to be used as objective function of an aircraft trajectory optimization problem, even though they cannot fully capture the complex dependency between background atmospheric conditions and aviation non-CO_2 effects (Rao et al., 2022). In the following sections, the development of the prototype version of the aCCFs is described, followed by the description of their implementation in the EMAC submodel ACCF.

3.4.1 Datasets used for the aCCFs derivation

The aCCFs are algorithmic approximations of large datasets, describing the dependency of the impact of a specific non-CO_2 effect of aviation on the background atmospheric conditions under which the aircraft emission occurred. These datasets were obtained with different methods, depending on the non-CO_2 effect. A description of these different methods is provided in the paragraphs below. The key differences between the datasets are summarized in Table 3.2.

[3]More information about the ATM4E project is available visiting the project website: https://www.atm4e.eu/ (Accessed: 9 July 2024).

Non-CO_2 effect	**Contrails**	**NO_x and H_2O**
Days	All days in three winters (Dec, Jan, Feb in 1994-95, 1995-96, 2003-04)	Eight representative days (five in winter, three in summer)
Time of air parcel trajectory initiation	12-hourly	06:00, 12:00, and 18:00 UTC
Def. of North Atlantic region	35-60°N, 0-70°W	30-80°N, 0-75°W
Vertical levels	300-250-200 hPa	400-300-250-200 hPa
Atmospheric fields:		
- Source	ERA-Interim / ECMWF IFS	EMAC
- Horizontal res.	1° × 1°	2.8° × 2.8°
- Vertical res.	60 levels up to 0.01 hPa	41 levels up to 5 hPa
- Temporal res.	6 hours	15 minutes

Table 3.2: Overview of the data used for the derivation of the aCCFs of different species.

Grewe et al. (2014b) describes in detail the derivation of the so-called *climate change functions* (CCFs) used as input for the H_2O and NO_x aCCFs. These CCFs are computed using a configuration of the EMAC model that includes its submodels ATTILA (Atmospheric Tracer Transport in a Lagrangian Model, Reithmeier et al., 2002) and AIRTRAC, which *tracks* the contribution of a local emission source to the resulting atmospheric concentrations on an air parcel (see Supplement of Grewe et al., 2014b). These two submodels determine the perturbation in atmospheric concentrations resulting from aircraft emissions at specific locations and times. Subsequently, EMAC computes the radiative forcing associated with those concentration changes. Lastly, this information is provided in terms of various climate metrics, e.g. average temperature response or absolute global temperature potential over a time horizon of 20 years (ATR20 and AGTP20, respectively). The H_2O and NO_x CCFs were computed for eight representative days, both during winter (five days) and summer (three days), which cover the range of variability of the atmosphere over the North Atlantic according to the weather classification by Irvine et al. (2013)[4].

In the case of contrails, the data used for the aCCF derivation was computed using the methods described in Irvine et al. (2014a) and in the supplement material of Yin et al. (2023). In this approach, the atmospheric variables are provided by the ERA-Interim reanalysis data, and Lagrangian trajectories describing the air parcels transport are computed offline using a fourth-order Runge-Kutta integration scheme. This analysis includes all days in three winters (December, January, February of 1994-95, 1995-96, 2003-04), chosen to cover the natural atmospheric variability during the winter season over the North Atlantic. The time resolution of the data along the trajectory is 6 hours (equal to the ERA-Interim time resolution). Thresholds for temperature (235 K) and relative humidity (98%) are used to identify conditions supporting contrail formation.

[4]This weather classification method is also employed in Chapter 5, where more information is provided.

At the time and locations where these criteria are met, the contrail optical depth was approximated using:

- the ice water content, calculated as a function of temperature obtained from contrail observations (Schumann et al., 2017);
- the contrail ice particle effective radius, estimated via an empirical function of the contrail age (Schumann et al., 2017);
- the contrail depth, which is set to be constant and equal to 200 m (in agreement with Grewe et al., 2014b).

Subsequently, the radiative forcing at each point along the trajectory is computed according to the parametric model presented by Schumann et al. (2012), assuming no cloudiness above the contrail (see Chapter 2.3.2). The input for this calculation includes:

- outgoing longwave radiation at the top of atmosphere, contrail temperature, contrail optical depth and effective contrail ice particle radius (to compute the contrail longwave radiative forcing);
- solar direct irradiance at the top of atmosphere, solar zenith angle, contrail optical depth, effective contrail ice particle radius, and the effective albedo (to compute the contrail short-wave radiative forcing).

Lastly, the total contrail radiative forcing is converted into a yearly, global-mean value.

Subsequently, these datasets have been used to identify simple relationships between local atmospheric variables and the radiative forcing from non-CO_2 effects, in order to estimate the flight climate impact under any weather pattern within the temporal and geographic scope of the original dataset (North Atlantic, winter and/or summer). The main steps of this approach are described in the following section.

3.4.2 Development of the algorithmic Climate Change Functions (aCCFs v1.0)

The development of the aCCFs is first presented by Manen et al. (2019) relatively to H_2O and NO_x aCCFs, and in the Supplement of Yin et al. (2023) for the case of contrail aCCFs. The aCCFs development starts from the selection of weather variables, which are candidates to be used as proxy for estimating the climate impact of non-CO_2 effects. This selection is based on the physical and chemical processing determining the non-CO_2 climate impact of aviation. Table 3.3 lists the weather variables which were considered as candidates in this phase. For example, potential vorticity PV [PVU] is among the weather variables taken into account to estimate the radiative forcing from H_2O emissions, as it indicates the expected life-time of the atmospheric concentration perturbation, i.e. longer in the stratosphere (characterized by a slow air turnover) than in the troposphere (where it is quickly removed from the atmosphere via the hydrological cycle). The radiative forcing resulting from NO_x emissions can be expected to show a correlation with the geopotential ϕ [$m^2\ s^{-2}$], since it reflects the transport pathways and their strength in advecting the emitted species, and with factors influencing the local NO_x chemistry, such as temperature T [K] and irradiance F_{in} [W^{-2}]. The radiative forcing of contrails is dependent on the ambient temperature T [K], top net thermal radiation TTR [W m^{-2}], and the solar zenith angle SZA, as explained in Chapter 3.4.1. Subsequently, four candidate algorithms were selected via regression analysis.

Lastly, one formula was chosen by qualitatively comparing the four options based on five criteria (Manen et al., 2019):

1. minimize the *residua variability* over the latitude-longitude field, averaging over days and altitude, in order to capture the horizontal patterns;
2. minimize the residual standard error and maximize the adjusted regression coefficient R^2, to compare *absolute accuracy* of the algorithms;
3. applicability of the algorithms to situations different from those used to calculate the CCF, to evaluate the *external veracity* of the formulas;
4. strength of the argumentation supporting the causal relationship between the weather variables and the ATR20 estimates, based on *background knowledge* of the relevant atmospheric processes;
5. minimize the amount of parameters (*parsimony*).

As a result of this approach, the following set of formulas was obtained[5]:

$$\mathrm{aCCF}_{H_2O} = \alpha_0 + \alpha_1 |PV| \qquad [\mathrm{K\ kg(fuel)^{-1}}] \quad (3.12)$$

$$\mathrm{aCCF}_{O_3} = \begin{cases} \beta_{00} + \beta_{01} T + \beta_{10} \phi + \beta_{11} T \phi, & \mathrm{aCCF}_{O3} > 0 \\ 0, & else \end{cases} \qquad [\mathrm{K\ kg(NO_2)^{-1}}] \quad (3.13)$$

$$\mathrm{aCCF}_{CH_4} = \begin{cases} \gamma_{00} + \gamma_{01} \phi + \gamma_{10} F_{in} + \gamma_{11} \phi F_{in}, & \mathrm{aCCF}_{CH_4} < 0 \\ 0, & else \end{cases} \qquad [\mathrm{K\ kg(NO_2)^{-1}}] \quad (3.14)$$

$$\mathrm{aCCF}_{night-contrail} = \begin{cases} F_{\mathrm{RF} \rightarrow \mathrm{P\text{-}ATR20}} \left(\delta_0 + \delta_1 10^{\delta_2 T} \right), & T > T^* \\ 0, & else \end{cases} \qquad [\mathrm{K\ km(contrail)^{-1}}] \quad (3.15)$$

$$\mathrm{aCCF}_{day-contrail} = F_{\mathrm{RF} \rightarrow \mathrm{P\text{-}ATR20}} (\kappa_0 + \kappa_1 TTR) \qquad [\mathrm{K\ km(contrail)^{-1}}] \quad (3.16)$$

Moreover, a constant aCCF for the ATR20 from CO_2 emission is included to complete the set:

$$\mathrm{aCCF}_{CO_2} = \lambda_0 \qquad [\mathrm{K\ kg(fuel)^{-1}}] \quad (3.17)$$

In Manen et al. (2019), the quality of the H_2O and NO_x aCCFs is assessed. This study evaluates the water vapour aCCF as being well representative of the geographical and temporal variability of the climate impact of H_2O emissions, based on the criteria listed above. The NO_x-O_3 aCCF is rated lower than the H_2O aCCF, but is nevertheless supported by pre-existing knowledge of this aviation effect. The quality of the NO_x-CH_4

[5]Note that the day-time contrail aCCF is given in terms of the outgoing long-wave radiation *OLR* [W m^{-2}] in Yamashita et al. (2020) and Yin et al. (2023). However, *OLR* is defined as a positive quantity (as in Yin et al., 2023, Figure S6), while Eq. (3.16) requires a negative argument to return the correct results. The ECMWF convention defines the top net thermal radiation *TTR* [W m^{-2}] as the longwave radiation emitted to space at the top of the atmosphere (i.e. equal to *OLR*), with negative sign. More details are available at https://codes.ecmwf.int/grib/param-db/209 (Accessed: 9 July 2024).

aCCF is the lowest, leading to larger uncertainties in its representation of the spatio-temporal variability of NO_x emissions effects on methane. Relatively to the contrail aCCFs, their quality was mostly satisfactory when short-lived (<6h) or strongly-warming contrails where assessed. As the latter are the most relevant to identify and avoid via trajectory optimization, the contrail aCCFs are expected to be an appropriate tool to evaluate the mitigation potential of aircraft trajectory optimization (see supplement material of Yin et al., 2023).

Non-CO_2 effect	Weather variables	
	Candidates	Selected
H_2O	p_{trop}, p, PV, q	PV
NO_x-O_3	q, T, ϕ, F_{in}	T, ϕ
NO_x-CH_4	ϕ, F_{in}, Θ, ATR20_{O_3}	ϕ, F_{in}
Night-time contrails	T, TTR	T
Day-time contrails	T, TTR, SZA	TTR

Table 3.3: Weather variables taken into account to derive the algorithmic climate change functions (aCCFs) are pressure at tropopause p_{trop} [Pa] (using the World Meteorological Organization definition of tropopause), pressure at emission p [Pa], potential vorticity PV [PVU], specific humidity q [kg/kg], atmospheric temperature at emission T [K], geopotential ϕ [m^2 s^{-2}], irradiance F_{in} [W^{-2}], potential temperature Θ [K], average temperature response in 20 years from NO_x-O_3 ATR20_{O_3} [K $kg(NO_2)^{-1}$], top net thermal radiation TTR [W m^{-2}], solar zenith angle SZA [degrees].

The coefficients values of the first consistent set of aCCFs (aCCFs v1.0) are provided in Table 3.4 (Yin et al., 2023). Note that the datasets used to derive the aCCFs were computed for atmospheric conditions occurring over the North Atlantic during specific seasons (winter in the case of contrails, winter and summer for H_2O and NO_x), thus the application of the resulting aCCF v1.0 in other seasons and/or geographic locations is outside the original temporal and geographical scope of these functions. This is very likely an important limitation of the aCCF v1.0, which motivates on-going research which aims at computing new CCFs, with an extended spatio-temporal coverage compared to those presented by Frömming et al. (2021), computed within the REACT4C project. Subsequently, these extended CCFs can be employed as input to develop a new set of aCCFs, possibly including formulas specific for different seasons and regions (e.g., different formulas would be provided for tropic and extra-tropic latitudes).

3.4.3 The EMAC submodel ACCF v1.0

This section provides a description of how the aCCFs v1.0 are calculated within the EMAC model. As described in Chapter 3.1, the EMAC model includes submodels which are responsible for specific tasks. In particular, the aCCFs calculation is performed by the ACCF submodel. Here, the focus is on the first version of such submodel, ACCF v1.0,

More details about the ACCF submodel are published in *Yin, F., Grewe, V., Castino, F., Rao, P., Matthes, S., Dahlmann, K., Dietmüller, S., Frömming, C., Yamashita, H., Peter, P., Klingaman, E., Shine, K. P., Lührs, B., and Linke, F.: Predicting the climate impact of aviation for en-route emissions: the algorithmic climate change function submodel ACCF 1.0 of EMAC 2.53, Geosci. Model Dev., 16, 3313–3334, https://doi.org/10.5194/gmd-16-3313-2023, 2023.*

presented by Yin et al. (2023). This paper presents the first consistent set of aCCF formulas, estimating the climate impact of CO_2 and non-CO_2 climate effects of aviation. In this application of the aCCFs, the weather variables required to calculate the aCCFs are provided by the base model ECHAM5, and by the submodels Orbit, TROPOP, and RAD. Moreover, the CONTRAIL submodel provides potential contrail coverage (defined in Chapter 3.3), which is used to determine whether persistent contrail can form or not. Only in the former case, values of the contrail aCCFs are calculated, otherwise the $ATR20_{contr}$ value is set to zero.

Coefficient	Estimate	Unit
	Water vapour	
α_0	2.11×10^{-16}	K kg(fuel)$^{-1}$
α_1	7.70×10^{-17}	K kg(fuel)$^{-1}$ PVU^{-1}
	NO_x-ozone	
β_{00}	-2.64×10^{-11}	K kg(NO_2)$^{-1}$
β_{01}	1.17×10^{-13}	K kg(NO_2)$^{-1}$ K^{-1}
β_{10}	2.46×10^{-16}	K kg(NO_2)$^{-1}$ (m^2 s^{-2})$^{-1}$
β_{11}	-1.04×10^{-18}	K kg(NO_2)$^{-1}$ (K m^2 s^{-2})$^{-1}$
	NO_x-methane	
γ_{00}	-4.84×10^{-13}	K kg(NO_2)$^{-1}$
γ_{01}	9.79×10^{-19}	K kg(NO_2)$^{-1}$ (m^2 s^{-2})$^{-1}$
γ_{10}	-3.11×10^{-16}	K kg(NO_2)$^{-1}$ (W m^{-2})$^{-1}$
γ_{11}	3.01×10^{-21}	K kg(NO_2)$^{-1}$ (W m^{-2} m^2 s^{-2})$^{-1}$
	Night-time contrail	
δ_0	-1.03×10^{-10}	Wm^{-2}
δ_1	0.0073×10^{-10}	Wm^{-2}
δ_2	0.0107	K^{-1}
	Day-time contrail	
κ_0	-1.7×10^{-10}	Wm^{-2}
κ_1	-0.0088×10^{-10}	-
	Carbon dioxide	
λ_0	7.48×10^{-16}	K kg(fuel)$^{-1}$
	Other parameters	
$F_{\text{RF}\rightarrow\text{P-ATR20}}$	0.0151	K (Wm^{-2})$^{-1}$
T^*	201	K

Table 3.4: Coefficients values of the first consistent set of aCCFs, the aCCFs v1.0 (Yin et al., 2023).

The specific coefficients set for the aCCFs v1.0 are listed in Table 3.4. Using these coefficients, the aCCFs provide estimates in terms of the climate metric average temperature response (ATR) over 20 years, assuming a pulse emission (P-ATR20). Moreover, the aCCFs formula can be multiplied by constant factors, for example, to take into account the efficacy of the different non-CO_2 effects of aviation, and to provide estimates in different climate metrics than P-ATR20 (Chapter 2). Table 3.5 lists the efficacy terms and the factors enabling the conversion from P-ATR20 to F-ATR20

(assuming a future emission scenario instead of pulse emission) used in Chapter 4 and Chapter 6. The ATR climate metric is recommended by Megill et al. (2024) to evaluate climate policies: Among its advantages, Megill et al. (2024) reports that ATR is stable over time, readily comparable to existing, temperature-based climate targets and policies, and simple to understand. By assuming a future emission scenario and choosing a relatively short time horizon of 20 years, the reduction of the near-term impacts of short-lived effects is prioritized. Therefore, the F-ATR20 climate metric is chosen to estimate the potential benefits that can be achieved via optimized aircraft trajectories in Chapter 4 and Chapter 6.

Non-CO_2 effect	**Efficacy term**	**Conversion factor P-ATR20 → F-ATR20**
Water vapour	1.0	14.5
NO_x-ozone	1.37	14.5
NO_x-methane	1.18	10.8
Contrail cirrus	0.42	13.6
Carbon dioxide	1.0	9.4

Table 3.5: Efficacy terms and the factors enabling the conversion from P-ATR20 to F-ATR20, i.e. assuming a future emission scenario instead of pulse emission (Yin et al., 2023).

Figure 3.6 illustrates an example of the daily mean patterns of the aCCFs as computed by the ACCF submodel over the North Atlantic and European regions, which are the focus of this thesis. The aCCF fields are interpolated at an altitude of 250 hPa. Note that the aCCFs are expressed in different units (K per kg(NO_2), kg(fuel), or km(flown)), therefore the magnitudes of the different effects cannot be directly compared. First of all, it can be noticed that both the ozone and methane impact from NO_x emissions tend to increase (considering the absolute magnitude) moving towards lower latitudes, due to the higher photochemical activity here (Figure 3.6a-b). Contrarily, the aCCF of water vapour emissions increases moving towards the polar region, possibly due to the decrease in the height of the tropopause (Figure 3.6c). The contrail aCCFs have been multiplied by the potential contrail coverage in Figure 3.6, in order to also visualize which areas would be most sensitive to contrail formation. Therefore, the units here are K/km(flown), instead of K/km(contrail). A key message of this figure is that contrail aCCFs present strong horizontal gradients. Therefore, when this function is used as optimization objective for aircraft trajectories, sharp decreases can be obtained via small deviations.

Using the ACCF submodel, Rao et al. (2022) demonstrated that trajectories optimized with respect to the NO_x-O_3 aCCF lead to a reduction of the radiating forcing from NO_x-O_3. To achieve this, as first step, Rao et al. (2022) conducted simulations with EMAC and its submodels ACCF and AirTraf, to identify cost optimal and NO_x-O_3 optimal trajectories. As a result of this phase, two emission inventories were obtained, describing the altitude and geographic location of aircraft emissions under each routing strategy. In the second step, a different configuration of EMAC is employed, to simulate the atmospheric perturbation caused by NO_x-O_3 emissions from the two distinct inventories, and to compare the resulting radiative forcing (Rieger et al., 2018; Dietmüller

et al., 2016). This case study confirmed that the NO_x-O_3 aCCF is effective as optimization objective, i.e. that NO_x-O_3 optimal trajectories result in a lower radiating forcing from NO_x-O_3 than cost-optimal trajectories. However, Rao et al. (2022) noted that the NO_x-O_3 aCCF cannot fully capture the spatio-temporal variability of the radiative forcing caused by the impact of NO_x emissions on the atmospheric ozone. This is expected, since this formula heavily simplifies the effect of complex physical-chemical processes. The application of similar approaches is recommended to be applied to other aCCF formulas, in order to test their effectiveness in assessing the mitigation potential of optimized aircraft trajectories. As this is the focus of on-going research, the aCCFs v1.0 are presented as a prototype version, and it is recommended to avoid their use outside their original temporal and geographical scope (winter and/or summer seasons, North Atlantic atmospheric dynamics).

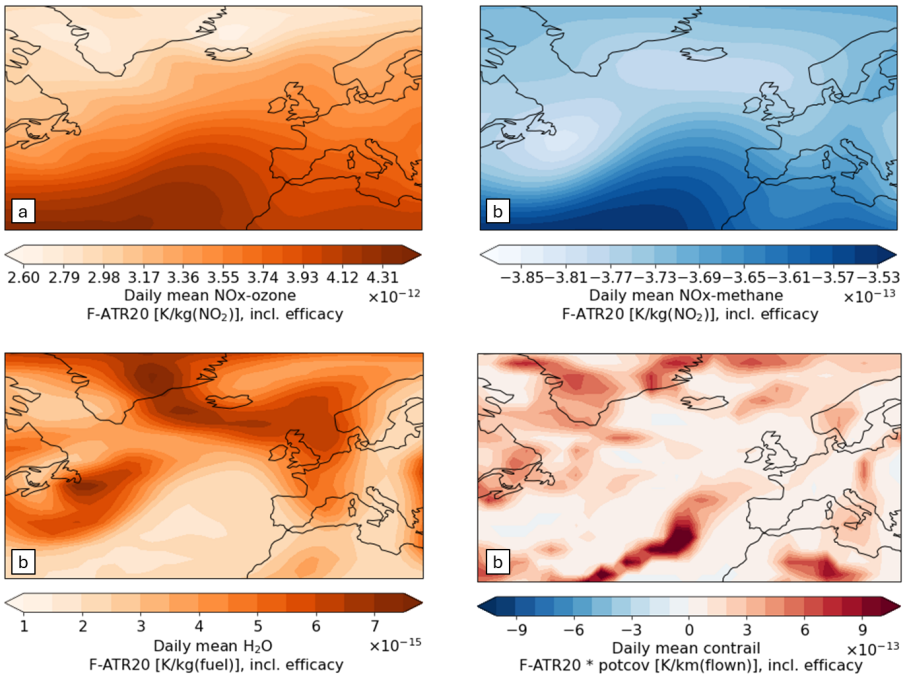


Figure 3.6: Example of daily geographical variability at 250 hPa of the aCCFs of NO_x-O_3 (Figure 3.6a), NO_x-CH_4 (Figure 3.6b), H_2O (Figure 3.6c), and contrails (Figure 3.6d). The patterns shown here are relative to 1 December 2018.

3.5 Summary

This Chapter described the main characteristics of the methods that were further developed (Chapter 4) and applied (Chapters 5-6) in this thesis. To identify and analyse eco-efficient trajectories, an atmospheric general circulation model (ECHAM5) is employed, coupled to several submodels via the interface provided by the Modular Earth Submodel System (MESSy2). This base model is referred to as EMAC (ECHAM/MESSy

Atmospheric Chemistry model). This Chapter outlines the relations between the base model EMAC and some selected submodels, which are the most relevant within the scope of this research: AirTraf, CONTRAIL, and ACCF. One of the main advantages of using this modelling chain is the possibility of optimizing an air traffic sample over several seasons, using the air traffic simulator AirTraf. The AirTraf submodel successfully optimizes aircraft trajectories based on several objective functions, including operating costs, contrail distance, and climate effects.

However, the model presents also important limitations. Some limitations discussed in this Chapter arise from the necessity of containing the computational effort. For example, the horizontal resolution of $2.8^\circ \times 2.8^\circ$ in latitude and longitude does not resolve ice supersaturation regions (ISSRs), which have typical horizon dimensions of $\mathcal{O}(100\ \text{km})$. To identify ISSRs and, subsequently, regions of the atmosphere where persistent contrails are likely, a parameterization implemented in the submodel CONTRAIL is used. This parameterization enables the computation of the potential contrail (cirrus) coverage, i.e., the (cloud-free) fraction of the model grid-box where contrails can persist.

Moreover, climate effects of aviation result from the complex interaction of atmospheric processes, acting over a wide range of spatial and temporal scales. Therefore, these cannot be explicitly simulated, especially while evaluating a large number of trajectories within the resolution of multi-objective optimizations. As an alternative, a simple set of formulas, the algorithmic Climate Change Functions (aCCFs) have been derived, in order to quickly estimates the climate effects of aircraft emissions in terms of average temperature response in 20 years (ATR20). The aCCFs have been implemented in the ACCF submodel, enabling the inclusion of non-CO_2 climate effects in the aircraft trajectory optimization performed bu the submodel AirTraf. However, the aCCFs are affected by significant uncertainties, e.g. arising from the simple statistical methods and the limited temporal and geographic scope of the dataset used in their derivation. Despite such limitations, previous studies confirmed that the AirTraf submodel can successfully reduce the climate impact of emitted NO_x via its impact on atmospheric ozone, when the relative aCCF is set as optimization objective. Moreover, the modelling chain described here, and its development presented in the next Chapter, can be easily adapted to account for future improvements in our understanding and simulation capabilities of non-CO_2 effects of aviation.

4

Model development: SolFinder 1.0 decision-making tool and its application in AirTraf 3.0

The optimization of aircraft trajectories involves balancing operating costs and climate impact, which are often conflicting objectives. To achieve compromise optimal solutions, higher-level information such as preferences of decision-makers must be taken into account. This Chapter introduces the SolFinder 1.0 module, a decision-making tool designed to identify eco-efficient aircraft trajectories, which allow the reduction of the flights climate impact with limited cost penalties compared to cost-optimal solutions. SolFinder 1.0 offers flexible decision-making options that allow users to select trade-offs between different objective functions, including fuel use, flight time, NO_x emissions, contrail distance, and climate impact. The module is included in the AirTraf 3.0 submodel (Chapter 3.2), which optimizes trajectories under atmospheric conditions simulated by the ECHAM/MESSy Atmospheric Chemistry model (EMAC, Chapter 3.1). This Chapter focuses on the ability of the module to identify eco-efficient trajectories while solving a bi-objective optimization problem that minimizes climate impact and operating costs. SolFinder 1.0 enables users to explore trajectory properties at varying locations of the Pareto fronts without prior knowledge of the problem results and to identify solutions that limit the cost of reducing the climate impact of a single flight.

This Chapter is based on *Castino, F., Yin, F., Grewe, V., Yamashita, H., Matthes, S., Dietmüller, S., Baumann, S., Soler, M., Simorgh, A., Mendiguchia Meuser, M., Linke, F., and Lührs, B.: Decision-making strategies implemented in SolFinder 1.0 to identify eco-efficient aircraft trajectories: application study in AirTraf 3.0, Geosci. Model Dev., 17, 4031–4052, https://doi.org/10.5194/gmd-17-4031-2024, 2024.*

4.1 Introduction

Currently, air traffic optimization focuses on minimizing economic penalties, e.g., identifying aircraft trajectories that lead to minimal operating cost. Minimizing the operating cost and the climate impact of a single flight are expected to be conflicting objectives of aircraft trajectory optimization (Yamashita et al., 2021). This implies that, in most cases, it is not possible to identify a solution that simultaneously minimizes both objectives. Therefore, optimizing an aircraft trajectory with respect to its economic cost and climate impact, a set of Pareto-optimal solutions can be identified. To select a single trajectory among this set of optimal solutions, a wide range of decision-making strategies can be employed (Kou et al., 2012; Pasman et al., 2022). In this Chapter, a new decision-making tool, the SolFinder 1.0 module, is presented. This tool was developed with the aim of identifying aircraft trajectories leading to a significant reduction of the flight climate impact, while limiting the increase in economic costs: these solutions are defined as *eco-efficient* aircraft trajectories. This tool satisfies the following requirements:

- it is applicable to any set of Pareto-optimal solutions resulting from the optimization of a single aircraft trajectory;
- it is suitable for identifying compromise solutions between any number of objective functions;
- in particular, when applied for the bi-objective optimization of operating cost and climate impact, it is capable of identifying eco-efficient solutions.

To satisfy these requirements, the following options have been selected and are available in the first version of SolFinder: (1) a strategy relying on the VIKOR method (abbreviation from its Serbian name: *Vlse Kriterijumska Optimizacija Kompromisno Resenje*, presented by Opricovic et al. (2004)) to identify eco-efficient solutions; (2) a strategy selecting the Pareto-optimal solution closest to a target percentage change in one of the objectives, such as the economic costs; (3) a decision-making method which combines the previous two options, applying the VIKOR method while limiting the change in one of the objectives. The SolFinder module has been coupled to the ECHAM/MESSy Atmospheric Chemistry (EMAC, Jöckel et al., 2010) submodel AirTraf (Yamashita et al., 2020), as part of the AirTraf extension for the efficient resolution of multi-objective optimization problems. This modelling chain enables users to select Pareto-optimal solutions matching specific preferences of decision-makers, e.g., eco-efficient aircraft trajectories, and to explore their dependency on the atmospheric natural variability.

In Sect. 4.2, the development of the AirTraf submodel of EMAC is described, before presenting the decision-making strategies included in SolFinder 1.0 (Sect. 4.3). In Sect. 4.4, an example application of the selected decision-making strategies is illustrated, using the Pareto-optimal solutions that are identified by AirTraf when a European air traffic sample of 100 night-time flights is optimized with respect to economic cost and climate impact. Sect. 4.5 includes a comparison of these results to those obtained in previous studies, and uncertainties affecting these results are discussed. The key messages are summarized in Sect. 4.6.

4.2 Multi-objective optimization with AirTraf

For the present study, EMAC (ECHAM5 version 5.3.02, MESSy version 2.55.0) is employed in the T42L31ECMWF-resolution, as described in Chapter 3, coupled with its submodel AirTraf (Chapter 3.2). The second version of this air traffic simulator (AirTraf 2.0, Yamashita et al., 2020) allowed the user to solve single-objective optimization problems, minimizing one of several available objective functions, including fuel use, flight time, NO_x emissions, contrail distance, operating costs, and climate impact. The submodel is being expanded to use the same optimization method for the efficient resolution of multi-objective optimization problems. As a result, it is possible to simultaneously optimize two or more objective functions, without combining such functions into a single objective. This is particularly convenient when aiming to identify eco-efficient aircraft trajectories under a large number of weather conditions. In fact, a conversion factor would be necessary to combine climate impact and operating costs into a single objective functions. However, this factor (e.g., as defined by Simorgh et al., 2023, Eq.7) is affected by a large variability over different flights and days, thus it is difficult to find a general value of the factor which can be applicable to optimize large air traffic samples over long-term simulations. Due to this AirTraf expansion for the resolution of multi-objective optimization problems, a decision-making module became necessary to ensure that a single optimal solution is identified, and its properties are evaluated and stored by the model. This task can be performed by the SolFinder 1.0 module presented in this Chapter. Therefore, SolFinder has been coupled to AirTraf to select one optimal solution from the full Pareto set, reducing the computational effort of the model.

In the development of the decision-making strategies implemented in SolFinder 1.0, the underlying goal has been to find eco-efficient aircraft trajectories, compromising between the optimization of climate impact and operating costs. Hence, the definitions of these objective functions within AirTraf are included here. The economic costs of the flights are represented by the Simple Operating Costs (SOC), defined as in Eq. (4.1):

$$\mathrm{SOC} = c_t \sum_{i=1}^{n_{wp}-1} \mathrm{TIME}_i + c_f \sum_{i=1}^{n_{wp}-1} \mathrm{FUEL}_i \tag{4.1}$$

where TIME_i and FUEL_i represent the flight time and fuel used at the i^{th} flight segment, respectively, while $c_t = 0.75$ \$/s and $c_f = 0.51$ \$/kg are the unit time and unit fuel costs (Burris, 2015; Yamashita et al., 2020). The climate impact of each aircraft trajectory is measured in this study in terms of Average Temperature Response over 20 years (ATR20), as provided by the ACCF submodel (Manen et al., 2019; Yin et al., 2023). Note that the approaches implemented in AirTraf and SolFinder are independent from the choice of climate metric. Therefore, this can be changed to any other metric in future applications. The total climate impact $\mathrm{ATR20}_{\mathrm{tot}}$ of each aircraft trajectory is determined summing the contribution from the main climate effects:

$$\mathrm{ATR20_{tot}} = \sum_{i=1}^{n_{wp}-1} \Big[\mathrm{ATR20_{CO_2},}_i + \mathrm{ATR20_{H_2O},}_i \tag{4.2}$$

$$+\mathrm{ATR20_{NO_x\text{-}O_3},}_i + \mathrm{ATR20_{NO_x\text{-}CH_4},}_i + \mathrm{ATR20_{contrails},}_i \Big] \tag{4.3}$$

where each addend represents, from left to right, the ATR20 at the i^{th} flight segment from (1) carbon dioxide (CO_2), (2) water vapour (H_2O), (3) ozone (O_3) from emission of NO_x, (4) methane (CH_4) from emission of NO_x, and (5) contrails. The term $\mathrm{ATR20_{NO_x\text{-}CH_4},}_i$ includes the changes in primary mode ozone induced by the reduced CH_4 atmospheric concentration, while it neglects the feedback from stratospheric water vapour (Yin et al., 2023). The present study uses ATR20 as climate metric, assuming a business-as-usual Future emission scenario (F-ATR20). Alternative climate metrics can also be used, e.g, considering a time horizon of 100 years (ATR100). A detailed description of the climate metric conversion is presented in Dietmüller et al. (2023).

4.3 SolFinder module

In this section, the decision-making strategies implemented in SolFinder 1.0 are described. The overall aim is to solve a multi-objective optimization problem minimizing a set of N objective functions f_n, with $n = 1, 2, ..., N$. If two or more objective functions are conflicting, a set of Pareto-optimal solutions, P, is identified. The values $f_{n,j}$ of the objective functions are assigned to each Pareto-optimal solution $p_j \in P$, with $j = 1, 2, ..., J$. Subsequently, a decision-making strategy intervenes, to select one solution $p_{\mathrm{rec}} \in P$ which is the *recommended* solution according to the decision-maker criteria. The following strategies towards the resolution of this problem are included: (1) option selecting a solution based on its weighted distance from an ideal (usually, not feasible) solution (VIKOR method, Sect. 4.3.1) for the identification of eco-efficient trajectories (Sect. 4.3.2); (2) option leading to a target percentage change in one of the objective functions, with respect to its minimum value (Sect. 4.3.4); (3) option combining the previous two strategies, limiting the change in one of the objective functions while applying the VIKOR method (Sect. 4.3.5); (4) selection of one of the extremes of the Pareto-optimal set (Sect. 4.3.6).

A large variety of multi-criteria decision-making methods is currently available to select one solution among a set of optimal options (Wang et al., 2017; Sałabun et al., 2020). In a preliminary phase of this research, different options among the most popular techniques were considered, including GRA (Grey Relational Analysis, Wang et al., 2017), TOPSIS (Technique for Order Preference by Similarity to Ideal Solution, Chen et al., 1992), and VIKOR (abbreviation from its Serbian name: *Vlse Kriterijumska Optimizacija Kompromisno Resenje*, Sect. 4.3.1). These options have been implemented in a python library[1], in order to apply them on test cases, and compare their effectiveness in identifying eco-efficient aircraft trajectories. The VIKOR method (Opricovic, 1998; Opricovic et al., 2004) was identified as a suitable candidate to translate the definition of

[1]See Supplement material and Castino (2023).

eco-efficient solutions into a decision-making algorithm. This is due to its peculiarity of recommending more than one solution, if certain criteria are not met by a single solution (Sect. 4.3.1). This allows flexible identification of a region of the Pareto-front (e.g., the section of the Pareto-front leading to a small change in the economic costs), within which the user is able to choose their preferred solution (e.g., the solution with the largest climate impact reduction). Moreover, no *a priori* knowledge on the optimization problem expected results is needed. To apply the VIKOR method, only the following information is provided as input, translating the user preferences in mathematical terms:

- the relative importance of N objective functions, represented by the weights $w_n \geq 0$, such that $\sum_n w_n = 1$, with $n = 1, 2, ..., N$.
- the relative importance of group utility (preference towards achieving the greatest benefit) and individual regret (preference towards avoiding large penalties), represented by the parameter γ, with $0 < \gamma < 1$. If $\gamma > 0.5$, the *majority rule* principle is applied; contrarily, $\gamma < 0.5$ implies the application of the *veto* principle; lastly, $\gamma \approx 0.5$ represents a *voting by consensus* strategy (Opricovic et al., 2004).

4.3.1 VIKOR method

In this Sect. 4.3.1, the steps characterizing the VIKOR method are quoted, as they were introduced and described in Opricovic (1998) and Opricovic et al. (2004). Figure 4.1 illustrates the main working principles of the VIKOR method. The x-axis represents the normalized distance from the minimum value of f_1, scaled by its relative weight w_1. As an example, this weight is set to $w_1 = 0.2$, thus the x-axis ranges from 0 to 0.2. Similarly, the y-axis represents the normalized distance from the minimum value of f_2, weighted using $w_2 = 0.8$. The axes intersect at the reference point i_{best}, defined as the best *ideal* (i.e., usually not feasible) solution. Opposite to i_{best}, it is possible to identify i_{worst}, which assumes the worst values of f_n ($f_{n,\text{worst}}$) found among the set of Pareto-optimal solutions. For example, when aiming at minimizing f_n, i_{worst} corresponds to the maximum f_n among the Pareto set. The grey points in Figure 4.1 indicate the location of the Pareto-optimal solutions, relative to i_{best}. In fact, the VIKOR method ranks the Pareto-optimal solutions using i_{best} as a reference point. Hence, the first step consists of identifying such a reference point, by determining the best values of each of the objectives, $f_{n,\text{best}}$. Since the aim is to minimize the objective functions, the following definitions of $f_{n,\text{best}}$ and $f_{n,\text{worst}}$ are used:

$$f_{n,\text{best}} = \min_j f_{n,j}, \qquad f_{n,\text{worst}} = \max_j f_{n,j}, \qquad n = 1, 2, ..., N, \qquad j = 1, 2, ..., J \tag{4.4}$$

In Figure 4.1, the Pareto-optimal solution p_j is highlighted. In the second step of the VIKOR method, two quantities are calculated for each point in the Pareto set: $S(p_j)$, which measures the *group utility* of the solution p_j, and $R(p_j)$, which represents its *individual regret*. In other words, $S(p_j)$ measures the overall distance of p_j from i_{best}, taking into account all the optimization objectives. On the other hand, $R(p_j)$ measures the largest distance of p_j from i_{best} considering each objective individually. These quantities are defined by Eqs. (4) and (5), respectively:

$$S(p_j) = \sum_{n=1}^{N} w_n \frac{f_{n,\text{best}} - f_{n,j}}{f_{n,\text{best}} - f_{n,\text{worst}}} \tag{4.5}$$

$$R(p_j) = \max_n \left[w_n \frac{f_{n,\text{best}} - f_{n,j}}{f_{n,\text{best}} - f_{n,\text{worst}}} \right] \tag{4.6}$$

where w_n is the relative weight of each objective f_n.

The geometric representation of $S(p_j)$ and $R(p_j)$ is illustrated in Figure 4.1. It is possible to deduce from Eqs. (4) and (5) and from Figure 4.1 that lower values of $S(p_j)$ and $R(p_j)$ are preferable. These measures of the distance of p_j from i_{best} are combined in the value $Q(p_j)$, which is used as main ranking parameter by the VIKOR method. The value of $Q(p_j)$ is calculated using Eq. (6):

$$Q(p_j) = \gamma \frac{S_j - \min_j S_j}{\max_j S_j - \min_j S_j} + (1-\gamma) \frac{R_j - \min_j R_j}{\max_j R_j - \min_j R_j} \tag{4.7}$$

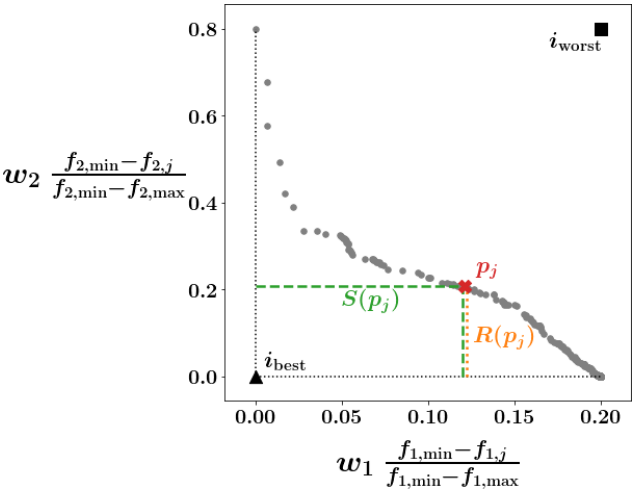


Figure 4.1: Illustration of the VIKOR method applied to a bi-objective optimization problem, minimizing f_1 and f_2. In this example, the relative weights are set to $w_1 = 0.2$ and $w_2 = 0.8$, thus the x (y) axis ranges from 0.0 to 0.2 (0.8). The grey dots represent Pareto-optimal solutions. The red cross indicates the Pareto-optimal solution p_j. The green dashed line represents $S(p_j)$, while the orange dotted segment represents $R(p_j)$. The reference points i_{best} and i_{worst} are indicated by the black triangle and black square, respectively.

The next step consists in creating three ranking lists of the Pareto-optimal solutions, sorting them by S, R, and Q. We define p_i as the Pareto-optimal solution at the i^{th} position in the list sorted by Q. Consequently, the first compromise solution to be recommended is p_1, which minimizes Q: $Q(p_1) = \min_j Q(p_j)$. The following conditions are then evaluated:

1. **acceptable advantage**: $Q(p_2) - Q(p_1) \geq \frac{1}{J-1}$

If this condition is not verified, a set of Pareto-optimal solutions p_v ($v = 1, 2, ..., M$) is recommended, where M is the maximum value for which $Q(p_M) - Q(p_1) \leq \frac{1}{J-1}$ is true.

2. **acceptable stability**: p_1 is the best ranked solution not only by Q, but also by S and R.

   If this condition is not satisfied, both p_1 and p_2 are recommended.

Therefore, the application of the VIKOR method results in the identification of either one optimal solution, p_1, or a subset of optimal solutions, p_v ($v = 1, 2, ..., M$), which are recommended to the decision-maker.

4.3.2 Strategy using VIKOR method to identify eco-efficient trajectories

The SolFinder 1.0 module identifies eco-efficient trajectories using a decision-making option based on the VIKOR method. This method, introduced by Opricovic (1998) and Opricovic et al. (2004), makes use of the overall distance (group utility) and the maximum distance (individual regret) of a Pareto-optimal solution from the minimal values of the optimization objectives to rank the Pareto-optimal solutions. More details on the version of the VIKOR method implemented in SolFinder are included in Sect. 4.3.1. Figure 4.2 illustrates how this decision-making strategy is applied using as an example the bi-objective optimization of a flight with respect to its SOC and ATR20. Firstly, the decision-making module collects all the Pareto-optimal solutions (represented by the grey crosses in Figure 4.2a). Subsequently, the VIKOR method is applied according to the prescribed values of the parameter γ and the relative weights w_n (Figure 4.2b). This leads to a recommended subset of optimal solutions (represented by the blue circles in Figure 4.2c). If the VIKOR method identifies more than one recommended solution, i.e., the solutions p_v ($v = 1, 2, ..., M$) are equally recommended, the model selects the one with the minimum value of the objective function assigned to the lowest weight w_n. In Figure 4.2d, the objective with the lowest relative weight is ATR20 ($w_{\text{ATR20}} = 0.3, w_{\text{SOC}} = 0.7$), thus the model selects the point among the recommended solutions (indicated by the blue circles in Figure 4.2d) with the lowest ATR20 (red triangle in Figure 4.2d). This last step is thus formulated to translate in mathematical terms the definition of eco-efficient aircraft trajectories, i.e., a compromise solution between cost-optimal and climate-optimal solutions, such that the largest possible climate impact reduction is achieved, while keeping the operating costs nearly unchanged with respect to the cost-optimal solution. Using the VIKOR method, a subset of Pareto-optimal solutions is identified, according to the relative importance of the two optimization objectives. Therefore, if the highest weight is assigned to the objective function representing operating costs, the VIKOR method equally recommends a subset of Pareto-optimal solutions close to – or, possibly, including - the cost-optimal extreme point of the Pareto-front. Among this subset of equally recommended solutions, the point leading to the largest climate impact reduction is chosen, i.e., the minimum value of the objective function assigned to the lowest weight.

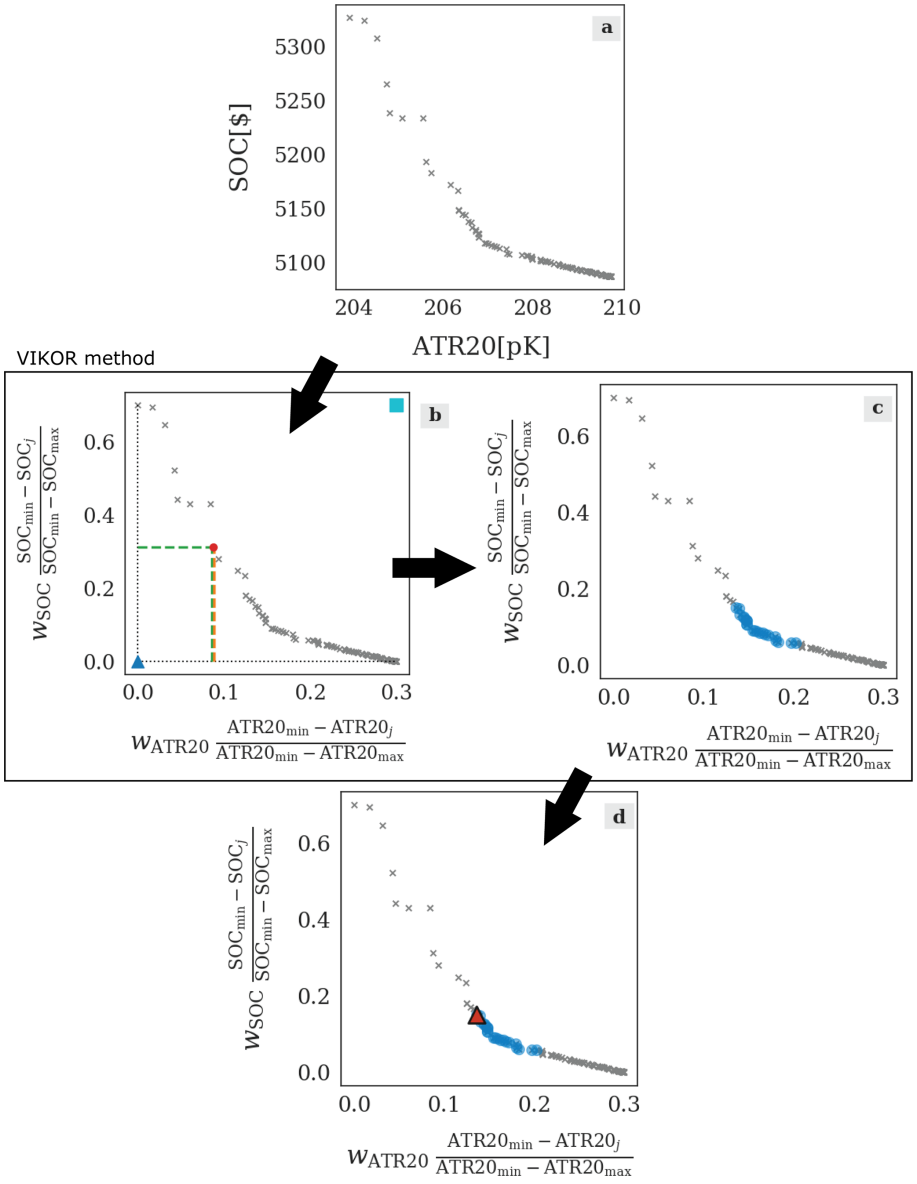


Figure 4.2: Illustration of the steps performed by the eco-efficient decision-making strategy relying of VIKOR. The aircraft trajectories are optimized to minimize SOC and ATR20, resulting in a set of Pareto-optimal solutions (grey crosses). We set $w_{SOC} = 0.7$, $w_{ATR20} = 0.3$, $\gamma = 0.5$. Panel a) shows the Pareto-optimal solutions (grey crosses) collected before applying the decision-making strategy. Panel b) illustrates the application of the VIKOR method (Sect. 4.3.1), thus the axes are scaled as in Fig. A1. This step results in the identification of the subset of recommended solutions, represented by the blue circles in panel c). Panel d) shows the selected solution (red triangle) among the subset of recommended solutions (blue circles).

Therefore, the objective with the highest weight plays a dominant role in the selection of the subset of equally recommended solutions (VIKOR method), while the objective with the lowest weight becomes dominant in the selection of a single solution among this subset. The resulting strategy can be configured to follow the steps listed here:

1. A bi-objective optimization problem is solved to simultaneously minimize the total climate impact ($ATR20_{tot}$ as defined in Eq. (4.2)) and operating costs (SOC, Eq. (4.1)). This step results in the identification of J Pareto-optimal solutions (Figure 4.2a).

2. The VIKOR method is applied, following the steps described in Sect. 4.3.1 (Figure 4.2b).

3. A set of equally recommended solutions are selected in the sections in the Pareto front closest to the cost-optimal solution, by assigning a relatively high weight to the operating costs, i.e., $w_{SOC} > 0.5$ (with $\gamma = 0.5$). Depending on the shape of the Pareto front, this set of solutions extends towards the best ideal solution, i_{best}, allowing for higher climate impact reductions with respect to the cost-optimal solution, while avoiding cost penalties that are not compensated by a climate impact reduction (Figure 4.2c).

4. Among this set of equally recommended solutions, the solution leading to the largest climate impact reduction with respect to the cost-optimal solution is selected, since $w_{ATR} < w_{SOC}$. We define this point as the *eco-efficient* solution among the set of Pareto-optimal options (Figure 4.2d).

4.3.3 Sensitivity of VIKOR parameterization

To understand the effectiveness the VIKOR method with various configurations of γ and w, a set of Pareto-optimal solutions is taken as example, resulting from the bi-objective optimization of an aircraft trajectory with respect to the SOC and ATR20 of the flight. Within this set, a subset of solutions is *recommended* by the VIKOR method with different values of γ and $w = [w_{SOC}, w_{ATR20}]$. The results of this analysis are shown in Figure 4.3. This figure illustrates the impact of varying the weights w by comparing different rows. It is possible to see how, increasing the value of w_{SOC} from 0.2 (Figures 4.3a, 4.3b, 4.3c) to 0.8 (Figures 4.3j, 4.3k, 4.3l), the set of solutions recommended by VIKOR moves closer to the cost-optimal extreme of the Pareto front (0% change in SOC and ATR20). It is less intuitive to understand the impact of changing the parameter γ, which represents the relative importance of group utility. As explained in Sect. 4.3, and according to the formulas included in Sect. 4.3.1, with $\gamma = 0.5$ the same relative importance is assigned to avoiding large penalties in one of the objectives, and to achieving the greatest overall benefit. In the results presented in Sect. 4.4.2, γ is always set to its default value, $\gamma = 0.5$. A value of $\gamma < 0.5$ leads to the application of the veto principle, i.e., if one of the objectives is heavily penalized by selecting a certain Pareto-optimal solution, then it will have a low likelihood to be recommended. Therefore, setting $\gamma = 0.25$ (as in Figures 4.3a, 4.3d, 4.3g, 4.3j) leads to the exclusion of elements located in the external sections of the Pareto-front, because of their distance to the opposite extreme of the Pareto front. On the other hand, when the veto principle is not applied ($\gamma \geq 0.5$), the set of recommended solutions (blue circles) can include the

solution minimising the objective with the highest relative weight. For example, when $w_{SOC} = 0.8$ and $\gamma \geq 0.5$, the solution with minimum SOC is included in the set of Pareto-optimal solutions (Figure 4.3k, 4.3l).

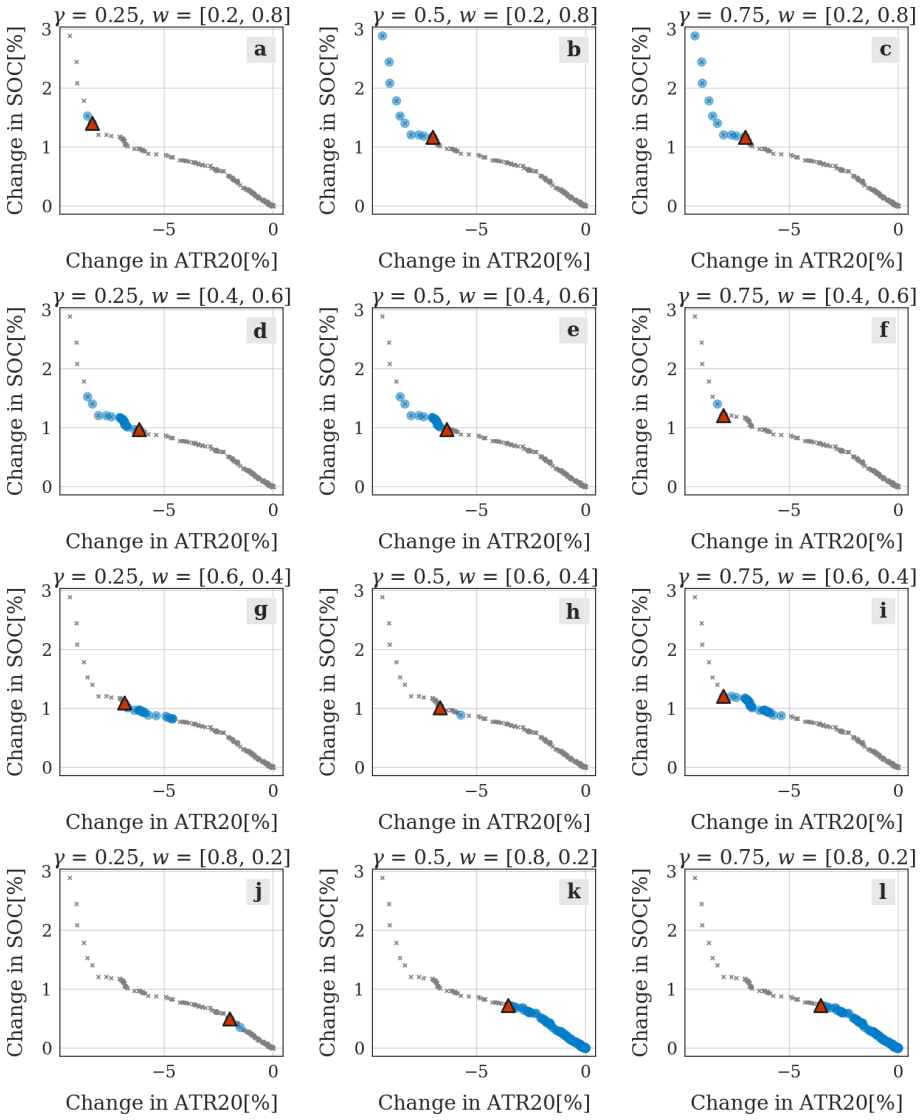


Figure 4.3: Variability of the selected solution (red triangle) using the eco-efficient decision-making method. The grey crosses represent the Pareto-optimal solutions, while the blue circles indicate the subset of solutions recommended by the VIKOR method. The axes show percentage changes in the objective functions, relative to the solution minimizing SOC. In this example, the Pareto front consists of 308 solutions.

This observation is the base for the definition of *eco-efficient* solution given at the end of Sect. 4.3.2, i.e., the solution selected with a high relative weight of SOC (w_{SOC} larger

than 0.5) and $\gamma = 0.5$. Following this definition, the selected solution shown in Figure 4.3k (represented by a red triangle) is an eco-efficient solution. In fact, this solution leads to the maximum $ATR20_{tot}$ reduction among the subset of the solutions recommended by VIKOR (blue circles), while being equally recommended as the cost-optimal solution by the VIKOR method. In other words, the selected solution in Figure 4.3k follows the definition of eco-efficient solutions given in the Introduction, i.e., it allows for a significant reduction in the flight climate impact, while avoiding significant increases in operating costs. However, note that determining the values of γ and w remains an arbitrary choice, which reflects the specific preferences of the decision-maker. Further elements to consider when setting these parameters are discussed later in Sect. 4.4.

4.3.4 Target percentage change in one of the objective functions

In some scenarios, the decision-maker wishes to limit the penalty of one of the objective functions, e.g., to avoid unsustainable increases in the operating costs. Therefore, in the second decision-making strategy, the solution p_{rec} leading to a percentage change in one of the objective functions, f_p, is selected. On the other hand, to obtain the expected outcome, this option requires certain information on the optimization results to be known before solving the problem, such as the typical shape of the Pareto fronts, and reference values at their extreme points. The threshold for the allowable change is specified as a target value x_t. This is translated in the following process:

$$f_{p,\text{ref}} = \min_j f_{p,j}, \qquad j = 1, 2, ..., J \tag{4.8}$$

$$x_j = 100 * \frac{f_{p,j} - f_{p,\text{ref}}}{f_{p,\text{ref}}} \tag{4.9}$$

$$\Delta x_j = |x_j - x_t| \tag{4.10}$$

Therefore, the selected Pareto-optimal solution $p_{rec} \in P$ is the solution corresponding to the relative change x_{rec}, such that $\Delta x_{rec} = \min_j \Delta x_j$.

Figure 4.4 illustrates which solution is selected within a Pareto-optimal set resulting from the resolution of a tri-objective optimization problem, simultaneously minimizing flight time, fuel use, and $ATR20_{tot}$. In this example, $x_t = +0.5\%$ is set as the target percentage change in flight time.

4.3.5 Hybrid option: VIKOR method with target percentage change in one of the objectives

To combine the advantages of the two decision-making strategies presented, a hybrid option is considered, limiting the variability in one of the objective functions while applying the VIKOR method. When this strategy is selected, the decision-maker provides: (1) the configuration of the VIKOR method, setting the parameters γ and w, and (2) a target percentage increase x_t in the objective f_p. Subsequently, the following decision-making process is followed:

1. Apply the VIKOR method and select the recommended solution minimizing the objective function having the lowest weight w_n, as described in Sect. 4.3.1.

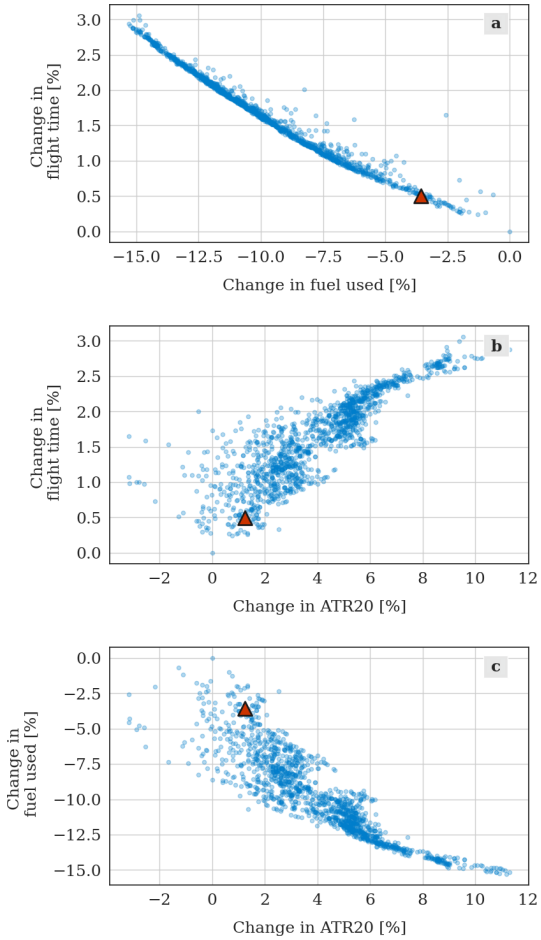


Figure 4.4: Example of selecting the solution among the Pareto-surface matching a target increase in 0.5% in flight time (indicated by red triangles). The blue circles indicate the Pareto-optimal solutions, which result from a tri-objective optimization problem minimizing flight time, fuel use, and $ATR20_{tot}$.

2. Calculate x_p, representing the relative change in f_p of the recommended solution with respect to the minimum value of f_p.

3. If $x_p > x_t$, replace the recommended solution identified in step 1. with the the Pareto-optimal solution leading to a target percentage change x_t in the objective function f_p (in other words, apply the strategy described in Sect. 4.3.4).

This strategy addresses the fact that, with the VIKOR method, no limit in the percentage increase of the objective is set, thus a fraction of the solutions can be affected by changes much larger than the average, as is shown in a later section of this Chapter (Sect. 4.4.2, Figure 4.7). With this hybrid option, the VIKOR method can be employed to identify eco-efficient trajectories, while introducing a constraint on the operating costs,

to prevent increases in the operating costs of some flights that the decision-maker does not accept.

4.3.6 Selecting one extreme of Pareto-optimal set

Lastly, an additional option is considered to select a solution minimizing one of the objective functions f_n, indicated as f_{min}. This simple decision-making process selects the optimal-solution corresponding to the result of a single-objective optimization minimizing f_{min}. Nevertheless, it can be useful to implement this method to identify which values are used as reference during the resolution of the multi-objective optimization problem, and to verify the performance of the model.

4.4 Application of decision-making method to analyse trajectories' variability along Pareto-front

We now present an example study, in which different settings of the decision-making strategies are compared. This application exemplifies how the decision-making strategies can be employed, and what to consider to determine the settings that best translate the decision-maker preference. This example focuses on the suitable settings to identify eco-efficient aircraft trajectories. Nevertheless, SolFinder can also be used to comply with alternative decision-making preferences, by changing the settings of AirTraf and SolFinder.

4.4.1 Simulations set-up

As previously stated, the objective is to identify eco-efficient aircraft trajectories, i.e., trajectories reducing the climate impact at limited changes in the operating costs. Therefore, a bi-objective optimization problem is solved, aiming to simultaneously minimize SOC and ATR20, as defined in Sect. 4.2. We conduct one-month simulations, from 1 January 2018 to 31 January 2018. On each simulation day, 100 night-time flights departing at 00:00 UTC are optimized. Figure 4.5 shows the locations of the airports of origin and destination, which were selected considering the Available Seat Kilometres (ASK) for the European Civil Aviation Conference (ECAC) area in 2018 (Meuser et al., 2022). The same criterion was used to select the A320-214 (CFM56-5B4) as the aircraft/engine type to be simulated. The climate impact of each aircraft trajectory is estimated using the aCCF 1.0A (Matthes et al., 2023). Table 4.1 summarizes the model configuration.

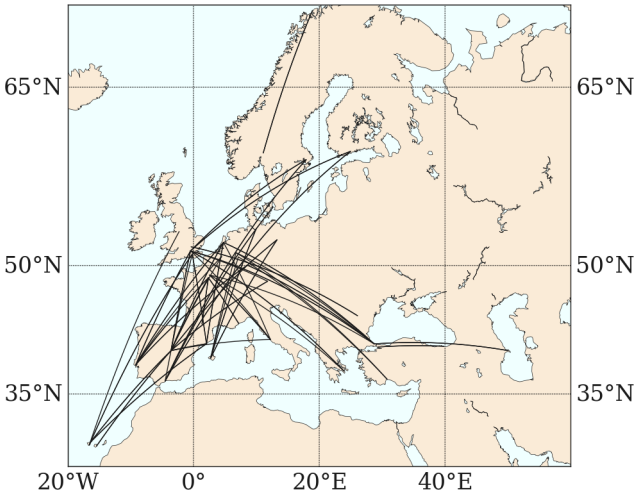


Figure 4.5: Location of the 100 flights included in the air traffic sample. Each curve represents the great circle connecting an origin/destination pair. Note that most origin/destination pairs are connected by two flights, i.e., one for each direction, thus the number of curves is lower than 100.

Table 4.1: Main settings of ECHAM5, ACCF, and AirTraf.

	ECHAM5
Horizontal resolution	T42 (2.81° × 2.81°)
Vertical resolution	L31ECMWF (31 vertical pressure levels up to 10 hPa ~ 30 km)
Time step	12 min
Duration	1-31 Jan. 2018 (each day, 1 month)
	ACCF
Version aCCFs	V1.0A
Climate metric	F-ATR20
Forcing efficacy	Included
	AirTraf
Trajectory waypoints	101
Aircraft / Engine	A320-214 (CFM56-5B4)
Air Traffic Sample	Top 100 routes by ASK for the ECAC area in 2018
Departure time	00:00
Optimization strategy	Multi-objective optimization of: (1) SOC, (2) $ATR20_{tot}$

To compare the effects of using different decision-making strategies, two sets of experiments are performed, whose characteristics are summarized in Table 4.2, and explained below:

1. In the first set of experiments, the VIKOR method is employed as described in Sect. 4.3.2, fixing $\gamma = 0.5$ and varying the relative weight w_{SOC} between 0.2 and 0.9 (Table 4.2). Therefore, a total of six selected trade-off solutions are obtained. The density of w_{SOC} values increases for higher values of w_{SOC}, as these values lead to the selections of solutions in the section of the Pareto-front of major interest when searching for eco-efficient trajectories, that is, the section closer to the cost-optimal solution. Additionally, the two solutions located at the Pareto-front extremes are selected, i.e., the cost-optimal and climate-optimal solutions, with the routine mentioned in Sect. 4.3.6. No preliminary knowledge about the expected problem results is needed to conduct these simulations. As a result of this first set of experiments, for each optimized flight we obtain information on eight solutions that determine the shape and extension of the Pareto-fronts relative to individual flights, and the relation between penalties and benefit aggregated over the whole air traffic sample.

2. In the second set of experiments, the effects of selecting a solution leading to a target change in SOC are explored (Sect. 4.3.4). The target values are chosen using the results form the first set of experiments, which obtained average SOC increases up to about +3.0% (see Table 4.3 and Figure 4.6). In light of these results, x_t is varied from 0.5% to 3.0% (Table 4.2), selecting four solutions per flight. Moreover, we set $w_{SOC} = 0.7$ to exemplify the effects of using the option of using VIKOR while setting a target SOC change (Sect. 4.3.5) of +1.0%.

Table 4.2: Overview of the two sets of experiments performed to exemplify the use of the different decision-making methods.

Set	SolFinder strategy	# sel. points	Parameter	Description	Value(s)
1	**VIKOR method for eco-eff.**	6	γ	Group utility weight	0.5
			w_{SOC}	Rel. weight of SOC	0.2, 0.4, 0.6, 0.7, 0.8, 0.9
			w_{ATR}	Rel. weight of $ATR20_{tot}$	$1 - w_{SOC}$
	Pareto-front extremes	2	f_{min}	Minimized objective	$ATR20_{tot}$ or SOC
2	**Target change in f_p**	4	f_p	-	SOC
			x_t	Target change [%]	0.5, 1.0, 2.0, 3.0
	Hybrid VIKOR-target option	1	γ	Group utility weight (VIKOR)	0.5
			w_{SOC}	Rel. weight of SOC (VIKOR)	0.7
			w_{ATR}	Rel. weight of $ATR20_{tot}$ (VIKOR)	$1 - w_{SOC}$
			f_p	objective with limited changes	SOC
			x_t	Limit and target change [%]	1.0

4.4.2 Results

As explained in Sect. 4.3, one of the main advantages of the VIKOR method is that no knowledge of the expected results is needed before solving the problem. For this reason,

the first set of experiments applies the VIKOR method with a range of values of the parameter w_{SOC}. This enables us to perform a preliminary examination of the characteristics of the relation between benefit (in this application, $ATR20_{tot}$ reduction) and penalty (increase in SOC). Relative to this problem, this relation is shown in Figure 4.6, illustrating the change in SOC that is required to achieve a certain reduction in ATR20. The grey curves in Figure 4.6a are obtained aggregating the 100 Pareto-optimal solutions selected using the VIKOR method on each simulation day, varying the relative weight w_{SOC} of the objective function SOC. The coordinates of the points connected by the black line (representing the average relation over the 31 simulated days) can be found in Table 4.3. Setting a low value of w_{SOC} (e.g., w_{SOC} = 0.2), a reduction in $ATR20_{tot}$ of about 13% is obtained, which is almost as large as the maximum potential reduction achieved selecting a climate-optimal routing strategy. Moving along the curve towards the cost-optimal strategy, the magnitude of the $ATR20_{tot}$ reduction decreases. This occurs with a simultaneous decrease of the cost per Kelvin reduction in climate impact, measured by the climate-cost coefficient k [$/K] (Table 4.3). This coefficient is defined as (Matthes et al., 2017):

$$k = \frac{SOC - SOC_{cost\text{-}opt}}{ATR20_{cost\text{-}opt} - ATR20} \tag{4.11}$$

where $ATR20_{cost\text{-}opt}$ and $SOC_{cost\text{-}opt}$ are relative to the cost-optimal solution, while ATR20 and SOC are relative to the considered decision-making strategy. From this first set of experiments, it is possible to understand that: (1) the average $\Delta ATR20_{tot}$ ranges from -3.5 to -14.4%, with an increase in SOC of 0.1-3.0%, respectively; (2) about half of the maximum feasible climate change reduction can be achieved with only +0.5% in SOC.

As previously mentioned, the red and green points highlighted in Figure 4.6a result from summing all the solutions selected for the 100 flights, and averaging over the month of simulation. However, each optimized trajectory is characterised by a different change in $ATR20_{tot}$ and SOC with respect to its corresponding cost-optimal solution. Note here that this cost-optimal solution (shown in red in Figure 4.6a), taken as reference to calculate the relative changes in $ATR20_{tot}$ and SOC, is specific to each route and each simulation day, thus it varies between different flights. The full variability of the relationship between relative changes in $ATR20_{tot}$ and SOC is illustrated in Figure 4.6b. In this panel, one can see that specific solutions can show large deviations from the average values, as some solutions reach an absolute $\Delta ATR20_{tot}$ larger than 60% at penalties lower than 2.5% in terms of ΔSOC. Moreover, Figure 4.6c-f show that the subsets of Pareto-optimal solutions obtained setting different w_{SOC} behave as expected: moving from lower to higher values of w_{SOC} leads to subsets that are confined below lower increases in SOC, while they still stretch towards high $ATR20_{tot}$ reductions (e.g., see the points selected with w_{SOC}=0.8 in Figure 4.6f). The distributions of $\Delta ATR20_{tot}$ and ΔSOC values across the optimized flights are represented in Figure 4.7, which compares the results obtained varying the parameter w_{SOC} applying the VIKOR method, and the climate-optimal scenario. Figure 4.7b shows the percentage of flights characterized by a certain ΔSOC. One can see that, employing VIKOR, the mode of each curve is close to ΔSOC ~ 0%, while the mean and maximum ΔSOC values increase when the weight w_{SOC} decreases. Looking at the $\Delta ATR20_{tot}$ distributions

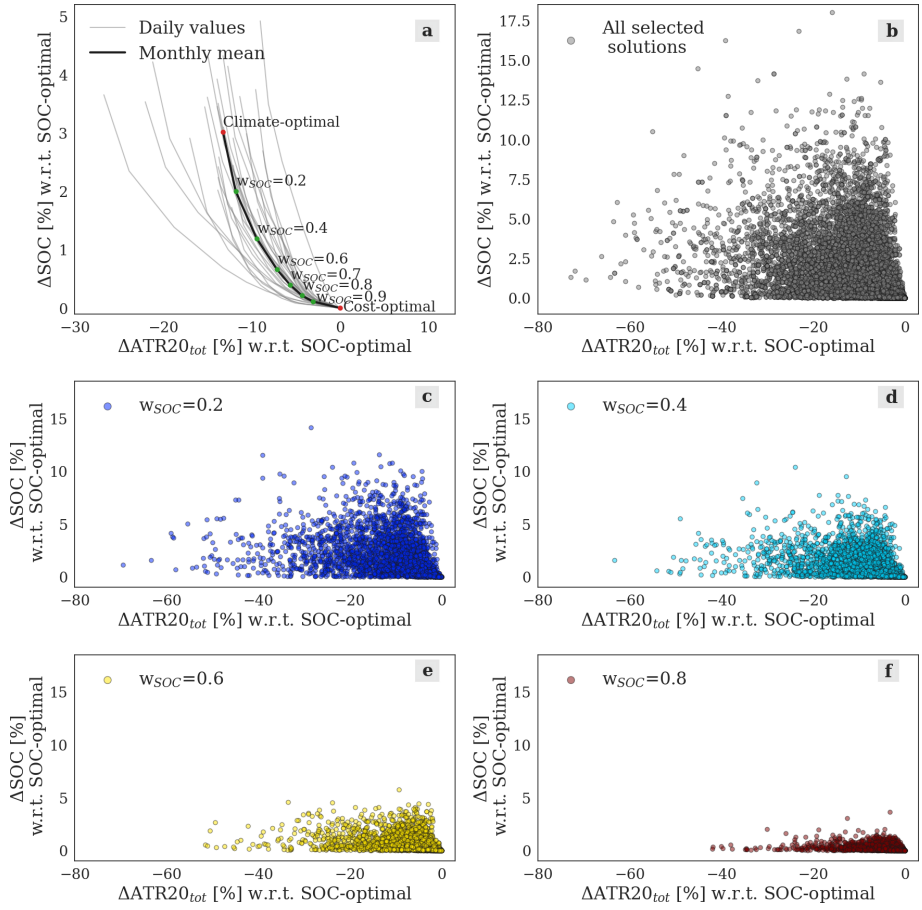


Figure 4.6: Relation between the relative changes in climate impact, $\Delta ATR20_{tot}$ [%], and in simple operating cost, ΔSOC [%], with respect to the cost-optimal solution. *Panel a):* Values obtained summing over the 100 routes optimized per day. The black line illustrates the average values over the 31 days included in the simulations, connecting the points selected varying the VIKOR weight w_{SOC} from 0.2 to 0.9 (green dots). The extremes of the Pareto fronts (climate- and cost-optimal solutions, red dots) are included. The gray lines represent the Pareto fronts obtained on each simulation day. *Panels b)-f):* Scatter graphs of $\Delta ATR20_{tot}$ [%] against ΔSOC [%], representing all the individual selected solutions (4.6b), and subsets of solutions obtained varying the weight of simple operating costs, w_{SOC} (4.6c-4.6f).

in Figure 4.7a, larger differences can be observed also in the modal values for varying w_{SOC}.

The results of the first set of experiments can then be used to conduct the second set, fixing a target or a limit increase in SOC as described in Sect. 4.4.1. The result of this second set of experiments are shown in Table 4.4. To illustrate the difference of employing different decision-making methods, it is useful to compare Figure 4.7 with Figure 4.8. The most evident difference emerges comparing Figure 4.7b with Figure 4.8b. As intended, when a target increase in SOC is set (e.g., +1.0%), most of the selected flights are affected by

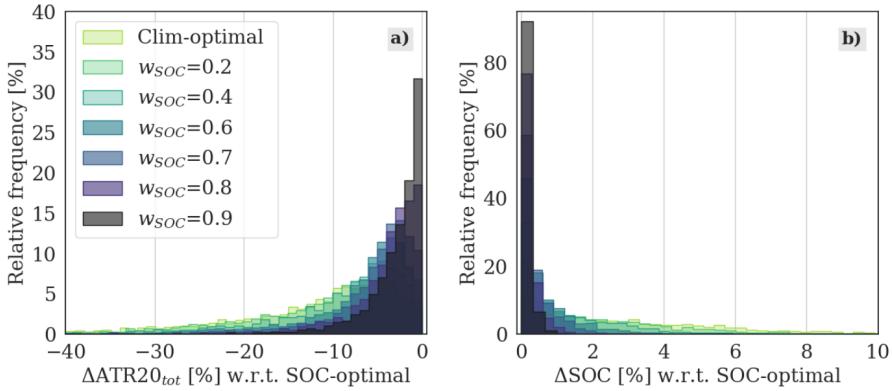


Figure 4.7: Relative frequencies [%] of different values of $\Delta ATR20_{tot}$ [%] (Figure 4.7a), and of ΔSOC [%] (Figure 4.7b) with respect to the cost-optimal solution. The histograms compare the distributions of the values obtained with different decision-making strategies, considering the 100 flights optimized on each simulation day (31*100 values per histogram). The solutions are selected by identifying the minimum climate impact (climate-optimal solutions), or employing the VIKOR method with varying w_{SOC} (first set of experiments).

an increase in SOC equal or similar to the target, thus the curves are centred on this ΔSOC value. However, one can also deduce that some Pareto-fronts do not extend to the target ΔSOC, since values of ΔSOC which are lower than the target are assigned to a fraction of the flights. This results in average ΔSOC values that are lower than the targets, as one can see in Table 4.4. For example, a total increase of 0.8% in SOC is obtained, when the target is set to 1.0%. Moreover, Figure 4.8b shows what distribution of ΔSOC the user can expect employing the hybrid method described in Sect. 4.3.5. The histogram relative to the hybrid option (yellow, hatch-filled) corresponds to the one obtained with VIKOR (with w_{SOC}=0.7), with an additional peak at the determined target SOC increase (1.0%), replacing the larger SOC increases observed in Figure 4.7b. The results illustrated in Figures 4.7b and 4.8b confirm that the strategies available in SolFinder 1.0 are correctly implemented, and lead to the expected selection of Pareto-optimal solutions. Moreover, the possibility of relying on the VIKOR method to identify eco-efficient trajectories is confirmed by Figure 4.9. These curves represent the distributions of the climate-cost coefficient k [$/K], obtained using VIKOR (blue curves) or the target SOC change (red curves). It is possible to observe that lower values of k are obtained using VIKOR, in particular when a relatively high weight is assigned to SOC.

Employing different decision-making strategies, trajectories characterized by different properties are obtained. How these properties vary is shown in Figure 4.10, which compares the mean flight altitudes and flown distances obtained when different decision-making strategies are selected. Firstly, one can notice that cost-optimal flights are characterized by the highest mean flight altitudes and the shortest trajectories among the solutions considered, due to the presence of fuel consumption in the optimization objective. On the opposite situation, the lowest altitude and the longest distances are obtained for climate-optimized flights. This confirms previous studies, which commented that (1) aircraft emissions have lower climate impact at lower altitudes, e.g.,

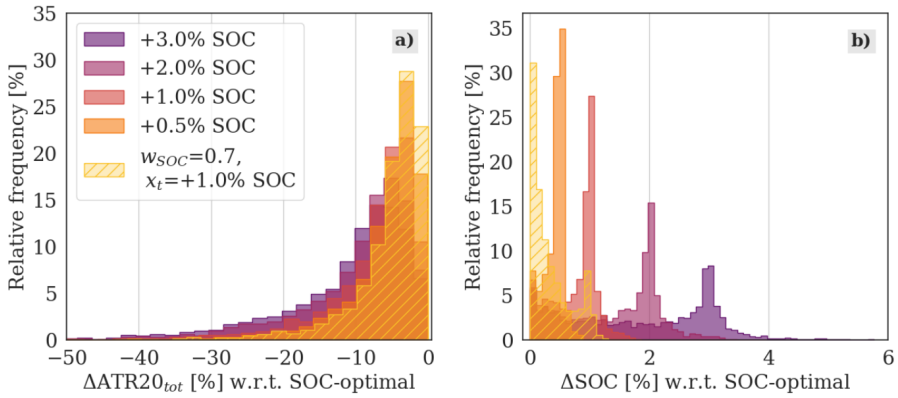


Figure 4.8: Relative frequencies [%] of different values of $\Delta ATR20_{tot}$ [%] (Figure 4.8a), and of ΔSOC [%] (Figure 4.8b) with respect to the cost-optimal solution. The histograms compare the distributions of the values obtained with different decision-making strategies, considering the 100 flights optimized on each simulation day (31*100 values per histogram). The solutions are selected by targeting different SOC changes, or applying the hybrid method with w_{SOC}=0.7 and x_t = 1.0% (second set of experiments).

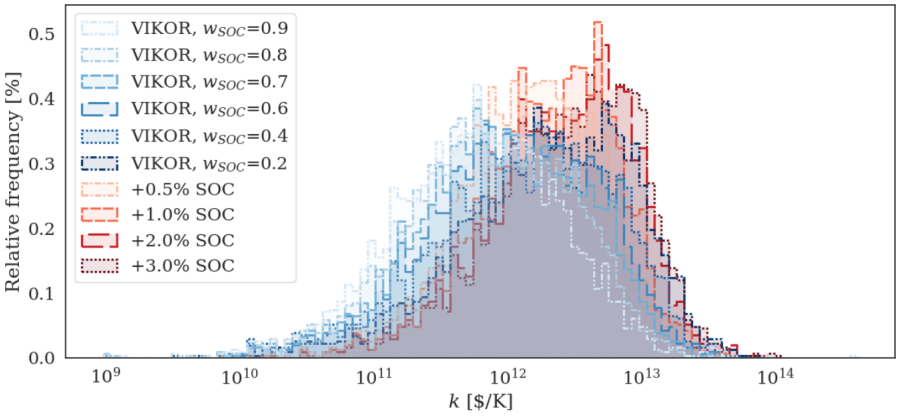


Figure 4.9: Relative frequencies [%] of different values of the climate-cost coefficient k [$/K], comparing the SolFinder solution-picking strategies using VIKOR (blue curves) or the target SOC change (red curves). The curves approximate the histogram outlines (connecting the bars centers) to highlight the shapes of the distributions and facilitate their comparison. Each curve includes the values obtained with different decision-making strategies, considering the 100 flights optimized on each simulation day (31*100 values per histogram).

due to shorter residence time of emitted species (Castino et al., 2021; Matthes et al., 2021; Frömming et al., 2012), and (2) lateral deviations may be necessary to avoid climate sensitive regions (Matthes et al., 2020). Moreover, the variability of the flight properties across the set of simulated flights is larger for climate-optimized flights than for cost-optimal ones. For example, comparing the different variability in flight altitudes, one can see the impact of the lowest aerodynamic drag, which allows minimal fuel use, and is systematically found at higher altitudes. Contrarily, the altitude leading to the

minimal ATR20 is highly variable, due to the high temporal and spatial variability of the atmospheric conditions determining the net flight ATR20. Trade-off solutions between these two extreme scenarios show intermediate properties, with median values and interval bars which gradually evolve moving from one extreme of the curve in Figure 4.6 to the other.

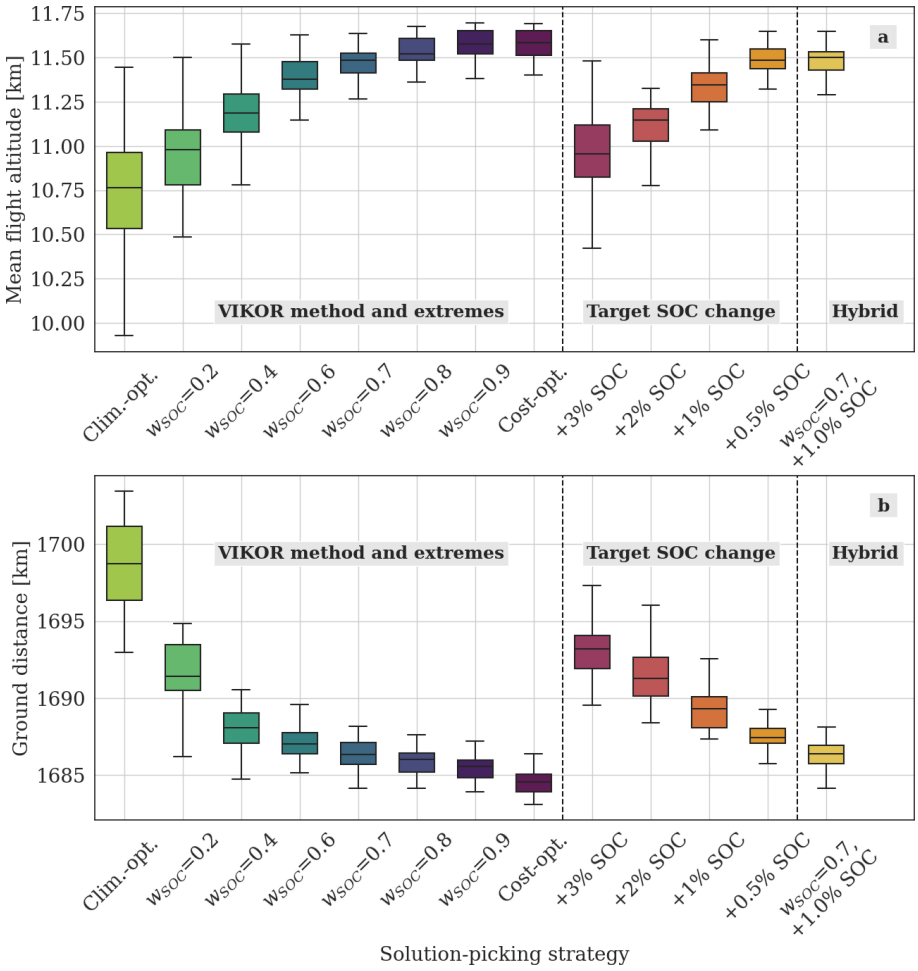


Figure 4.10: Variability of mean flight altitudes [km] (Figure 4.10a) and ground distance [km] (Figure 4.10b) when employing different decision-making strategies. The flight altitudes are calculated averaging over each trajectory, and over the 100 flights optimized on each day. The ground distances represent the total length of each trajectory, averaged over the 100 flights optimized on each simulation day. The boxes extend between 1st and 3rd quartiles over time, and include segments marking the median values. The whiskers indicate the the distribution of the remaining values (excluding eventual outliers).

One can also see that employing the VIKOR method rather than fixing a target increase in costs can lead to different tendencies in the average characteristics of the selected trajectories. For example, comparing the VIKOR method with $w = 0.4$ (causing

ΔSOC ~ +1.2%, see Table 4.3) and setting a target +1.0% change in SOC, one can see that the latter strategy leads to a less frequent selection of lower flight altitudes, while flying longer trajectories, than the former case. Therefore, the user is recommended to identify their preferred decision-making strategy by also considering these secondary aspects, and not exclusively the resulting distributions in objective functions values.

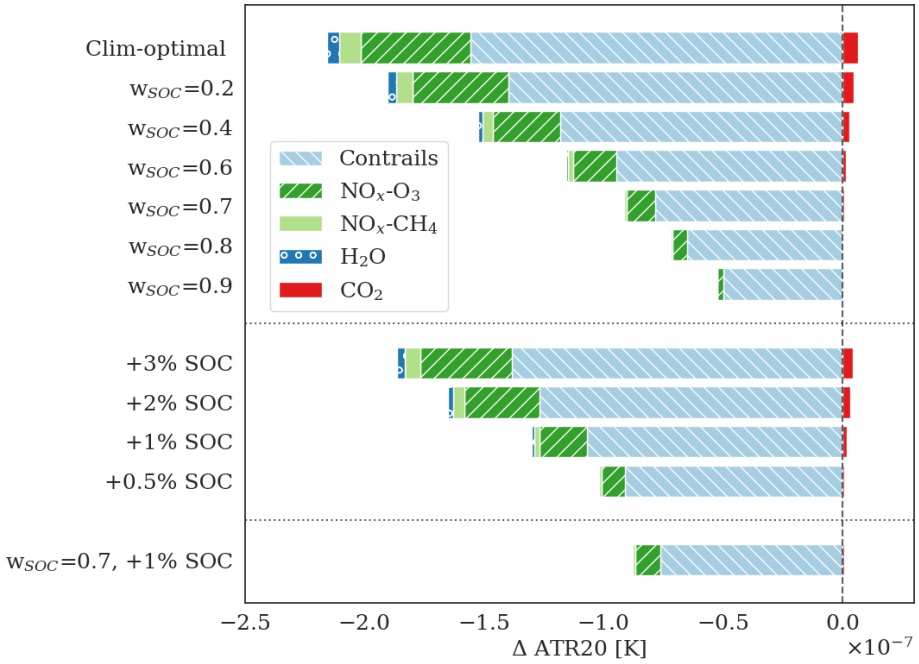


Figure 4.11: Contribution of different climate effects of aviation to the absolute ΔATR20 [K] when employing different decision-making strategies. The horizontal, dotted line distinguish between solutions selected using VIKOR or climate-optimal solutions (upper section), solutions selected targeting a SOC relative change (middle section), and solutions selected applying the hybrid method (lowest bar). The vertical, dashed line separates positive (warming) from negative (cooling) values of ΔATR20.

Lastly, the contribution to the total change in ATR20 of each effect of aviation emissions considered in the optimization process is analyses: CO_2, H_2O, contrails, NO_x via perturbation of ozone, and NO_x via methane depletion. The relative importance of these effects under different decision-making strategies is illustrated in Figure 4.11. Firstly, one can notice that the ATR20 from CO_2 emissions increases moving from cost-optimal to climate-optimal and compromise solutions. This increase is expected, as the climate impact of CO_2 is independent of the background atmospheric conditions at time and location of emission; thus it is simply proportional to the amount of fuel used, which is minimized by cost-optimal flights. On the other hand, the increase in the ATR20 from CO_2 is largely compensated by the reduction in the ATR20 from contrails and, secondarily, from the impact of NO_x on ozone. Moreover, Figure 4.11 shows that reduction in climate impact of contrails becomes increasingly dominant over the reduction of the other effects, when the relative weight w_{SOC} of SOC increases. This

aspect should be considered when selecting the preferred settings of the decision-making strategy. For example, if the decision-maker is interested in reducing both the climate impact of contrails and NO_x-ozone via trajectory optimization, this goal can be achieved allowing larger changes in SOC than those needed to only reduce the ATR20 from contrails effects. The dominant contributions of contrails and, secondarily, of the NO_x climate impact to the ATR20 reduction is confirmed by the results obtained optimizing aircraft trajectories with different tools (Lührs et al., 2021; Simorgh et al., 2022). However, large uncertainties affect the estimates of non-CO_2 effects of aviation (see Sect. 1 and 4), which can heavily affect the relative importance of the different effects of aviation emissions. Therefore, it is relevant to update the modelling chain presented here when enhancements in the scientific understanding and in the ability to model non-CO_2 effects are available, for example, via updated aCCFs versions.

Table 4.3: Properties of the trajectories selected within the 1st set of experiments. The table provides the total monthly percentage changes in climate impact, $\Delta ATR20_{tot}$ [%], in simple operating cost, ΔSOC [%], in fuel used, ΔFuel [%], and in flight time, ΔTime [%], relative to the respective total values from the cost-optimal scenario; and values of the climate-cost coefficient k [$/K]. The minimum and maximum daily values are included within brackets.

SolFinder Strategy	ΔATR20 [%]	ΔSOC [%]	ΔFuel [%]	ΔTime [%]	Coeff. k [$/K]
Climate-optimal	-14.4(-29.2, -6.7)	+3.04(+1.32, +5.00)	+8.14(+2.41,+15.19)	+1.01(+0.59, +1.52)	3.95e+12(1.58e+12, 1.33e+13)
VIKOR w_{SOC}=0.2	-12.8(-26.0, -5.9)	+2.00(+0.72, +3.52)	+5.72(+1.38,+11.18)	+0.51(+0.07, +0.98)	2.94e+12(1.07e+12, 1.05e+13)
VIKOR w_{SOC}=0.4	-10.3(-21.1, -4.7)	+1.19(+0.42, +2.56)	+3.50(+0.70, +8.28)	+0.27(+0.01, +0.57)	2.21e+12(6.05e+11, 9.37e+12)
VIKOR w_{SOC}=0.6	-7.9(-13.8, -4.0)	+0.67(+0.21, +1.52)	+1.86(+0.30, +5.07)	+0.20(-0.01, +0.34)	1.66e+12(4.65e+11, 8.10e+12)
VIKOR w_{SOC}=0.7	-6.2(-11.0, -2.8)	+0.40(+0.14, +0.74)	+1.09(+0.19, +2.61)	+0.12(-0.04, +0.27)	1.27e+12(3.71e+11, 6.54e+12)
VIKOR w_{SOC}=0.8	-4.9(-8.7, -1.3)	+0.22(+0.09, +0.34)	+0.55(+0.05, +1.30)	+0.08(-0.09, +0.22)	8.81e+11(2.37e+11, 4.31e+12)
VIKOR w_{SOC}=0.9	-3.5(-6.3, -0.5)	+0.11(+0.06, +0.18)	+0.25(-0.00, +0.46)	+0.06(-0.05, +0.16)	6.46e+11(1.80e+11, 2.85e+12)

Table 4.4: Properties of the trajectories selected within the 2nd set of experiments. The table provides the total monthly percentage changes in climate impact, ΔATR20 [%], in simple operating cost, ΔSOC [%], in fuel used, ΔFuel [%], and in flight time, ΔTime [%], relative to the respective total values of the cost-optimal scenario; and values of the climate-cost coefficient k [$/K]. The minimum and maximum daily values are included within brackets.

SolFinder Strategy	ΔATR20 [%]	ΔSOC [%]	ΔFuel [%]	ΔTime [%]	Coeff. k [$/K]
+3.0% SOC	-12.5(-25.2, -6.3)	+1.92(+1.00, +2.82)	+5.47(+1.79, +9.55)	+0.51(-0.05, +0.91)	2.90e+12(1.22e+12, 9.67e+12)
+2.0% SOC	-11.1(-21.5, -5.7)	+1.43(+0.82, +1.96)	+4.04(+1.34, +6.94)	+0.39(-0.11, +0.72)	2.44e+12(9.40e+11, 8.45e+12)
+1.0% SOC	-8.7(-14.9, -3.4)	+0.80(+0.59, +0.98)	+2.14(+0.82, +3.59)	+0.26(-0.13, +0.52)	1.79e+12(6.72e+11, 7.08e+12)
+0.5% SOC	-6.9(-12.8, -2.0)	+0.42(+0.36, +0.50)	+1.02(+0.39, +1.90)	+0.19(-0.06, +0.36)	1.27e+12(3.89e+11, 6.13e+12)
VIKOR w=0.7, +1.0% SOC	-6.0(-10.7, -2.4)	+0.35(+0.14, +0.61)	+0.94(+0.19, +2.21)	+0.11(-0.05, +0.24)	1.18e+12(3.52e+11, 6.38e+12)

4.5 Discussion

This Chapter illustrated the decision-making strategies implemented in the SolFinder 1.0 module, and how they can be used to identify eco-efficient trajectories. The climate-optimization of aircraft trajectories has been increasingly researched in the last decade, as efforts to reduce the climate impact of aviation lead to the investigation of operational mitigation strategies. For example, Grewe et al. (2017b) optimized a set of transatlantic flights during eight representative weather patterns in winter and summer, employing the air traffic simulator SAAM and the Climate Change Functions (CCFs). Grewe et al., 2017 found that a 10% reduction in climate impact can be achieved with a 1.0% increase in operating costs (Grewe et al., 2017b). In this study, a different region of the airspace (European flights) was considered, and a larger number of weather patterns (every day in the month of January 2018) was included, although limited to the winter season and to night-time; nevertheless, the results in Grewe et al. (2017b) were found to be aligned with those presented in Sect. 4.4, since a ΔSOC ~ +1.2% corresponds to a ΔATR20 ~ −10.3% (Table 4.3). The maximum feasible climate impact reduction is higher (about 20%) in Grewe et al. (2017b), but this is achieved with an approximately double increase in costs. The discrepancy in the section of the Pareto-front closer to the climate-optimal solution may be due to the different temporal and spatial domains. The mitigation potential of optimized aircraft trajectories is expected to be affected by seasonal and daily variability (e.g., Reutter et al., 2020, and Castino et al., 2021), thus the methodology presented in this Chapter can be extended to cover multiple years, to investigate this aspect. Under specific weather conditions, cost-benefit relations were found to show higher eco-efficiency than were found aggregating the model output over all the routes, and all the simulated days. For example, Lührs et al. (2021) analysed a day characterised by a weather situation with strong contrail formation, and found that a 0.75% increase in fuel used halved the climate impact. The results in Lührs et al. (2021) confirm the possibility of identifying weather situations that allow for a higher eco-efficiency than others. The modelling chain presented in this Chapter enables us to optimize aircraft trajectories under a large number of different atmospheric conditions, within a feasible computational time. Therefore, on-going research is using the newly developed version of AirTraf, coupled with the SolFinder module, to analyse under which weather conditions eco-efficient aircraft trajectories are most likely to be identified. To this end, additional decision-making strategies are being investigated, to exploit the ability of VIKOR to identify lower values of the climate-cost coefficient k than a strategy applying a target increase in SOC to all flights (Figure 4.9). Two candidate additional strategies are illustrated in Figure 4.12. With these options, only a fraction of the flights identified by VIKOR is climate-optimized, due to an additional condition. This is obtained setting a threshold value of the coefficient k, in order to climate-optimize only the top ranked half of the flights (Figure 4.12a) or until a certain budget is spent (e.g, +0.5% of SOC in Figure 4.12b). A disadvantage of these decision-making strategies is that their settings configuration relies on information on the whole system of optimized flights, which is not available considering the Pareto front resulting from a single-flight optimization. Therefore, preliminary simulations have to be run to derive some parameter values, for example the specific threshold value of the climate-cost coefficient k [$/K]. Because of the large variability of k, these decision-making strategies are more

reliant on the results obtained from previous simulations than the strategies included in SolFinder 1.0.

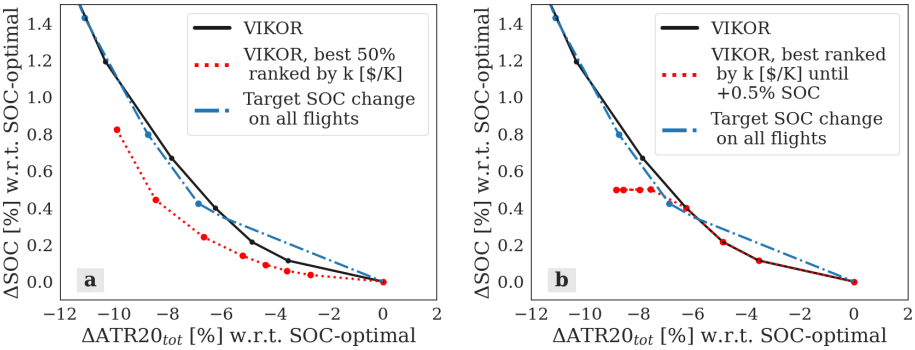


Figure 4.12: Relation between the percentage changes in climate impact, ΔATR20 [%], and in simple operating cost, ΔSOC [%], with respect to the cost-optimal solution. The values are obtained aggregating the properties of all the optimized flights (31 days, 100 routes optimized per day). The black curve connects the points obtained with the SolFinder strategy relying on VIKOR, while the blue line and points refer to the SolFinder strategy targeting a fixed SOC change. The red lines refer to additional strategies considered for future versions of SolFinder: optimization of the 50% of the flights best ranked by k (Figure 4.12a), and optimization of the flights best ranked by k until an increase in SOC of 0.5% is achieved.

The present work estimates the climate effect of aviation resulting from the emission of CO_2, H_2O, NO_x, and from the formation of contrail-cirrus. Estimating the radiative forcing caused by non-CO_2 effects is a complex process, leading to results that are affected by large uncertainties due to, for example, incomplete scientific understanding and modeling capabilities (Lee et al., 2021). As described in Sect. 4.4.1, the aCCFs version 1.0A is used to estimate the climate impact of aviation (Matthes et al., 2023), which are calibrated towards the results of a climate response model (AirClim, Dahlmann et al., 2016) to align the relative importance of individual aCCFs. This is an update of the consistent set of aCCF 1.0 (Yin et al., 2023), calculating the climate impact of CO_2, H_2O, NO_x-ozone, NO_x-methane and contrails in terms of ATR20, assuming pulse emissions (P-ATR20). This prototype set of functions are the focus of on-going research, to address their sources of uncertainties. Moreover, factors are used to: (1) convert the aCCFs values to a different climate metric, F-ATR20, which assumes a business-as-usual future emission scenario; (2) include the efficacy of each climate impact effect (Dietmüller et al., 2023). These assumptions introduce additional sources of uncertainties. Moreover, the majority of ice-supersaturated regions (supporting persistent contrail formation) have characteristic dimensions that are smaller than the horizontal resolution of the model employed in this study. To take this factor into account, a parameterization developed by Burkhardt et al. (2008) is employed to estimate the fraction of model grid box which is supporting persistent contrails. The potential of reducing the flights climate impact by contrail avoidance could be reduced by factors not included in this research. For example, here weather conditions simulated by an atmospheric model (EMAC) are used rather than weather forecast. In real life applications, this mitigation strategy relies on the accuracy and stability of weather forecast, as discussed in Sect. 1. Lastly, note that a

simplified representation of the operating cost is used, to limit the computational time required for their evaluation within each optimization step. To this end, a linear relationship between cost of time and flight time is assumed (see Eq. (4.1) and Yamashita et al., 2020). Therefore, additional costs caused by delays are neglected. Further research will explore the impact of optimizing not only the location of the flight trajectory (see Sect. 4.2), but also the airspeed, improving fuel efficiency compared to the present study, which assumes a constant Mach number for all solutions. Other studies found that speed changes can be important for reducing fuel flow, NO_x emissions and, ultimately, NO_x climate effects (Simorgh et al., 2023). This improvement of AirTraf is expected to impact the SolFinder results, by reducing the penalties in terms of operating costs and CO_2 emissions for a certain gain in terms of reduction of ATR20. On the other hand, including the airspace structure and capacity, which are neglected in this study, can reduce the estimated climate impact mitigation potential of this operational strategy.

4.6 Summary

In this Chapter, the decision-making strategies implemented in the SolFinder 1.0 module are described. The SolFinder 1.0 module has been coupled to the AirTraf 3.0 submodel, as part of its development to efficiently solve multi-objective optimization problems. It was showed here how the selected decision-making strategies can be used to identify solutions matching specific preferences (e.g., eco-efficient aircraft trajectories). Moreover, using this modelling chain, it is possible to explore the results variability under a large number of consecutive days, due to the coupling between SolFinder and an atmospheric chemistry model (EMAC), via the EMAC submodel AirTraf. To demonstrate the usage of the tool, this Chapter showed results for the period of one winter month (1-31 January 2018). A bi-objective optimization problem was solved, minimizing the climate impact of the aircraft trajectory (F-$ATR20_{tot}$) and its simple operating costs (SOC), and the solutions selected by different configurations of SolFinder 1.0 were analysed. Comparing the strategies using VIKOR and a target change in SOC, lower values of the climate-cost coefficient k [\$/K] (i.e., a higher eco-efficiency) are obtained with the former option. The modelling chain presented in this Chapter has been used to identify those weather situations allowing for the largest benefits via the optimization of aircraft trajectories, by avoiding contrail formation (Chapter 5) or by minimizing the temperature response caused by the impact of NO_x emissions (Chapter 6).

5

Mitigation potential of contrail avoidance and its dependency on weather patterns

The formation of persistent condensation trails (contrails) behind aircraft is expected to cause significant warming effects on the climate. Aircraft trajectory optimization has been suggested as a measure to reduce persistent contrail formation and, therefore, aviation climate impact (Chapter 2). However, contrail avoidance relies on the availability of ice-supersaturation forecasts, which are affected by large uncertainties. Moreover, contrail avoidance likely leads to extra fuel consumption, resulting in higher CO_2 emissions and operating costs. The present study focuses on the dependency of contrail avoidance on meteorological variability, considering trajectory optimization strategies that reduce contrail formation with limited changes in fuel use. A sample of 100 North Atlantic flights is optimized every day between 1 December 2015 and 31 December 2018 using the ECHAM/MESSy Atmospheric Chemistry (EMAC) model and its submodels AirTraf and CONTRAIL (Chapters 3 and 4). A well-established weather pattern classification based on the North Atlantic Oscillation (NAO) and East Atlantic (EA) patterns is applied to distinguish winter days into five classes. Weather conditions linked to a weak and tilted jet stream results in the highest ratio between benefit (contrail reduction) and penalties (extra fuel burnt). As air pressure and wind fields forecasts guarantee a better performance than those of relative humidity, conditions linked to high mitigation potential from contrail avoidance may be identified in advance by air traffic management using these insights.

5.1 Introduction

Exhaust plumes from jet engines enter the atmosphere at a temperature and moisture that are much higher than the ambient conditions at cruise level. During mixing

This Chapter is based on the results presented in *Castino, F., Grewe, V., Yamashita, H., Hildebrandt, K.G., Yin, F.: Seasonal variability and weather pattern dependency of contrail avoidance in the North Atlantic, under review.*

between the warm exhaust plume and cold ambient air, the local relative humidity increases and may reach saturation with respect to liquid water (Schumann, 1996). Consequently, condensation trails (contrails) are occasionally visible as ice clouds behind the aircraft (Chapter 2). In the first few minutes after their formation, contrails are clearly identifiable by their linear shape. However, the contrail's life-time can extend to several hours, if it forms or is transported into ice-supersaturated regions (ISSRs) of the atmosphere (Gierens et al., 2017). In such cases, contrails may lose their original shape, and become difficult, or even impossible, to distinguish from natural cirrus (Heymsfield et al., 2010). Similarly to natural clouds, these anthropogenic cirrus interact with radiation emitted by the Sun (incoming) and the planet's surface (outgoing), resulting in cooling and/or warming effects (Kärcher, 2018). Because of the complex interaction between radiation and cloud particles, the net radiative forcing of a contrail is highly dependent on the time, geographic location, and altitude at which the aircraft emission occur, as well as on the characteristics of the aircraft itself (Frömming et al., 2021; Engberg et al., 2025). Considering historical emissions (1940–2018) from global aviation, Lee et al. (2021) reported an estimated effective radiative forcing (ERF) of contrail cirrus of 57.4 mWm^{-2} in 2018, although with a wide 90% likelihood range (17 – 98 mWm^{-2}). Comparing with the well-known impact of CO_2 emissions, both the best estimate (34.3 mWm^{-2}) and the uncertainty range (28 – 40 mWm^{-2}) of the ERF from CO_2 are smaller than those reported for contrail cirrus. Despite low confidence levels, contrail cirrus are thus expected to be responsible for a large warming effect on the climate. Consequently, reducing contrail formation has been suggested as a strategy to mitigate the climate impact of aviation (Chapter 2). However, several challenges hinder the implementation of contrail avoidance in air traffic management, including the ability to forecast ice-supersaturated regions (Gierens et al., 2020; Lee et al., 2023). Since relative humidity is characterized by strong temporal and spatial gradients, simulating this field via numerical weather prediction models is difficult, thus previous studies suggested to include dynamical fields as proxies to facilitate the forecast of ISSRs (Wilhelm et al., 2022; Hofer et al., 2024). Therefore, insights on which weather conditions support ice-supersaturation would contribute to overcome this challenge.

Because of the temporal and spatial variability of ISSRs, the mitigation potential of contrail avoidance is expected to vary under different meteorological situations. Previous studies investigated how the potential of reducing persistent contrails changes throughout the year, looking at monthly variabilities (Yin et al., 2018a; Roosenbrand et al., 2023). Grewe et al. (2017b) and Yamashita et al. (2021) explored the variability of the climate impact mitigation potential from aircraft trajectory optimization, analysing an air traffic sample over the North Atlantic; however, only a small number of representative days (five winter days, three summer days) was considered. The present study builds on the work presented by Yamashita et al. (2021), which showcased the use of the EMAC submodel AirTraf 2.0 to optimize aircraft trajectories with respect to several optimization objectives, including fuel consumption and contrail distance. Due to the limited number of days analysed in their work, the dependency of contrail avoidance on the natural atmospheric variability is not fully captured by Yamashita et al. (2021). Moreover, this previous study recommended to further develop the modelling chain in order to solve multi-objective optimization problems, thus identifying trade-off solutions

leading to larger environmental benefit per extra unit of fuel burnt. This Chapter addresses these research gaps. In fact, the analysis is extended to 37 full months (from 1 December 2015 to 31 December 2018), and a new AirTraf version is used, including the SolFinder decision-making module (Chapter 4), to compare various optimization strategies between the extreme options, minimizing fuel and contrail distance.

Therefore, the objective of this Chapter is to explore how different atmospheric conditions affect the properties of contrail-avoiding aircraft trajectories, considering both seasonal and daily variabilities. This knowledge would support air traffic management in anticipating on which days contrail avoidance is particularly beneficial. The daily variability during winter is explored in more detail by classifying winter days into five weather types, clustering days that typically present similar strengths and locations of the jet stream (Irvine et al., 2013). Different trajectory optimization strategies are compared:

- a reference scenario, selecting aircraft trajectories that minimize fuel consumption;
- three alternative options, optimizing trajectories with respect to both fuel and *contrail distance*, which is defined as the distance flown through regions of the atmosphere supporting the formation of persistent contrails;
- an extreme scenario, minimizing contrail distance.

The trajectory optimization is performed by the air traffic simulator AirTraf, using the atmospheric conditions provided by the EMAC model (Chapter 3). The main characteristics of these models are provided in Section 5.2. This section also includes the particular settings employed to run the simulations analysed in this study (Section 5.2.2), and the classification strategy applied to distinguish winter days into five types (Section 5.2.3). Subsequently, the seasonal (Section 5.3.1) and daily variability (Section 5.3.2) is examined. These results are discussed and summarized in Sections 5.4 and 5.5.

5.2 Methods

5.2.1 Model overview

The ECHAM/MESSy Atmospheric Chemistry (EMAC) model is a numerical chemistry and climate simulation system that includes sub-models describing tropospheric and middle atmosphere processes and their interaction with oceans, land and human influences (Jöckel et al., 2010). The core atmospheric model ECHAM5 (5th generation European Centre Hamburg general circulation model, Roeckner et al., 2006) is coupled with several submodels via the interface provided by MESSy2 (second version of the Modular Earth Submodel System[1]). Each submodel describes a specific element of the climate system, and can be activated or deactivated depending on the simulation setup. In this study, the submodels CONTRAIL and AirTraf play a crucial role, thus they have been extensively described in Chapter 3 (Section 3.2 and 3.3). The CONTRAIL submodel (Frömming et al., 2014) computes the potential contrail cirrus coverage, i.e., the fraction

[1]Further information is available at the MESSy Consortium Website: http://www.messy-interface.org (last access on 15 May 2025).

of the model grid-box where persistent contrails can be found, according to the parameterization presented by Burkhardt et al. (2008). The potential contrail cirrus coverage at each time and location is delivered to the air traffic simulator AirTraf, which identifies optimal aircraft trajectories using an Adaptive Range Multi-Objective Genetic Algorithm (ARMOGA, Sasaki et al., 2005; Yamashita et al., 2016; Yamashita et al., 2020). AirTraf can solve single- or multi-objective optimization problems, aiming at minimizing one or more of the available objectives (such as flight time, operating costs, and climate impact). When a multi-objective optimization problem is solved and the optimization objectives are conflicting, more than one optimal solution (i.e., a set of Pareto-optimal solutions) is found by the genetic algorithm. Therefore, a decision-making module, SolFinder, is included in AirTraf to ensure that a single optimal trajectory is selected, according to one of the implemented strategies (Chapter 4). The chosen modelling chain offers the advantage of exploring the variability of optimized aircraft trajectories over a large number of weather situations. Since AirTraf operates online during the simulation, the aircraft trajectories optimization is based on the weather conditions simulated at the model time step corresponding to the departure time of the flight. Therefore, weather data with a high time resolution (minutes) over long periods of time (years) is efficiently used as input for the optimization.

5.2.2 Simulations setup

This section and Table 5.1 summarize the setup of the experiments conducted in this study. The EMAC model is employed in the T42L31ECMWF resolution, which corresponds to a horizontal resolution of approximately 2.8° × 2.8° in longitude and latitude (~300 km at mid latitudes), and 31 vertical levels. The vertical resolution is about 30 hPa at 400-100 hPa, i.e., at typical flight levels.

The time resolution of the simulation is 12 minutes, and the overall duration of the simulation extends from 1 December 2015 to 31 December 2018. To ensure that the weather conditions are aligned to those actually occurred during this period, the ERA5 dataset (Hersbach et al., 2020) is used for initialization and nudging of selected atmospheric variables.

On each simulation day, the AirTraf submodel optimizes an air traffic sample including 100 North Atlantic flights. Figure 5.1a illustrates the geographic region covered by the air traffic sample. The flights are a subset of the transatlantic traffic sample in 2019 from Saez Ortuno (2022), which was obtained originally from FlightRadar24. The selection of the city pairs aimed at obtaining a good geographical coverage over the North Atlantic region, so that a good representation of the weather situation is achieved. Considering this criterium, 100 city pairs were selected based on the travelled distance (i.e., the longest) and the frequency (most frequent) within the initial dataset. Subsequently, the most frequent departure times was identified for each city pair, resulting in the distribution visualised in Figure 5.1b. It is evident that two clusters of departure times can be identified, depending on their direction (eastward versus westward). The aircraft properties and performance are simulated taking reference values provided by BADA relatively to the A330-301 model (Eurocontrol, 2011). The properties are evaluated at 100 flight segments (n_{wp} = 101), as set in the benchmark tests presented in Yamashita et al. (2016).

For each individual aircraft trajectory, AirTraf solves a bi-objective optimization

Table 5.1: Main settings of ECHAM5, AirTraf, and SolFinder.

	ECHAM5
Horizontal resolution	T42 (~ 2.8° × 2.8° in longitude and latitude)
Vertical resolution	L31ECMWF (31 vertical pressure levels up to 10 hPa ~ 30 km)
Time step	12 min
Duration	1 Dec. 2015 - 31 Dec. 2018 (each day, 37 months)
Reanalysis data (for initialization and nudging)	ERA5
	AirTraf
Trajectory waypoints	101
Aircraft	A330-301
Air Traffic Sample	100 routes over the North Atlantic, selected based on length and frequency in 2019*
Departure times	Distributed throughout the day, selected based on frequency in 2019*
Optimization strategy	Multi-objective optimization of: (1) fuel consumption, (2) contrail distance

*Data available from FlightRadar24 dataset and Saez Ortuno (2022).

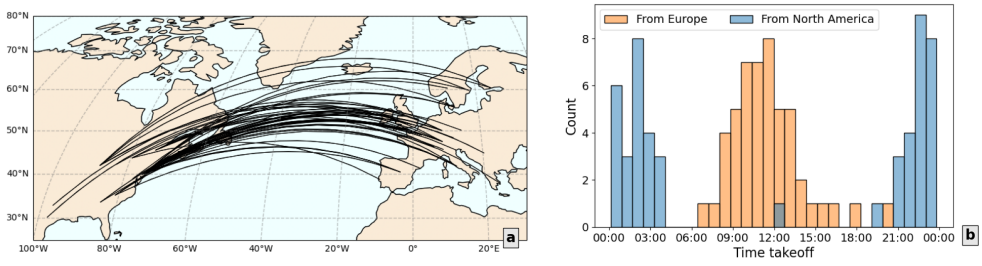


Figure 5.1: Characteristics of the air traffic sample employed in this study. Panel a: Location of the 100 selected city pairs, connected by great circle. Note that less than 100 lines are plotted, as most city pairs are connected in both eastward and westward directions. Panel b: Number of flights departing at various take off time throughout the day.

problem, having as objective the minimization of fuel consumption, f_{fuel}, and contrail distance, f_{cont}. The fuel consumption is calculated via the aircraft performance model of Eurocontrol's Base of Aircraft Data (BADA Revision 3.9, Eurocontrol, 2011). The contrail distance is calculated by multiplying the potential contrail cirrus coverage at each flight segment with the length of the trajectory at the same segment. Below, the mathematical description of these two objective functions is provided (Yamashita et al., 2020):

$$f_{\text{fuel}} = \sum_{i=1}^{n_{wp}-1} \text{FUEL}_i \qquad \text{[kg(fuel)]} \tag{5.1}$$

$$f_{\text{cont}} = \sum_{i=1}^{n_{wp}-1} \text{potcov}_i d_i \qquad \text{[km(contrail)]} \tag{5.2}$$

where FUEL_i [kg], potcov_i [-], and d_i [km] are the fuel consumption, contrail potential coverage, and flown distance over a flight segment i, respectively.

If contrails are formed along a *fuel-optimal* trajectory, the aircraft can be deviated to reduce the contrail distance, depending on the meteorological condition and the optimization constraints. If this mitigation potential exists, a trade-off between contrail distance and fuel consumption is expected, thus a set of Pareto optimal solutions is identified by AirTraf for the individual flight. Therefore, the SolFinder module intervenes to select an individual solution among the Pareto set. In the current study, five points are selected along each Pareto front (see Table 5.2):

5

- two extreme points, identified as *fuel-optimal* and *contrail-optimal*;
- three trade-off points, selected using the VIKOR method varying the relative weights of the optimization objectives w_{fuel} and w_{cont}. These points are identified as *trade-off/low-fuel*, *trade-off/mid-fuel*, and *trade-off/high-fuel*; the names suggest that increasing penalties in terms of extra fuel consumption are allowed moving from the first to the last point.

Table 5.2: SolFinder selection strategies.

Name of solution	**Selection strategy**
Fuel-optimal	Extreme point, minimizing fuel use
Trade-off/low-fuel	VIKOR method ($w_{\text{fuel}} = 0.75$, $w_{\text{cont}} = 0.25$, $\gamma = 0.5$)
Trade-off/mid fuel	VIKOR method, ($w_{\text{fuel}} = w_{\text{cont}} = 0.5$, $\gamma = 0.5$)
Trade-off/high fuel	VIKOR method, ($w_{\text{fuel}} = 0.25$, $w_{\text{cont}} = 0.75$, $\gamma = 0.5$)
Contrail-optimal	Extreme point, minimizing contrail distance

5.2.3 Weather pattern classification

To distinguish between days characterized by different weather patterns, the classification method developed by Irvine et al. (2013) is applied. This classification is based on the similarity between the weather pattern occurring on a specific day, and the North Atlantic Oscillation (NAO) and East Atlantic (EA) patterns (Wallace et al., 1981; Barnston et al., 1987; Hurrell et al., 2003). The NAO and EA patterns are recurrent north-south dipoles of pressure anomalies over the North Atlantic, both characterized by a positive and negative phase. To measure the similarity with the NAO and EA patterns,

the daily mean geopotential height at 250 hPa is compared to climatological fields from a ten-year EMAC simulation, from which the seasonal cycle is extracted by Fouried filtering (Irvine et al., 2013; Yamashita et al., 2021). Therefore, daily anomalies of geopotential height at 250 hPa are obtained. Subsequently, the inner product between the daily anomalies and the NAO pattern is calculated, to derive daily NAO coefficients. The same step is performed to compare the daily anomalies with the EA pattern. Once the NAO and EA coefficients for each simulation day are available, the threshold values identified by Irvine et al. (2013) are applied to group the days into different weather classes (see Table 5.3)[2].

Table 5.3: For each weather pattern type, the table indicates the classification criteria and the resulting typical jet stream strength/location. More details are provided by Irvine et al. (2013).

Winter weather type	NAO coeff.	EA coeff.	Jet stream
W1	$\lvert c_{NAO}\rvert \leq 1$	$c_{EA} > 0.4$	strong/zonal
W2	$c_{NAO} > 0.4$	$\lvert c_{EA}\rvert \leq 0.4$	strong/tilted
W3	$\lvert c_{NAO}\rvert \leq 1$	$c_{EA} < -0.4$	weak/tilted
W4	$c_{NAO} < -0.4$	$\lvert c_{EA}\rvert \leq 0.4$	strong/confined
W5	$\lvert c_{NAO}\rvert \leq 0.4$	$\lvert c_{EA}\rvert \leq 0.4$	weak/confined

This classification presents several advantages. First of all, this method was developed to represent classes that lead to different routing options, and hence it concentrates on the geopotential height anomalies at 250 hPa, which determine the wind field at cruise levels. Secondly, the variability in strength and location of the jet stream over the North Atlantic is well represented by this classification method. As a consequence, we can expect similar properties of aircraft trajectories optimized under the atmospheric conditions observed on different days, but labelled as the same weather pattern class.

The resulting average conditions for each weather pattern are illustrated in Figure 5.2. Figure 5.2 shows the average geopotential height anomalies at 250 hPa [gpm] over all days labelled as a particular weather pattern class. Moreover, this figure indicates the average location and strength of the jet stream. For example, the second class (W2) collects weather conditions close to the positive NAO phase. This corresponds to lower-than-average pressure over Greenland and Iceland, and opposite anomalies over western Europe (Figure 5.2b). This strong pressure gradient determines the location of the jet stream, which is on average more intense under such weather conditions. During the negative NAO phase (similar to W4, Figure 5.2d), the pressure gradient between these two regions of the Atlantic decreases, thus the jet stream weakens. For the EA pattern, the dipole is shifted southward. In its positive phase, the area of low pressure anomalies extends over the North Atlantic from the western coast of Ireland (as showed in Figure 5.2c). Figure 5.2 compares very well with the patterns showed by previous studies that applied the same classification method (Irvine et al., 2013; Yamashita et al., 2021), even though these studies used different sources for the atmospheric fields (ERA-Interim, and EMAC nudged towards ERA-Interim, respectively). This agreement in the resulting patterns of average geopotential height anomalies at 250 hPa, as well as in

[2]The python implementation of this classification method is available at https://doi.org/10.4121/d5413c6f-4e15-4d44-b385-809c6d77d248.

the average location of the jet stream, demonstrates that the days are correctly distinguished into the five winter classes.

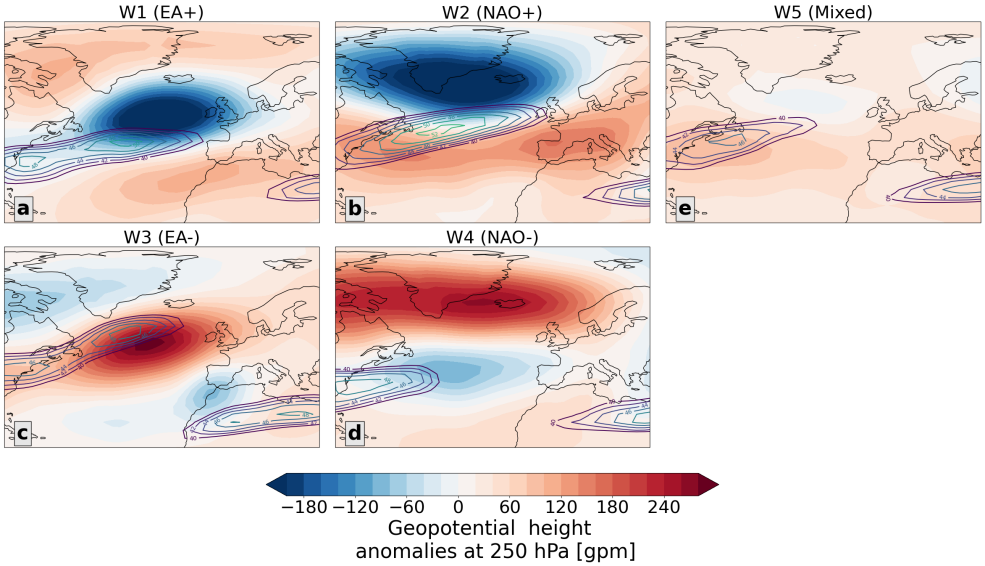


Figure 5.2: Average geopotential height anomalies at 250 hPa [gpm] under the five patterns used to classify weather conditions. The contour lines represent average horizontal wind velocities above $40 ms^{-1}$, to illustrate the jet stream location and strength.

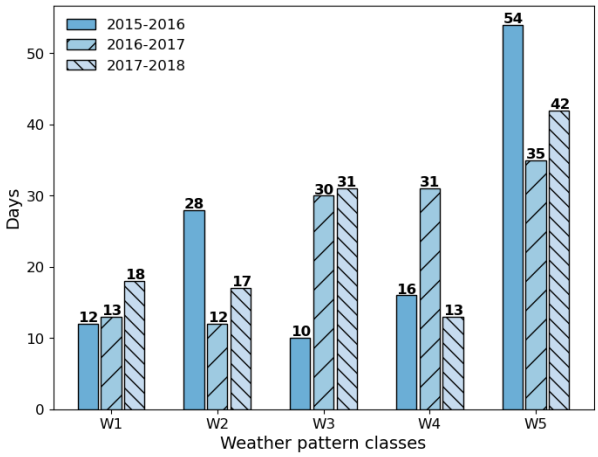


Figure 5.3: Occurrence frequency of each winter weather pattern class, comparing the three extended winter seasons (December, January, February, and March of 2015-2016, 2016-2017, and 2017-2018) considered in the present study.

Figure 5.3 illustrates the number of days per weather pattern class which are

analysed in this study. As described in Section 5.2.2, the simulations cover the period from 1 December 2015 to 31 December 2018. Therefore, three full winters (December, January, February, and March, DJFM) are available for analysis. The winter season is extended to March, as this is typically done in previous studies focusing on the NAO pattern (Smith et al., 2020; Dong et al., 2025), and because of the strength and location of jet stream, which reaches in March its minimum mean latitude (Woollings et al., 2014), hence it is highly influential over the North Atlantic Flight Corridor. The key results do not change restricting the analysis to the meteorological winter (DJF, see Appendix B) but they are based on fewer days, particularly within the W1 class (Figure B.3). Looking at Figure 5.3, one can see that the frequency of each weather pattern class varies on different years. For example, W2 reached a peak of 32 days in the winter of 2015-2016, while it only occurred on 12 days in the following winter season.

5.3 Results

5.3.1 Seasonality of contrail avoidance

In this section, we consider the entire simulated period (from 1 December 2015 to 31 December 2018) to investigate the seasonal variability of the properties of aircraft trajectories obtained from different optimization strategies. Figure 5.4 compares trajectories minimizing fuel consumption (red, solid lines), contrail distance (blue, dotted lines), and those solutions that represent a compromise between these two extremes, with a higher relative importance in limiting fuel penalties (orange, dashed lines). Therefore, these curves represent three solutions described in Section 5.2.2: *fuel-optimal*, *contrail-optimal*, and *trade-off/low-fuel*, respectively. The top panel, Figure 5.4a, illustrates the evolution of contrail distance per flown distance, i.e. the fraction of the total flown distance travelled through regions of the atmosphere supporting persistent contrails. The curve indicates the median value, while the shaded areas represents the variability over the 100 flights included in the air traffic sample (extending from the first to the third quartile). A running average with a window of 30 days is applied to the time series.

First of all, one can see that contrail distance varies significantly with different trajectory optimization strategies, as there is almost no overlap of the shaded areas of different curves (representing the variability over the air traffic sample). As expected, the contrail distance reaches a maximum and a minimum at the extreme cases (*fuel-optimal* and *contrail-optimal*, respectively). *Fuel-optimal* trajectories reach the highest peaks in contrail distance per flown distance in Spring 2017, Autumn 2017, and Summer 2018. *Contrail-optimal* flights achieve a minimal contrail formation in summer, when we also observe the lowest variability over time. Contrarily, on average, *fuel-optimal* trajectories are characterised by smaller contrail distances during winter.

To understand these trends, we consider the mean flight altitudes along the aircraft trajectories (Figure 5.4b). Similarly to panel 5.4a, the three trajectory optimization strategies considered (*fuel-optimal*, *contrail-optimal*, and one trade-off option) are compared. The first noticeable result is that *fuel-optimal* trajectories fly at the highest mean altitudes, as observed in previous studies (Castino et al., 2021; Simorgh et al., 2023). In fact, when the *fuel-optimal* strategy is chosen, the optimizer selects altitudes close to

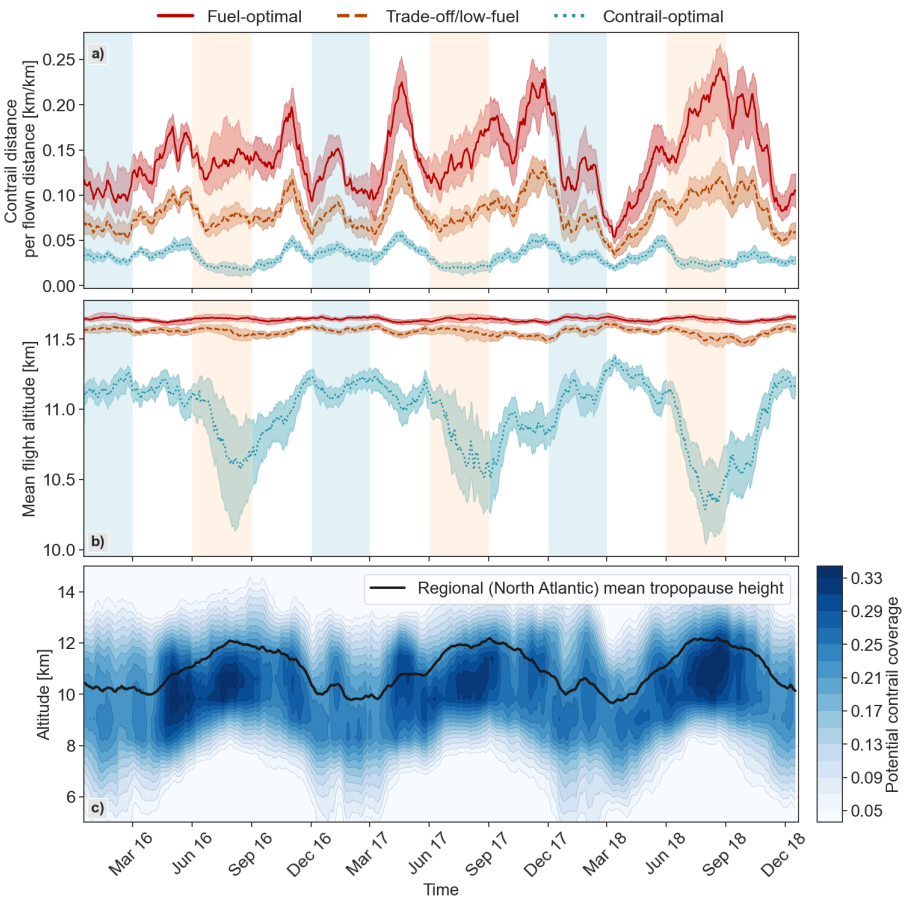


Figure 5.4: **Panels a and b:** comparison of trajectory properties obtained using different optimization strategies, i.e. 1) *fuel-optimal* (red, solid lines), 2) *trade-off/low-fuel* (orange, dashed lines), and 3) *contrail-optimal* (blue, dotted lines). Curves: median value over the air traffic sample. Shaded areas extend from the first to the third quartile. A 30-day running average is applied to the time series. Winter (light blue) and summer (light orange) are highlighted. **Panel c:** temporal and vertical variation of the average potential contrail cirrus coverage over the North Atlantic region (40°N-60°N, 80°W-5°W). Black line: regional mean tropopause height. As in panels a and b, a 30-day running average is applied.

the upper bound in flight levels (FL410), to minimize aerodynamic drag. If contrail distance is included in the objective function, the optimizer selects lower altitudes whenever this leads to a reduction in contrail formation, even at the cost of increasing fuel consumption. These results are affected by the choice of using *fuel-optimal* trajectories as reference scenario. In fact, a previous study (Yin. et al., 2018b) found an increase in altitude when contrail distance is minimized, having time-optimal trajectories as reference scenario. This highlights the importance of considering the characteristics of the reference optimization strategy, and their comparison to the actual air traffic, in order to correctly evaluate the impact of contrail avoidance in real life applications.

When our reference, *fuel-optimal* strategy is used, the aircraft fly at a constant altitude of about 11.6 km throughout the simulated period (Figure 5.4b). There is a relatively small difference between the mean flight altitudes of *fuel-optimal* and *trade-off* trajectories, as the latter fly on average at 11.5 km. The trajectories drop to lower altitudes (11.0 km on a yearly average) to minimize the formation of contrails. Moreover, a clear seasonal cycle is exhibited by the mean flight altitudes of *contrail-optimal* trajectories. During the summer, the lowest flight altitudes are flown, reaching 10.7 km on average, and the altitudes variability within the air traffic sample extends over the largest range. This may be due to more frequent altitude changes to reduce contrail formation in summer. This would be explained by the fact that the likelihood of forming contrails peaks below the tropopause and, in summer, the regional tropopause height increase up to the typical altitudes flown by our reference, *fuel-optimal* scenario (Figure 5.4c).

Figure 5.4c shows the potential contrail cirrus coverage, i.e. the fraction of the model grid box supporting persistent contrails, as it varies during the simulated period at different altitudes over the North Atlantic region. Moreover, Figure 5.4c includes the evolution of the regional mean tropopause height (black line). First of all, it is possible to observe how the potential contrail cirrus coverage increases towards the tropopause, usually reaching a maximum just below this level. Peaks in potential contrail cirrus coverage are in same cases associated to tropopause height rises. Above the tropopause, a sharp decrease in potential contrail cirrus coverage is found. This is expected, because of the dry atmospheric conditions observed in the stratosphere. As a consequence, the peak altitude of potential contrail cirrus coverage exhibits the same seasonal cycle as the regional mean tropopause height, which rises in summer and drops in winter. Moreover, particularly high mean values are observed during the summer at around 10-11 km of altitude, i.e., at those altitudes where the optimal trajectories fly (Figure 5.4b). It is important to highlight that this feature is highly dependent on the choice of focusing on the North Atlantic region. In fact, a different seasonality is observed over Europe (see Figure B.2 in Appendix B): in this case, the average potential contrail cirrus coverage increases in spring below the tropopause, and drops during the summer seasons at all flight levels, after a sudden rise in the tropopause height is observed (see Section 5.4 for more details).

5.3.2 Dependency of contrail avoidance on typical winter weather patterns

In this section, the day-to-day variability in benefits (in terms of contrail avoidance) and penalties (extra fuel) of different trajectory optimization strategies is analysed, focusing on winter weather patterns. As described in Section 5.2.3, the winter days occurring during our simulation period are classified according to five classes (Figure 5.2 and Table 5.3). Figure 5.5 shows the Pareto fronts that are obtained under each of these weather patterns. The median values of benefits and penalties are provided in terms of absolute values (Figure 5.5a) and relative changes with respect to the *fuel-optimal* scenario (Figure 5.5b).

Looking at Figure 5.5a, one can observe that the contrail formation is largest under the atmospheric conditions characterizing W3, which show similarities with the negative

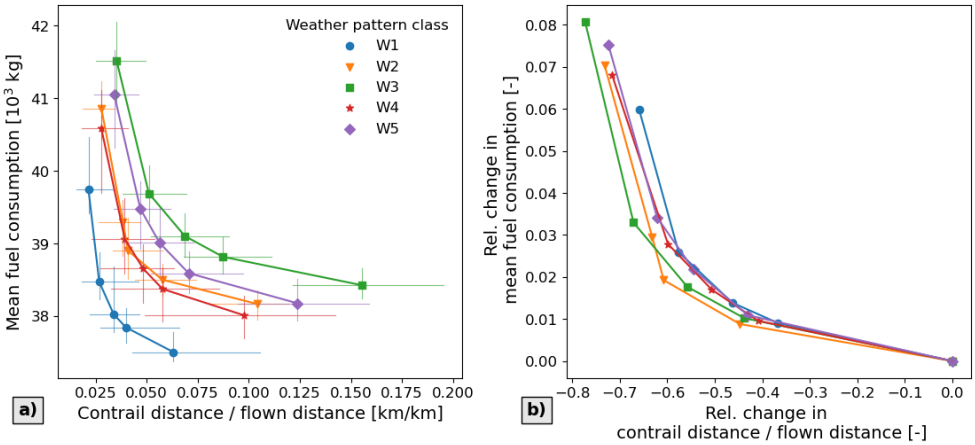


Figure 5.5: Comparison of the Pareto fronts obtained under different winter weather pattern classes, in terms of absolute values of the objective functions (Fig. 5.5a) and in terms of relative changes with respect to the *fuel-optimal* solution (Fig. 5.5b), averaging over the air traffic sample. The curves connect the median values over time of the different optimization strategies (*fuel-optimal*, *contrail-optimal*, and three trade-off solutions). Panel a: segments indicate the daily variability in both objectives along the Pareto fronts, extending from the first to the third quartile.

phase of the East Atlantic (EA) pattern. This weather pattern leads to the presence of a weak and tilted jet stream over the North Atlantic, as illustrated in Figure 5.2. Moreover, W3 corresponds to the highest fuel consumptions. This is motivated by the wind fields characterizing W3, as extra fuel is consumed to work against lateral winds. Contrarily, the fuel consumption tends to be lower in the presence of strong zonal winds, e.g. under the weather class W1 (Figure 5.2). In fact, strong zonal winds are beneficial to eastward flights, and can be easily avoided by westward flights. Under this type of weather (W1), a minimum in contrail distance is also achieved (Figure 5.5a, blue line). Figure 5.7 motivates the differences in contrail formation observed under W1 and W3, as explained in the next Section. Another interesting feature is that similar levels of fuel consumptions and contrails are obtained under both the positive and negative phases of the North Atlantic Oscillation (NAO), i.e., the W2 and W4 classes. The former, W2, is characterized by a strong and tilted jet stream, leading to a large variability in the average latitude of the *fuel-optimal* routes (Figure 5.8), while W4 presents no consistent strong winds. These two situations lead to similar Pareto fronts, as the curves relative to such days overlap (Figure 5.5a). Interestingly, the relative reduction in contrail distance that can be achieved changing routing strategy is affected by a lower variability (Figure 5.5b), although the largest (lowest) relative benefit is achieved under W3 (W1).

To better compare the difference in the mitigation potential of different weather pattern classes, the following quantity is calculated, as done in previous works (Matthes et al., 2017; Yin et al., 2018a; Castino et al., 2024):

$$k_x = \frac{f_{\text{cont},max} - f_{\text{cont},x}}{f_{\text{fuel},x} - f_{\text{fuel},min}} \qquad \text{[km(contrail)/kg(fuel)]} \tag{5.3}$$

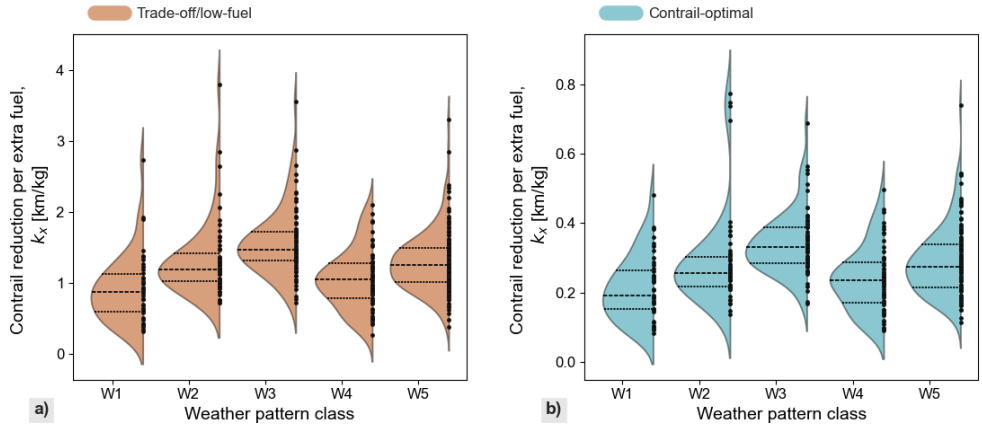


Figure 5.6: Distributions of k_x obtained over the simulated days, grouped by weather pattern class. Two trajectory optimization strategies are compared: trade-off solution strongly limiting fuel penalties (w_{fuel} = 0.75, panel a) and the extreme solution minimizing contrail distance (panel b). The dashed lines indicate quartiles, while the dots represent individual k_x values. Note that four outlier values are removed from the plot.

In other words, the parameter k_x [km(contrail)/kg(fuel)] represents the ratio between benefits (contrail distance reduction) and penalties (extra fuel) of the optimization strategy x (e.g., *contrail-optimal*, or one of the trade-off options) with respect to the *fuel-optimal* strategy. Firstly, comparing the two panels of Figure 5.6, one can see that the *trade-off/low-fuel* strategy leads to a factor of five higher contrail distance reduction per extra fuel burnt (Figure 5.6a) than minimizing contrail distance (Figure 5.6b). The general shape of the k_x distributions is similar under different weather pattern classes, although the mitigation potential is different. The highest average k_x values are achieved under the atmospheric conditions of W3, while the highest individual values are registered under W2, due to a subset of outlier points. Because of the definition of k_x (Eq. 5.3), these outliers may be linked situations where the deviations necessary to avoid contrail formation lead to minimal changes in the fuel burnt, compared to *cost-optimal* trajectories. Therefore, the distributions of the k_x values confirm that the beneficial conditions for contrail avoidance are most frequently found under W3 days, and with the lowest frequency on W1 days.

5.3.3 Potential contrail cirrus coverage under different weather patterns

Figure 5.7 represents the mean potential contrail cirrus coverage at 250 hPa, averaging over all days within each weather pattern class. Both the magnitude and general patterns agree with the ice-supersaturated regions described by previous studies, based on observations (Lamquin et al., 2012) and reanalysis data (Irvine et al., 2012). For

example, Figure 5.7 shows a maximum in potential contrail cirrus coverage over Greenland under all weather situations. Higher frequences of ISSRs in this region are reported in the literature, linked to air rising due the local orography. Moreover, we find that this maximum over Greenland is less pronounces under W4 and W5 (Figure 5.7d-e), which was also found by Irvine et al. (2012) analysing ISSRs under ERA-Interim data. Another feature shown by Figure 5.7 is that potential contrail cirrus coverage peaks south of the jet stream, motivating the variability in contrail formation under different weather classes. This result is also aligned with such previous studies, linking this maximum to the air rising in the storm track.

Figure 5.7 offers insights to interpret the properties of optimized trajectories under different weather patterns described in the previous section. For example, the higher contrail formation obtained under W3 can be attrebuted to the location of the jet stream on these days, which is further north than in the other weather classes (Figure 5.2c). This has two consequences: 1) our air traffic sample crosses the region where the potential contrail cirrus coverage peaks, just south of the jet stream, and 2) the regional mean tropopause is higher and with a lower slope over the North Atlantic, as it drops to lower altitudes at the jet stream location (see Figure S5 in the Supplement material). Similarly, it is possible to explain the lower contrail formation under W1. As the jet stream is strong, zonally oriented, and located further south over the North Atlantic, the flights tend to fly over an area of low contrail formation (Figure 5.7a), and at a higher distance from the tropopause, which is generally at lower altitudes (Figure S5 in the Supplement material).

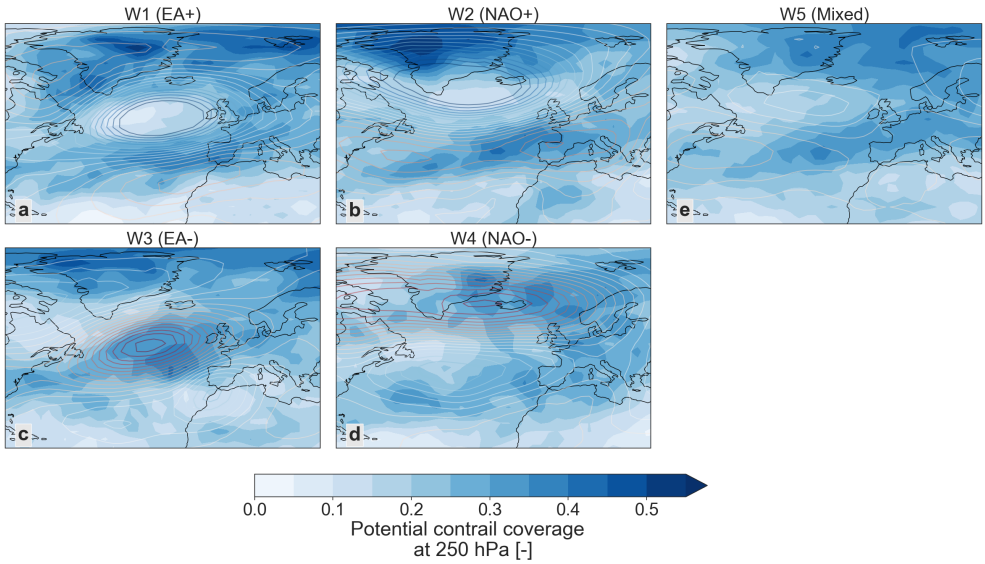


Figure 5.7: Average potential contrail cirrus coverage and geopotential height anomalies (contour lines) at 250 hPa [gpm] under the five weather pattern classes.

5.3.4 Properties of optimized trajectories under different weather patterns

Figure 5.8 provides an overview of the properties of the optimized trajectories under the five winter weather types W1-W5 (Section 5.2.3), comparing the optimization strategies defined in Table 5.2. Firstly, the mean flight altitude decreases gradually moving from *fuel-optimal* towards *contrail-optimal* (Figure 5.8a). The largest average decrease in altitude is obtained under W3, while the smallest occurs under W1. These observations corresponds to differences in the available benefit from contrail avoidance, discussed in the previous sections. As a result of flying through a region of low potential contrail cirrus coverage under W1 (Figure 5.7a), altitude changes are less frequent under this weather pattern class when varying routing strategy. The opposite occurs under the class W3.

In terms of lateral deviations, we distinguish between westward and eastward flights (Figure 5.8b and 5.8c, respectively). We notice a preference towards southward or northward deviations, depending on weather pattern class and flight direction. For example, westward (eastward) fuel-optimal routes fly more north (south) to avoid (take-advantage) of the strong and zonal jet-stream, with a low latitudinal spread. This result is aligned with the findings of (Irvine et al., 2012), which analysed one transatlantic route (London - New York), optimized with respect to its flight time over three winters between 2004 and 2010. In our study we also see that, to reduce contrail formation, the routes have a larger latitudinal spread, moving on average towards the centre of the region, where high potential contrail cirrus coverage is less likely (Figure 5.7a). Under W3 conditions, the jet stream is further north (Figure 5.2c), thus eastbound *fuel-optimal* trajectories are those located at the highest latitudes on average (Figure 5.8c), as in (Irvine et al., 2014a). Moreover, *trade-off* and *contrail-optimal* trajectories tend to fly even further north, since deviations south of the jet stream would lead to crossing the area where potential contrail cirrus coverage peaks. Looking at the latitudinal variations under W5, which collects days with no clear resemblance to the NAO or EA patterns, we can see the largest latitudinal spread and no clear preference towards southward or northward deviations (particularly evident for westward flights, Figure 5.8b), due to the absence of a consistent wind field over different days.

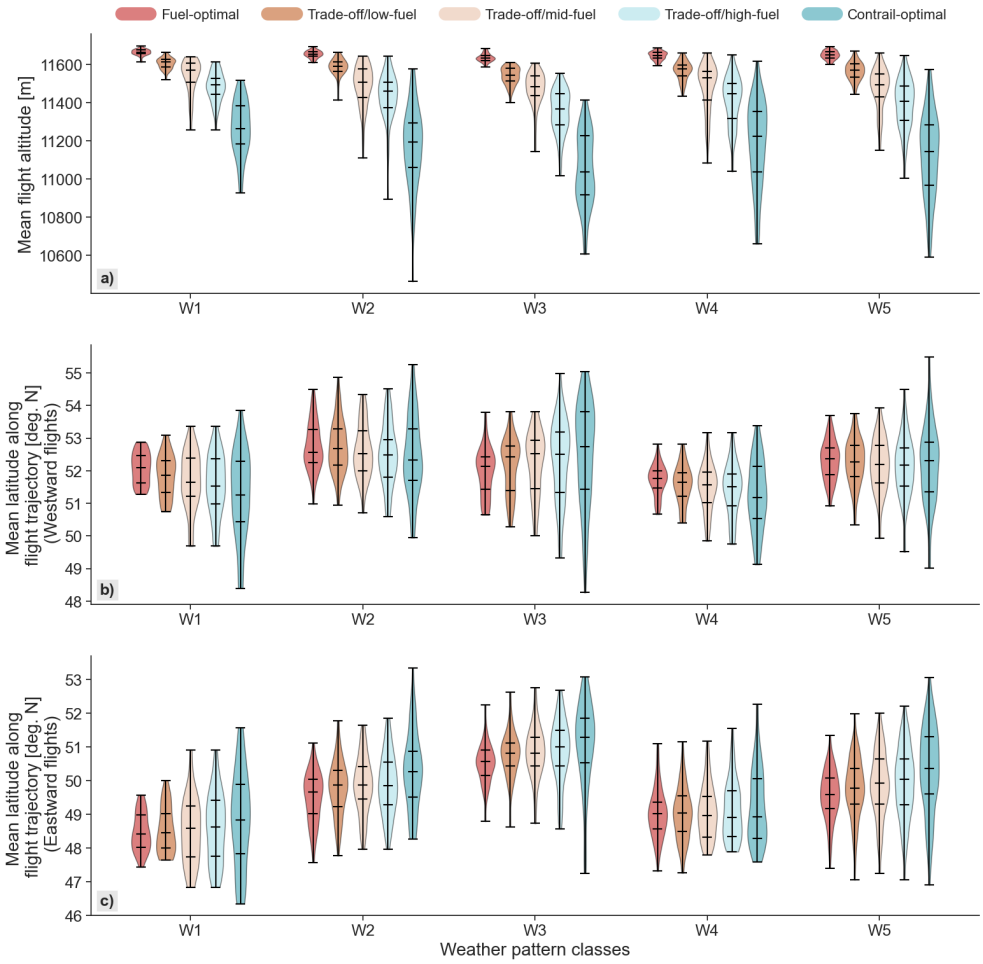


Figure 5.8: Distribution of trajectory properties obtained over the simulated days, grouped by weather pattern class. Five optimization strategies are compared: *fuel-optimal* (red), three trade-off options with increasing penalties in terms of fuel-use, and *contrail-optimal* (blue).

5.4 Discussion

We have analysed weather dependent mitigation potentials for different optimisation strategises including contrail avoidance, using the EMAC model. The main advantage offered by this model is that aircraft trajectories can be optimized based on the background atmospheric conditions at the time of departure (with resolution of 12 minutes, given by the model time step), considering a large number of days (Section 5.2). Therefore, we could explore the variability of optimized aircraft trajectories under a multitude of weather situations. However, the characteristics of this modelling chain introduce uncertainties in our results, that we discuss in this section.

Firstly, the EMAC model grid size does not resolve ISSRs, hence a parameterization is

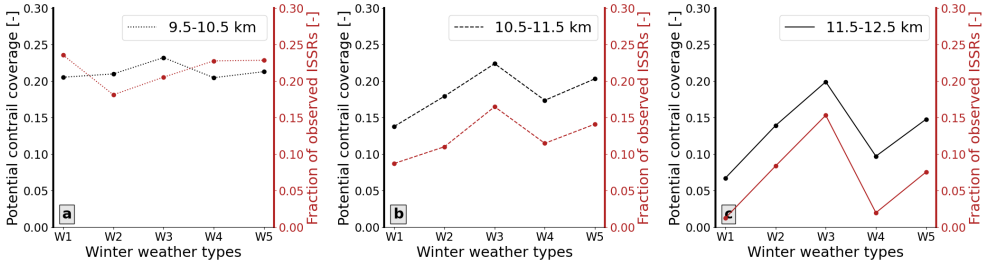


Figure 5.9: Comparison of potential contrail cirrus coverage, i.e., fraction of the EMAC grid-box where contrails can form and persist (black dots, left vertical axis) with frequency of ice-supersaturation conditions derived from IAGOS observations (red dots, right vertical axis). The three panels (a, b, c) show mean values relative different altitude ranges (9.5-10.5 km, 10.5-11.5 km, 11.5-12.5 km). All values are averaged over the North Atlantic region (40°N-60°N, 80°W-5°W). EMAC potential contrail cirrus coverage is averaged over the period from 1 December 2015 to 31 December 2018, while IAGOS fraction of observed ISSRs is relative to a 11-year dataset, from 3 December 2011 to 31 March 2022.

employed to compute the fraction of the model grid box that supports the formation of persistent contrails. This is defined as potential contrail cirrus coverage (Burkhardt et al., 2008, Chapter 3). To help evaluating the performance of the model at identifying ISSRs, Figure 5.9 compares the potential contrail cirrus coverage calculated by EMAC with the observations provided by IAGOS (In-service Aircraft for a Global Observing System). As the present study focuses on the North Atlantic Flight Corridor, this analysis includes data within 40°N-60°N and 80°W-5°W, where the air traffic is concentrated (Figure 5.1a). The comparison focuses on the extended winter months (DJFM), including three seasons simulated by EMAC (from 1 December 2015 to 31 March 2018) and 11 seasons from IAGOS (from 1 December 2011 to 31 March 2022). Using the IAGOS dataset, the frequency of occurrence of ISSRs along aircraft trajectories is calculated as the ratio between the number of points where ice-supersaturation occurs over the total number of measurements. Subsequently, the average frequency at three different altitude ranges (9.5-10.5 km, 10.5-11.5 km, 11.5-12.5 km) and under different winter weather patterns are derived. These mean values are compared to the average fraction of the EMAC grid-box where contrail can form and persist, defined as the average potential contrail cirrus coverage by Burkhardt et al. (2008). Both fields are linked to the probability of forming persistent contrails at a specific time and location. However, note that the fields differ in some aspects: the EMAC potential contrail cirrus coverage represents clear-sky, ice-supersaturated conditions where the Schmidt-Appleman Criterion (SAC) is satisfied, while the ice-supersaturated conditions derived from IAGOS include both clear-sky and in-cloud situations, as well as areas where the SAC is not satisfied. The relevance of distinguishing between clear-sky and in-cloud ISSRs has been recently highlighted by Petzold et al. (2025), showing that the conditions supporting persistent contrails are usually found in regions with pre-existing cirrus, and how this may impact their radiative effects. This aspect is considered in the parametrisation of the potential contrail cirrus coverage and, therefore, in the aircraft trajectory optimization strategies (Chapter 3).

Both fields in Figure 5.9 show a similar variability across altitude ranges and winter

weather types. The latter is particularly strong above 11.5 km, i.e. at the typical altitudes flown by our reference *fuel-optimal* trajectories (see Figure 5.4b). At this altitude range (11.5-12.5 km), both fields peak under W3, and are at least halved under W1 and W4. This comparison with IAGOS observations supports the results presented in Section 5.3.2, particularly weather pattern dependency of the contrail distance per flown distance of *fuel-optimal* trajectories (Figure 5.5a). Irvine et al. (2013) also found a lower (higher) probability of forming contrails under W1 and W4 (W2 and W3), attributing these variations on the flight time spent in the stratosphere.

Figure 5.10 represents the dependency between potential contrail cirrus coverage [-] and distance from the dynamical tropopause [hPa] (potential vorticity iso-surface of 3.5 PVU provided by the TROPOP submodel, Jöckel et al., 2006) under different seasons. Above the tropopause, the frequency of ice-supersaturation is expected to rapidly reduce to zero because of the dry stratospheric conditions (Reutter et al., 2020; Petzold et al., 2020). However, Figure 5.10 shows that conditions supporting persistent contrails formation are found in the lower stratosphere, up to ~100 hPa above the local tropopause. This overestimation of potential contrail cirrus coverage at high flight levels is aligned with previous findings, describing a "wet bias" in the extratropical lowermost stratosphere simulated by EMAC, due to horizontal diffusion of water vapour from the tropical upper troposphere (Stenke et al., 2008; Peter et al., 2025). This numerical diffusion across the tropopause is also responsible for a model "cold bias" of ~3 K in the temperature field, which affects the calculated potential contrail cirrus coverage (Yin et al., 2023; Peter et al., 2025).

The ranges of values of potential contrail cirrus coverage at different distances from the tropopause in Figure 5.10 compare well with the ISSR fraction over the North Atlantic presented by Hildebrandt et al., 2025 (see their Figure 12b). The main discrepancies are found in the lower stratosphere, as discussed above, and at the tropopause level during summer, where we found a peak in the potential contrail cirrus coverage. This difference could result from high humidity in this region during summer, combined with the "cold bias" of ~3 K discussed above (Yin et al., 2023; Peter et al., 2025). Therefore, additional work to better understand the impact of this wet and cold biases on the simulated potential contrail cirrus coverage is recommended.

Here, the fraction of the flights leading to persistent contrail formation is reduced via aircraft trajectory optimization. To fully evaluate the climate impact benefits of contrail avoidance, the impact of contrails on the climate system must be measured via a climate metric, such as Average Temperature Response (ATR), or Global Warming Potential (GWP). On-going research is developing tools that allowed to include this step in the evaluation of contrail avoidance as a climate mitigation strategy (Yin et al., 2023; Engberg et al., 2025).

Lastly, note that the reference scenario used to calculate changes in aircraft properties (Figure 5.5 and 5.6) is the *fuel-optimal* solution described in Section 5.3. This reference, *fuel-optimal* scenario flies at an altitude of about 11.6 km, which remains approximately constant for different city pairs and in time (Figure 5.4b). However, the actual North Atlantic air traffic presents a different vertical distribution (see supplement material, Figure S6). Our results show that contrail distance is highly dependent on the vertical distribution of the air traffic, thus it is important to note that the contrail impact

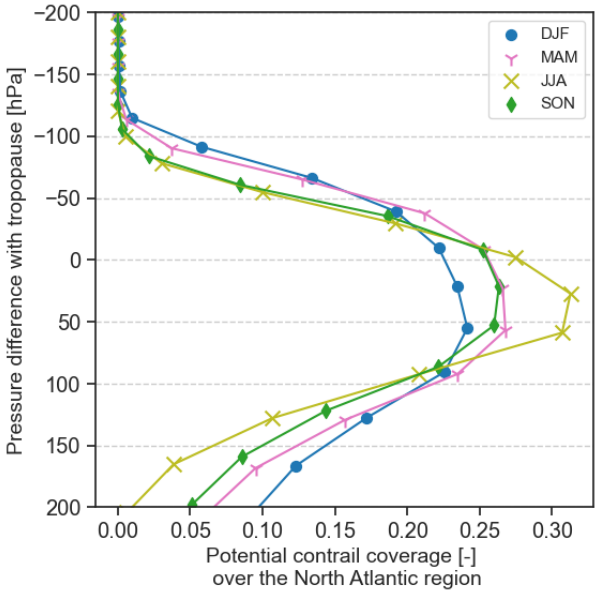


Figure 5.10: Seasonal mean vertical profiles of potential contrail cirrus coverage [-], averaged over the North Atlantic region (40°N-60°N, 80°W-5°W). Altitudes are indicated as distance from the dynamical tropopause. Each profile is relative to mean values over 3-month periods (DJF, MAM, JJA, SON) occurring from 1 December 2015 to 31 December 2018.

mitigation potential calculated here is relative to a reference scenario that differ from the trajectories that would actually be flown. For example, this study does not include airspace structure and limitations, which may reduce the possibility of avoiding ice-supersaturated regions in real-life trials and applications.

5.5 Conclusions

Five aircraft trajectories optimization strategies, minimizing fuel and contrail formation, are compared under a large number of weather conditions (1 December 2015 and 31 December 2018), simulated using the using the ECHAM/MESSy Atmospheric Chemistry (EMAC) model. All benefits and penalties are calculated relative to a reference, *fuel-optimal* scenario. This reference scenario differs from the air traffic that is actually flown, thus the mitigation potential achievable in real life might be lowered by limits not taken into account in this study. Nevertheless, using the *fuel-optimal* scenario, we compare solutions that minimize fuel and, consequently, CO_2 emissions, with strategies that include contrail avoidance. In other words, the strategies compared in this study illustrate the impact of prioritizing the reduction of CO_2 and non-CO_2 effects of aviations. The mitigation potential of contrail avoidance over the North Atlantic Flight Corridor (NAFC) is highly dependent on the weather situation, considering the variability of the relation between the absolute reduction in contrail distance and the corresponding increase in fuel burnt (Figure 5.5a). In particular, potential for larger

benefits is observed under a typical winter weather pattern characterised by pressure anomalies similar to those of the negative phase of the East Atlantic pattern (EA-). This weather pattern class (W3) is linked to a weaker jet stream, which is tilted and located further north over the Atlantic Ocean, resulting in a higher than average tropopause height and potential contrail cirrus coverage over the NAFC. Lower contrail distance reductions are achieved under days classified as W1 (EA+), linked to a strong a zonal jet stream. Taking advantage of (avoiding) the jet stream, eastward (westward) reach a minimal fuel consumption and contrail distance. The variability across weather patterns classes is lower, when considering relative changes in fuel burnt and contrail distance achieved by different optimization strategies.

With this study, we provide insights on which weather conditions are linked to the largest reductions of persistent contrails via aircraft trajectory optimization, and we analyse the trends in the corresponding changes in fuel use, flight altitude, and horizontal path. These results can provide useful insights towards the development and testing of tools to better forecast ISSRs and assess contrail avoidance as an operational strategy to reduce the climate impact of aviation.

6

Seasonal variability of aircraft trajectories reducing NO_x-climate impacts under a multitude of weather patterns

In this chapter, we explore the relation between NO_x-climate impacts and routing strategies. To this end, the model described in Chapter 3 (EMAC) is employed. We conduct simulations over 37 months with the air traffic EMAC submodel AirTraf 3.0, which includes the SolFinder module to identify alternative routing strategies (Chapter 4). We consider the same air traffic sample analysed in Chapter 5, including 100 North Atlantic routes. Here, we optimize aircraft trajectories with respect to their Simple Operating Costs (SOC), and the climate impact from NO_x emissions. A set of prototype algorithmic Climate Change Functions (aCCFs) is used to identify routes that reduce the expected climate impact from NO_x emissions. The resulting mean flight altitudes of optimized trajectories show seasonal and latitudinal dependencies. The potential of reducing ozone effects from aviation NO_x is subjected to a strong seasonal cycle, reaching a minimum in summer. The modelling chain can be adapted to use new approaches for the estimation of NO_x-climate impact (Chapter 7).

This Chapter is based on an adaptation of the results presented in *Castino, F., Yin, F., Grewe, V., Soler, M., Simorgh, A., Yamashita, H., Matthes, S., Baumann, S., Linke, F., and Lührs, B.: Seasonal Variability of Aircraft Trajectories reducing NO_x-climate Impacts under a Multitude of Weather Patterns, 11th SESAR Innovation Days, 2021, https://resolver.tudelft.nl/7bbf56c6-63bd-4645-b183-560002cb4190.*

6.1 Introduction

The impact of non-CO_2 effects, including those from NO_x emissions, on the climate system has been shown to be highly dependent on cruise altitude and geographical location of the aircraft (Köhler et al., 2013; Matthes et al., 2021). Therefore, previous studies highlighted the potential of mitigating the climate impact of aviation by optimizing the aircraft trajectories (Grewe et al., 2014b; Grewe et al., 2017b; Lührs et al., 2021; Matthes et al., 2020). However, these studies focused on a limited number of representative days, because of the large computational costs related to estimating the climate impact of a unit emission occurring at a specific time and location. The objective of this chapter is to explore the properties of optimized aircraft trajectories, and their variability under a large number of weather patterns, comparing three optimization strategies, i.e., *cost optimal*, *NO_x-climate optimal*, and *trade-off* trajectories (Section 6.2.3).

To achieve this objective, we conduct multi-annual simulation (from 1 December 2015 to 31 December 2018) with the EMAC model (Chapter 3). Here, two submodels have a key role: 1) AirTraf, which optimizes an air traffic sample of 100 North Atlantic routes, and 2) ACCF, implementing a prototype version of the algorithmic Climate Change Functions, to identify which regions of the atmosphere are more or less sensitive to aircraft emissions (Section 6.2). The model output is analyzed in Section 6.3, and our results are discussed in Section 6.4. To conclude, we present our plans to further explore the mitigation potential of optimizing aircraft trajectories w.r.t. the climate impact of their emitted species (Section 6.5).

6.2 Methods

6.2.1 Base model

The EMAC model, described in detail in Chapter 3, is employed in the present study in the T42L31ECMWF-resolution, i.e. with a spherical truncation of T42 (corresponding to a quadratic Gaussian grid of approx. 2.8 by 2.8 degrees in latitude and longitude) with 31 vertical hybrid pressure levels (up to 10 hPa ~ 30 km of altitude). We apply a time step of 12 minutes, and we set the simulation duration from 1 December 2015 to 31 December 2018. The simulations are nudged down to the surface towards the ECMWF ERA5 reanalysis data (Hersbach et al., 2020). The applied model setup comprised the submodels ACCF (Yin et al., 2023) and AirTraf (Yamashita et al., 2020). Note that these sub-models are currently under development (further information on their status can be found at https://www.messy-interface.org). Therefore, in this study, we illustrate the preliminary results obtained using the current versions of these sub-models, to analyse the model behaviour under different routing strategies. Table 6.1 summarizes the settings of the model that were employed to run our simulations.

6.2.2 Sub-model AirTraf

In our simulations, air traffic is simulated by the EMAC sub-model AirTraf 3.0, as described in Chapters 3 and 4 (Yamashita et al., 2020; Castino et al., 2024). A North Atlantic air traffic sample (identical to the one employed in Chapter 5) is optimized on every simulation day. The air traffic sample includes 100 different routes, defined by their origin-destination pair and their departure times, which are distributed throughout

Table 6.1: Summary of the model setup employed in our simulations.

	ECHAM5
Horizontal resolution	T42 (2.81° × 2.81°)
Vertical resolution	L31ECMWF (31 vertical pressure levels up to 10 hPa ~ 30 km)
Time step	12 min
Duration	from 1 Dec. 2015 to 31 Dec. 2018 (37 months)
	AirTraf
Air traffic sample	100 North Atlantic flights
Aircraft	A330-301 model
Waypoints	101
Optim. Objectives	SOC, $ATR20_{NO_x}$

the day (Figure 5.1 in Chapter 5). Various routing strategies are available: each option optimizes a specific objective function, e.g. representing fuel used, operating cost, or the climate impact of a flight. As described in Chapter 4, AirTraf was further developed to efficiently solve multi-objective optimization problems (AirTraf 3.0), and it currently includes the decision-making module SolFinder, to idenitfy an individual optimal solution that satisfies a set of criteria. Here, we compare three solutions, which are described in detail in the following section.

6.2.3 Routing optimization strategies

We conduct three simulations with the model setup described in the previous paragraphs, varying only the route optimization strategy to obtain the following three scenarios:

1. *Cost optimal* trajectories, minimizing the Simple Operating Costs (SOC), defined as the weighted sum of fuel burnt and flight time. Note that we use a simplified definition of the operational costs, as the aim of this optimization strategy is to take into account both flight time and fuel use. Therefore, the objective function values are calculated with the following formula (Cook et al., 2009; Marla et al., 2017):

$$\mathrm{SOC} = c_t \sum_{i=1}^{n_{\mathrm{wp}}-1} \mathrm{TIME}_i + c_f \sum_{i=1}^{n_{\mathrm{wp}}-1} \mathrm{FUEL}_i \tag{6.1}$$

   where $n_{\mathrm{wp}} = 101$ are the number of waypoints; TIME_i and FUEL_i are flight time and fuel used at the i^{th} flight segment; c_t [$/s] and c_f [$/kg] are the unit time and unit fuel costs, respectively, assuming the values $c_t = 0.75$ $/s and $c_f = 0.51$ $/kg (Yamashita et al., 2020; Burris, 2015).

2. *NO_x-climate optimal* trajectories, minimizing the climate impact of NO_x emissions in terms of Average Temperature Response over 20 years (ATR20); this is represented by the sum of the ozone and methane effects, which are individually computed by the model using a set of prototype aCCFs (Manen et al., 2019; Yamashita et al., 2020; Yin et al., 2023):

$$ATR20_{NO_x} = ATR20_{O_3} + ATR20_{CH_4} + ATR20_{PMO} \tag{6.2}$$

   Note that we take into account changes in primary mode ozone caused by the CH_4 depletion, although we neglect the feedback on the stratospheric water vapour (Manen et al., 2019; Yin et al., 2023).

3. *Trade-off* solutions, providing a compromise solutions between the two extreme scenarios above. This point is selected using the SolFinder strategy based on the VIKOR method (Chapter 4), which uses geometric methods to identify an optimal solution at a specific distance from each extreme point of the Pareto front. Here, we set the relative weights of the objectives to $w_{SOC} = 0.75$ and $w_{NOx} = 0.25$ (with $\gamma = 0.5$). In other words, a higher importance is given to limiting cost increases (and, indirectly, CO_2 emissions) rather than achieving the largest available reductions in $ATR20_{NO_x}$. More details on the VIKOR settings are provided in Chapter 4.

6.3 Results

6.3.1 Mean flight altitudes and horizontal paths

First of all, we look at the differences between the trajectories obtained in the two extreme scenarios, minimizing only the climate impact of NO_x or operational costs, respectively. An example of such differences is illustrated in Figure 6.1, which showcases ten *cost-optimal* and *NO_x-climate optimal* trajectories on the last simulation day (31 December 2018). The green and solid curves, representing *NO_x-climate optimal* trajectories, often show large deviations from *cost-optimal* solutions (red, dashed lines), and the former tend to fly further north the latter. To better identify trends in vertical and horizontal path changes over a larger number of flights, Figure 6.2 illustrates the distributions of mean flight altitudes (Figure 6.2a) and latitudes (Figure 6.2b). Each distribution includes all the individual flights optimized over the simulation period.

Figure 6.2a shows that the mean altitude characterizing each flight is highly affected by the choice of routing strategy. Trajectories minimizing SOC are flying at the highest altitudes, with a small range of variability. This is in line with our expectations, since *cost-optimal* trajectories minimize the sum of fuel use and flight time and, to reduce aerodynamic drag, high altitudes are preferred. In contrast, the trajectories minimizing NO_x effects generally prefer lower flight altitudes. This is because the residence time of O_3 at lower altitudes is shorter, due to more efficient removal processes, reducing the resulting warming effects of the increased O_3 concentrations due to NO_x emissions. In fact, this tendency of "flying lower" to reduce NO_x-climate impact is in line with results from previous studies (Grewe et al., 2002; Frömming et al., 2012; Søvde et al., 2014; Matthes et al., 2021).

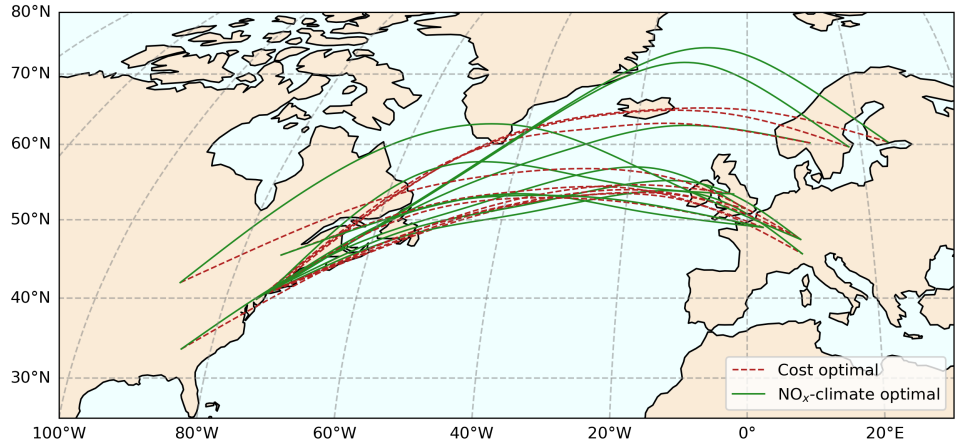


Figure 6.1: Trajectories of ten transatlantic routes optimized on the last simulation day (31 December 2018), comparing the two extreme optimization strategies: cost-optimal (red, dashed) and *NO_x-climate optimal* (green, solid) solutions.

Considering the changes in the horizontal path (Figure 6.2b), it is possible to observe that *NO_x-climate optimal* flights show a northward shift of aircraft locations, as already showcased by the examples in Figure 6.1. This is in agreement with previous studies, which found a decrease in the impact of NO_x emissions towards higher latitudes (Köhler et al., 2008).

Looking at the distributions of *trade-off* trajectories, it is possible to observe that flying at lower altitudes to reduce the climate impact of NO_x emissions is preferred by the optimizer to limit the penalties in terms of simple operating costs, rather than flying further north.

Taking advantage of the large number of days considered, we can further look at seasonal variabilities, to better interpret the trends observed in Figure 6.2. To this end, Figure 6.3 shows two dimensional histograms of flight altitudes and latitudes, comparing winter (December to February, DJF) and summer (June to August, JJA) months. Moreover, the seasonal mean tropopause height, averaged over the North Atlantic region (40°N-70°N, 80°W-5°W) is included in all panels (black, dashed lines). Here, it is possible to observe the relation between tropopause height and mean flight altitudes of *trade-off* and *NO_x-climate optimal* trajectories. As the mean tropopause height is lower in winter than in summer, the trajectories tend to fly much lower in the former season. Moreover, altitudes of *NO_x-climate optimal* trajectories present a strong dependency on latitude, which is not visible in the *cost-optimal* option. Using the *NO_x-climate optimal* strategy, the flight altitude increases towards lower latitudes, following the increasing average height of the tropopause (black, dashed curve). This model behaviour can be expected, considering that the upper-troposphere is characterised by a sharp increase in the NO_x climate impact, related to a high ozone production rate (Köhler et al., 2008). Therefore, the location of the tropopause is crucial in determining the cruise altitude of *NO_x-climate optimal* trajectories.

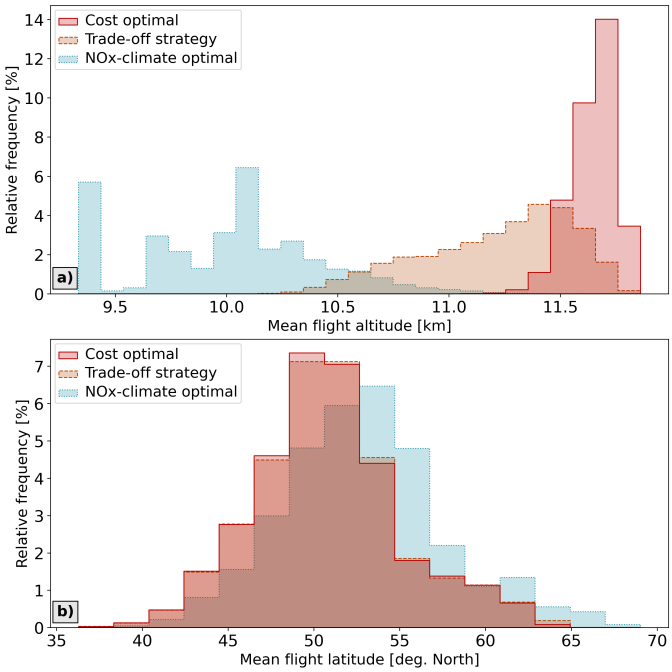


Figure 6.2: Distributions of flight altitudes (panel a) and latitudes (panel b), averaging over all waypoints of each optimized trajectory. Each distribution includes a total of 112573 points, considering 100 flights optimized on 1126 days (27 null values from the model output are excluded). Three trajectory optimization strategies are compared: *cost-optimal* (red, solid steps), *trade-off* (orange, dashed steps) and *NO_x-climate optimal* (blue, dotted) flights.

6.3.2 Time-evolution of changes in fuel use and flight time

Figure 6.4 shows the evolution of flight altitude, flight time, fuel use, and Simple Operating Cost during the year of simulation. A 7-days running average is applied. Figure 6.4a compares the flight altitude of *cost-optimal* (red, solid), *trade-off*, and *NO_x-climate optimal* (blue, dotted) trajectories. We can see that there is no evident seasonal variability in the flight altitude of *cost-optimal* trajectories, as its values remain constant throughout the year, and with a reduced variability over the air traffic sample. On the other hand, the reduction in the cruise altitude of *NO_x-climate optimal* trajectories is larger in winter than in summer. As discussed in the previous Section 6.3.1, this is linked to the elevation of the average height of the tropopause during the summer season, which determines the cruise altitude of *NO_x-climate optimal* trajectories. Moreover, the extension of the shaded area shows that the variability within the set of flights is larger using the *NO_x-climate optimal* strategy.

Figure 6.4b-6.4c show that the evolution of fuel increase also follows a strong seasonality, driven by the increase in aerodynamic drag caused by flying at lower altitudes. We can observe that the relative changes in flight time are also larger in winter than in the other seasons months, but they are usually negligible compared to the changes in fuel use. Therefore, the increase in SOC is driven by the increment in fuel use.

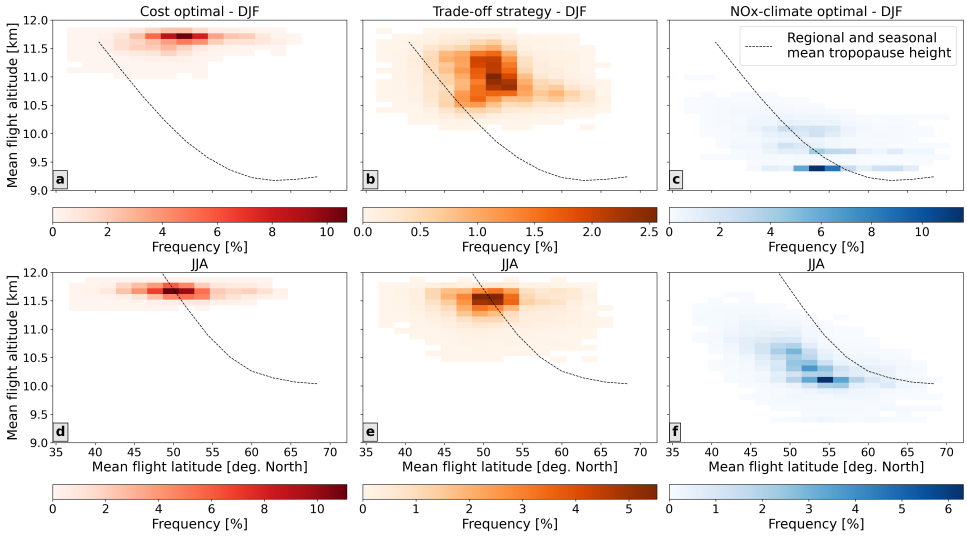


Figure 6.3: Two dimensional histograms of flight altitudes [km] and latitudes [degrees North], averaged over all the waypoints of an individual flight. Panels a-c: average over all winter months (December to February, DJF). Panels d-f: average over all summer months (June to August, JJA). Three trajectory optimization strategies are compared: *cost-optimal* (panels a and d), *trade-off* (b and e) and *NO_x-climate optimal* (c and f) flights. Black, dashed curves in each panel represent the seasonal mean tropopause height, averaged over the North Atlantic region (40°N-70°N, 80°W-5°W).

Moreover, comparing Figure 6.4b and Figure 6.4c, we can observe that the *trade-off* strategies successfully limits the operating costs changes. In fact, increases in fuel use with respect to the *cost-optimal* solution range between ~ 2 – 5% when the *trade-off* strategy is selected, but the bounds of this range are about 5 times higher for *NO_x-climate optimal* flights. The variability of the relation between climate benefits and operating costs will be further discussed in Section 6.3.4.

6.3.3 Changes in climate impact of NO_x emissions

In this section, we look at the effects of minimizing $ATR20_{NO_x}$ on the two elements contributing to the climate impact of NO_x emissions, i.e., their effects on ozone (increase in $ATR20_{O_3}$) and methane ($ATR20_{CH_4}$ decrease). Figure 6.5a shows the total aviation climate impact from NO_x emissions ($ATR20_{NO_x}$), combining ozone and methane effects.

Ozone effects present a larger magnitude than those of methane, thus the seasonality of the $ATR20_{O_3}$ relative variations (Figure 6.5b) emerges also in Figure 6.5a. We find that the impact of NO_x through ozone effects reaches a maximum in summer (Figure 6.5b), under all trajectory optimization strategies. This result is due to a higher photochemical activity in summer, and it is in agreement with previous studies (Søvde et al., 2014; Manen et al., 2019).

During winter and spring, the $ATR20_{O_3}$ values are significantly reduced by *NO_x-climate optimal* trajectories. This could be due to the fact that vertical and latitudinal gradients in temperature and geopotential (input fields to calculate the ozone

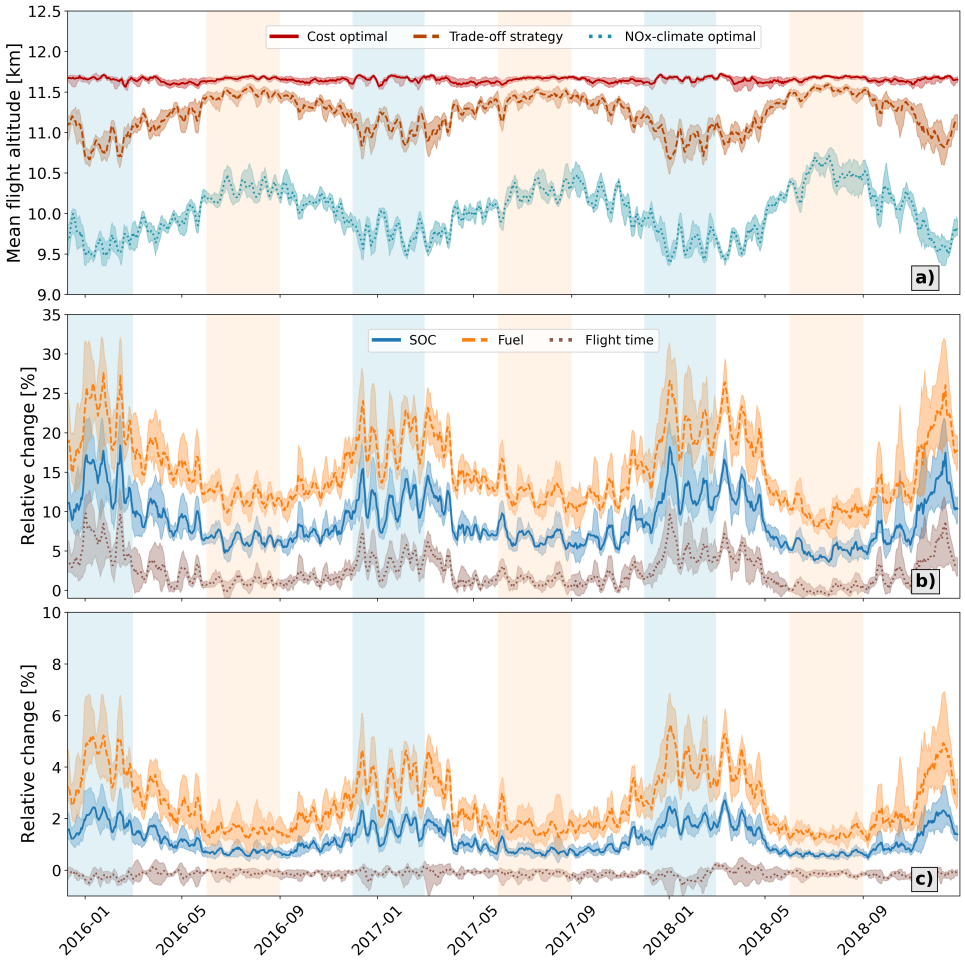


Figure 6.4: Panel a: evolution of flight altitude [km], averaged over the trajectory waypoints, comparing *cost-optimal* (red, solid curve), *trade-off* (orange, dashed curve) and *NO_x-climate optimal* (blue, dotted curve) flights. Panel b: evolution of the relative change in Simple Operating Costs (blue, solid curve), fuel (orange, dashed curve), and flight time (brown, dotted curve) of *NO_x-climate optimal* trajectories w.r.t. *cost-optimal* ones. Panel c: same as panel b, but showing relative differences between *trade-off* and *cost-optimal* trajectories. All panels: thick lines indicate the median values over the 100 routes included in the air traffic sample, shaded areas extend from the first to the third quartile. All curves represent the 7-days running average over the dataset.

aCCF Manen et al., 2019) are larger in this period of the year. In winter and spring, the jet stream is stronger and located further south than during the summer (Archer et al., 2008), leading to sharper temperature and geopotential gradients over the North Atlantic region. Therefore, the large mitigation potential in winter would be linked to (1) larger meridional mass exchange, hence large possibility to transport an air parcel to the tropics, and (2) larger difference in chemical activity between mid latitudes and tropics (Rosanka et al., 2020). The $ATR20_{O_3}$ reduction achieved flying *NO_x-climate optimal*

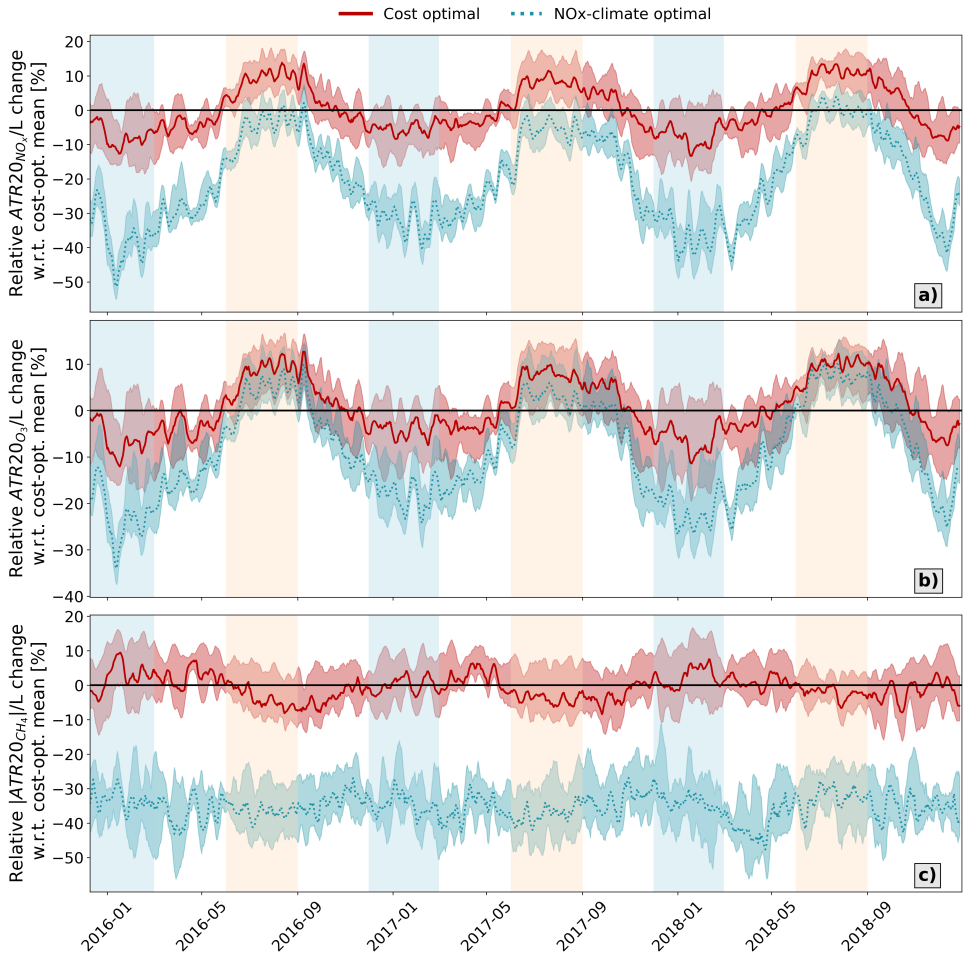


Figure 6.5: Evolution of the relative change of aviation climate impact from NO_x emissions, comparing *cost-optimal* (red, solid curves) and *NO_x-climate optimal* trajectories (blue, dotted curves). The ATR20 values are weighted against the total flight length, *L*, of *cost-optimal* trajectories. The yearly mean value from the *cost-optimal* strategy is chosen as reference (black lines) for each panel, and it assumes the values 1.45×10^{-12} K/km, 1.84×10^{-13} K/km, and -3.95×10^{-13} K/km, for panel (a), (b), and (c), respectively. The thick curves represent the median values over the 100 routes included in the air traffic sample, while the shaded regions extend from the first to the third quartiles. A 7-days running average is applied over the dataset.

trajectories is minimal in summer, when the jet stream is weaker and shifted northward.

Figure 6.5c shows the variability of net-cooling effects (i.e., reduced warming) due to methane depletion, which is induced by NO_x emissions (Chapter 2). To represent this net-cooling effect, $ATR20_{CH_4}$ is always negative (Manen et al., 2019). Therefore, the magnitude of methane effects ($|ATR20_{CH_4}|$) presents the same seasonality of the magnitude of ozone effects ($|ATR20_{O_3}|$, panel b), as we observe larger net-cooling effects from methane depletion in summer than in winter. This seasonality is less evident in

NO_x-climate optimal trajectories. Net-cooling NO_x effects are always enhanced by *NO_x-climate optimal* trajectories throughout the year, thus the difference between the two strategies is larger in winter and spring, when $|ATR20_{CH_4}|$ reaches its minimum value in the *cost-optimal* scenario.

6.3.4 Relation between climate benefits and economic costs

Figure 6.6 shows the seasonal mean Pareto fronts, i.e., the seasonal variability of the changes in SOC and $ATR20_{NO_x}$ obtained using different trajectory optimization strategies. Here we compare the four meteorological seasons, extending from December to February (DJF), March to May (MAM), July to August (JJA), and September to November (SON).

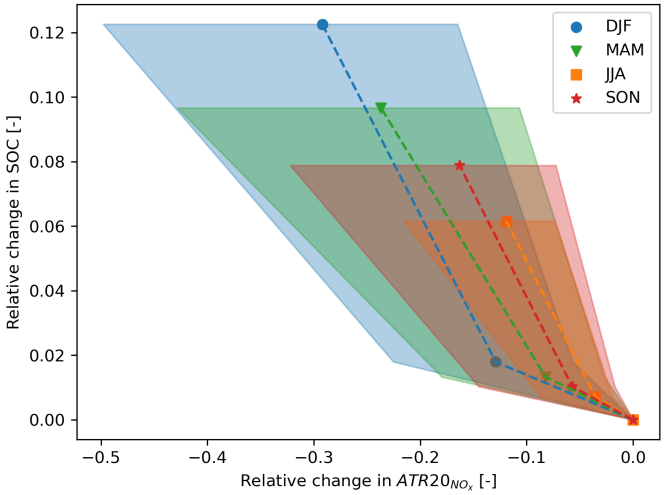


Figure 6.6: Comparison of the Pareto fronts obtained under different seasons, in terms of relative changes with respect to the *cost-optimal* solution. Firstly, SOC and ATR20 values are summed over all waypoints in an individual trajectory (total climate impact and operating costs of each flight). Subsequently, the average over the 100 flights in the air traffic sample is computed. The connected points indicate seasonal averages, while the shaded areas extend between the minimal and maximal daily $ATR20_{NO_x}$ relative changes. The dashed lines connect the mean values over time of the three optimization strategies (*cost-optimal*, *NO_x-climate optimal*, and *trade-off* solutions).

First of all, it is possible to observe that the extension of the Pareto fronts is highly dependent on the season. As explained in previous section, a larger climate impact reduction from NO_x emissions can be achieved during winter. Looking at Figure 6.6, we can see that winter is also the season with the largest day-to-day variability in $ATR20_{NO_x}$ relative reductions, reaching ~ 50%. On average, an almost 30% decrease in $ATR20_{NO_x}$ can be achieved with a 12% increase in the operating costs. Because this SOC increase may be unaffordable, and it is also linked with a increase in CO_2 emissions which would affect the climate system on long time-scales, we are interested in considering trade-off solutions between the extreme strategies. Here, in winter, we obtain an average decrease in $ATR20_{NO_x}$ larger than 10%, at a limited SOC increase (2%). The potential of reducing

the climate impact of NO_x emissions via trajectory optimization reaches a minimum on summer, when the average $ATR20_{NO_x}$ change is almost as low as the lowest winter value.

6.4 Discussion

This study aims at enhancing the understanding of the relation between NO_x-climate impacts and routing strategies, exploring how the systematic application of different routing strategies in a global atmospheric model produces a set of alternative trajectories which are intended to have a smaller climate effect due to NO_x emissions. As a reference scenario, we consider *cost-optimal* trajectories, minimizing Simple Operating Costs (SOC). Our calculation of SOC comprises both costs of fuel and time, assuming a linear dependence between costs of time and time of flight (Section 6.2.3). If one would intend to consider extra costs due to delay time, a linear relationship would not be realistic. However, in our concept of alternative trajectories planning, these costs of time represent those costs due to longer working hours and usage of the aircraft. Other costs, such as route charges, are neglected in the calculation of economic costs (SOC) in our analysis, as a simple relationship between time and costs would not be realistic. Nevertheless, since the operating costs are mainly determined by flight time and fuel used, variations in these two quantities are monitored considering SOC as optimization objective (Yamashita et al., 2020).

Please note that we rely on the algorithmic Climate Change Functions (aCCFs) to calculate and compare the climate impact of different routing strategies. This innovative methodology has the advantage of significantly reducing the computational time, allowing to perform trajectory optimization. Previous studies tested that using the ozone aCCFs as objective function, the EMAC submodel AirTraf identifies trajectories that reduce the radiative forcing from NO_x emissions (Yin. et al., 2018b; Rao et al., 2022). On-going research is addressing the source of uncertainties that affect the current climate impact estimates (Matthes et al., 2021). These are originated, for example, by (1) the calculation of the RF from the emitted species/contrails, and (2) the conversion from the RF values to the selected climate metric (ATR20). Moreover, the representation of atmospheric processes in the EMAC model is subjected to uncertainties, affecting the meteorological fields that are used as input for the aCCFs. Therefore, these sources of uncertainties must be taken into account interpreting the output of our model simulations.

6.5 Conclusion

Our study confirms the climate mitigation potential of aircraft trajectories optimization (Grewe et al., 2014b; Lührs et al., 2021). In particular, here we show that the newly developed version of AirTraf, including the decision-making module SolFinder, identifies optimal trajectories under a wide range of background atmospheric conditions, leading to a significant reduction of climate effects of aviation, while limiting penalties in terms of fuel use and flight time. We employed the EMAC sub-model AirTraf 3.0 to optimize 100 aircraft routes within the North Atlantic airspace, simulating the atmospheric conditions from 1 December 2015 to 31 December 2018. Subsequently, we analysed the

variability of the properties characterizing *cost-optimal* and *NO_x-climate optimal* trajectories. Stressing again that we consider our current results as an initial study relying on prototype estimates of non-CO_2 effects, the main results and the next steps of our research are:

- The potential of reducing ozone effects from aviation NO_x is subjected to a strong seasonal cycle, reaching a minimum in summer.
- The seasonal mean flight altitudes of *NO_x-climate optimal* trajectories are lower than those of *cost-optimal* ones. The difference between the two strategies follows a seasonal cycle, with a reduction in the variation during summer months, when the average tropopause height increases, and the potential of reducing NO_x effects decreases.
- Especially during winter months, *trade-off* solutions offer large reductions in $ATR20_{NO_x}$ (on average, > 10% in winter) at lower changes in the operating costs (< 2%) than *NO_x-climate optimal* trajectories.
- On-going research is addressing the sources of uncertainty that affect the current climate impact estimates, e.g. due to the aCCFs implementation, and to the meteorological fields at emission location (Matthes et al., 2021).

7

Discussion

"...Where there are threats of serious or irreversible damage,
lack of full scientific certainty
shall not be used as a reason for postponing
cost-effective measures to prevent environmental degradation."

From Principle 15
of the United Nations Rio Declaration
on Environment and Development, ***1992***

In this Chapter, the key assumptions and open questions related to the work presented in this thesis are discussed. Three main areas are examined, considering their crucial role in the identification of eco-efficient aircraft trajectories. Firstly, fast assessment models are necessary to quantify aviation non-CO_2 effects within the framework of an air traffic optimizer. Since high-fidelity models are too computationally expensive for this task, prototype tools to estimate the spatio-temporal variability of non-CO_2 effects have been developed. Chapter 7.1 examines the advantages and disadvantages of such tools. Secondly, limitations introduced to reduce the complexity of the multi-objective optimization problems analysed in this thesis are discussed. These limitations originate, for example, by optimizing aircraft trajectories individually, without considering network effects and airspace regulations (Chapter 7.2). Lastly, a crucial open question in the field concerns the weighting of potential trade-offs between CO_2 and non-CO_2 effects. In fact, whether a specific climate mitigation measure will reach its target may depend on the relative importance assigned to these different effects, unless win-win strategies (reducing both fuel consumption and non-CO_2 effects) are implemented (Chapter 7.3). Therefore, this Chapter provides recommendations for future research, considering the findings and limitations of this thesis.

7.1 Quantifying aviation non-CO_2 effects with fast assessment models

Non-CO_2 effects of aircraft emissions depend on the time and location of the flights. This dependency is a key concept in this thesis, as it offers the possibility of

reducing aviation climate impact via alterations in aircraft trajectories. At the same time, this high variability is difficult to capture with measurements or models, because the interactions between aircraft emissions and the environment operate over a wide range of time and spatial scales. For example, the formation and radiative impact of persistent contrails are determined by microphysical and macrophysical processes, as well as large scale meteorological phenomena. Estimating the impact of a pulse emission of NO_x on short-term ozone concentrations at a specific time and location requires computational expensive simulations with atmospheric-chemistry models (e.g. Maruhashi et al., 2022). Therefore, comprehensive approaches to simulate non-CO_2 effects are not compatible with the resolution of optimization problems aiming to identify aircraft trajectories that minimize these non-CO_2 effects. Nevertheless, solving such optimization problems requires information on the variability of non-CO_2 effects in time and space. Moreover, such data has to be available with a sufficiently high resolution and at low computational cost, so that a large number of alternative trajectories with varying vertical profiles and horizontal paths can be compared. The first version of the algorithmic Climate Change Functions (aCCFs 1.0, Yin et al., 2023) comprises a set of prototype functions that satisfy these requirements (Chapter 3). In the following paragraphs, the advantages and limitations of this approach, and its use in this thesis, are discussed.

The aCCFs consists of simple relationship between weather fields (such as potential vorticity, geopotential, temperature) and the climate impact of aircraft emissions. This concept relies on the identification of a limited number of variables that are the most relevant indicators of the radiative forcing from contrails, NO_x emission, and H_2O. For example, Manen et al. (2019) identified potential vorticity (PV) as the best predictor for the radiative forcing from H_2O emissions at cruise altitudes (RF_{H_2O}). Simple regression techniques are then employed to find a correlation between PV and RF_{H_2O}, based on an original dataset - called Climate Change Functions, CCFs (Grewe et al., 2014a) - obtained via computationally expensive simulations (see Chapter 3). The choice of using PV as predictor for H_2O is supported by a clear physical interpretation. In fact, PV is low in the troposphere (where H_2O quickly leaves the atmosphere via the water cycle) and high in the stratosphere (where H_2O has longer residence times, resulting in stronger greenhouse effects from its emissions). Indeed, the definition of the dynamical tropopause is based on threshold PV values. In other words, PV is an good indicator for the main patterns of variability of RF_{H_2O} in space and time (Manen et al., 2019). In other cases (aCCFs of NO_x-methane, contrails), the relationship between atmospheric variable(s) and radiative forcing is unclear. In Manen et al. (2019), the choice of predictors used for the NO_x-methane aCCF (geopotential, incoming solar radiation) is not supported by a strong physical or chemical interpretation. Considering also the low adjusted regression coefficient R^2, this study assigns a low overall quality to this formula (see their Table 5). Nevertheless, the approach is considered a suitable solution to approximate the spatial and temporal variability of non-CO_2 effects of aviation, as part of the resolution of optimization problems. In fact, because of their low computational cost, the aCCFs are efficiently computed based on the local atmospheric fields, while solving aircraft trajectories optimizations. This is a great advantage compared to the CCFs, which are only available for a limited number of emission times and locations. Of course, since the aCCFs are rough approximations of highly non-linear processes, it is important to take into account their limitations.

First of all, the aCCFs 1.0 derive from datasets having specific spatio-temporal domains (North Atlantic, winter and/or summer days). As discussed in Chapter 3.4, these prototype formulas are employed out of design outside this domain, and are not suitable for applications under different atmospheric dynamics, e.g. at tropical latitudes. More details about this limitation, and on-going work addressing it, are available in Chapter 3.4. Moreover, all the available data was used for the derivation of the aCCFs 1.0 formulas, as well as for the calculation of the adjusted regression coefficient R^2. However, only distinguishing training and test datasets would enable to measure the ability of the model to handle *new* data within the domains of the training data (e.g. North Atlantic region, winter season). A recent study (Rao et al., 2024) presented a new approach for the derivation of aCCFs, and included the distinction between training and test data.

Lastly, the aCCFs 1.0 provide a set of deterministic values, representing the climate impact of contrails, NO_x, H_2O, and CO_2, in terms of Average Temperature Response over 20 years (ATR20). These values are affected by uncertainties (related to modelling, scientific understanding, natural variability, etc.), which are not quantified using the aCCFs 1.0. As a result, the probability of achieving the predicted reduction in ATR20 via aircraft trajectory optimization cannot be estimated. This gap is addressed by Rao et al. (2024), and on-going research is working towards a new set of aCCFs that includes uncertainty quantifications (more information is available at the F4EClim project webpage, https://www.f4eclim.eu/, last accessed on 16 July 2025).

Another prototype tool that can be incorporated in the calculation of optimized aircraft trajectories is CocipGrid, an extension of the trajectory-based contrail cirrus prediction model CoCiP (Schumann et al., 2012; Engberg et al., 2025). This approach uses a Lagrangian model to simulate the evolution of a contrail segment during its lifetime. It results in the generation of four-dimensional global maps of contrails climate impact, measured in terms of contrail energy forcing. Therefore, the robustness of contrail avoidance can be increased by comparing aircraft trajectories optimized based on different models. More fast-assessment tools estimating the climate impact of NO_x emissions are necessary in order to perform inter-model comparisons in future studies.

In this thesis, the functionality of the developed modelling chain has been showcased using the prototype set of aCCFs 1.0 (Chapter 4). The relative importance of the different species was calibrated using the AirClim model (aCCFs 1.0A, Matthes et al., 2023). The results presented in this case study are in agreement with previous literature (Grewe et al., 2017b). Further developments of the approach used for the evaluation of non-CO_2 effects are recommended, particularly to (1) quantify uncertainties affecting the best estimates, and (2) include a wider range of scenarios in the training data (seasons, geographic regions, alternative fuels and new technologies). Because of its modularity, the modelling chain presented here is readily adaptable to include future approaches, e.g. new aCCFs versions.

To conclude, the aCCFs formula are, as described above, simplifications of highly complex atmospheric processes. Therefore, they cannot fully capture the spatio-temporal variability of the climate impact of aircraft emissions. Nevertheless, the question is if the aCCFs are effective objective functions for aircraft trajectory optimization, i.e., if minimizing their values along the aircraft trajectories leads to a reduction in the radiative forcing from aviation non-CO_2 effects. This has been successfully tested by Rao

et al. (2022) for the case of the NO_x-ozone aCCF (see Chapter 3.4.3). In Chapter 6, this formula has been used to analyse the variability of aircraft trajectories minimizing operating costs and the climate impact of NO_x emissions, over multiple years. This methodology allows to investigate the potential benefits and penalties of the systematic application of different trajectory optimization strategies over long periods of time, thus improving the understanding of the relation between NO_x-climate effects and aircraft trajectory optimization. Moreover, this work provides new information and opportunities to compare the simulated climate impact from aviation NO_x emissions across different studies, using independent approaches.

7.2 Multi-objective optimization of aircraft trajectories

The development of an approach to identify eco-efficient aircraft trajectories is among the main objectives of this thesis (Chapter 1). A decision making tool, SolFinder 1.0, has been introduced in Chapter 4 to tackle this point, and it is currently available as part of the EMAC submodel AirTraf (AirTraf 3.0). By employing this modelling chain, air traffic samples are optimized every day over long periods of time (~3 years, see Chapters 5-6), based on the local atmospheric conditions at the time of departure, with a high temporal resolution (12 minutes). In the following paragraphs, the main limitations of the approach employed to optimize the air traffic samples are considered.

First of all, the flights included in the air traffic sample are optimized individually, neglecting potential conflicts and other network effects. This has the advantage of reducing the complexity of the problem at hand. When assessing the mitigation potential of optimized trajectories, the average single-flight contribution across the air traffic sample is usually computed, as commonly done in the literature (Simorgh et al., 2022). However, this mitigation potential might be lower in reality, due to airspace structure and network effects. Moreover, non-linearities in the total climate impact of multiple flights are not taken into account. For example, what is the cumulative effect of contrails formed by consecutive flights is still an open research question.

Another point to take into account is that the benefit and penalties are calculated with respect to a reference scenario (fuel- or cost-optimal trajectories), which differs from the one that is actually flown. As a result, win-win situations might emerge, in which both fuel (and thus CO_2 emissions) and non-CO_2 effects are reduced, when comparing the currently implemented routing strategy, and potential eco-efficient aircraft trajectories (Niklaß et al., 2021).

Lastly, the definition of what is considered as an eco-efficient trajectory is ultimately dependent on political and economic considerations. The decision-making tool introduced in Chapter 4 (SolFinder 1.0) includes a strategy based on the VIKOR method, which offers the possibility of varying the relative weight of the optimization objectives (w), and the preference towards a higher overall benefit or towards limiting large penalties in one of the objectives (γ). Therefore, different outcomes resulting from a range of preferences can be compared using this tool. Ultimately, the user is responsible for providing the higher-level information necessary to guide the selection, by setting the VIKOR parameters w and γ.

7.3 Trade-offs between reducing CO_2 and non-CO_2 effects

This thesis contributes to on-going efforts aiming at reducing the climate impact of aviation. As described in Chapter 2, aircraft emissions perturb the climate system via several processes, usually distinguished between CO_2 and non-CO_2 effects. The latter include the impacts from the formation of persistent contrails, and NO_x emissions. This thesis focuses on the possibility of optimizing aircraft trajectories to reduce of the overall climate impact of aviation, taking advantage of the spatio-temporal dependency of non-CO_2 effects (contrails, NO_x, H_2O). Therefore, this works relies on the assumption that a net reduction in the climate impact is achieved by reducing the magnitude of non-CO_2 effects, at the cost of a small increase in fuel consumption. However, extra fuel use results not only in higher operating costs, but also higher CO_2 emissions. The latter disadvantage is particularly relevant, as the goal of this operational strategy is the reduction of the overall aviation climate impact. Weighting the trade-offs between the reduction of CO_2 and non-CO_2 effects is not straightforward, due to the following key points:

- The species emitted by the aircraft, and the atmospheric perturbations that they cause, have very different residence times in the atmosphere. Persistent contrails vanish a few hours after their formation, while a fraction of the emitted CO_2 remains in the atmosphere for millennia (Chapter 2). Therefore, the trade-offs between the reduction of CO_2 and non-CO_2 effects of aviation are highly dependent on the **time horizon** (20 or 100 years, or longer) and on the underlying **emission scenario** chosen for their evaluation (Chapter 2).
- The interactions between non-CO_2 species and the local environment are governed by complex physical and chemical processes, operating over a wide range of spatio-temporal scales (Chapter 2). As a result, measuring and simulating these processes is challenging, thus their confidence levels remain medium, low, or very low (Lee et al., 2021). The opposite is true for CO_2 emissions: their impact on the climate is well-understood and relatively easy to simulate, as the radiative forcing is simply dependent on the amount of emitted CO_2. This hinders the evaluation of trade-offs between different effects, as it is uncertain if the overall effective radiative forcing (ERF) of contrails and NO_x emissions is much larger or much smaller than the ERF of CO_2 (Chapter 2).

Trade-offs between the reduction of CO_2 and non-CO_2 effects characterize not only aircraft trajectory optimization, but also several other climate impact mitigation strategies (Lee et al., 2023; Prather et al., 2025). For example, CO_2 emissions are reduced at the cost of increasing NO_x emissions, when improvements in fuel efficiency are achieved via higher engine pressure ratios and turbine entry temperatures. Another case is represented by the removal of aromatic compounds from kerosene fuels, which would require higher CO_2 emissions from fuel refinery operations, to achieve reductions in soot emissions and, possibly, in the climate impact of contrails. In some instances, win-win situations are possible. Water ingestion can be exploited to lower combustion temperatures, thus decreasing NO_x emissions, while increasing fuel efficiency.

Moreover, using sustainable aviation fuels (SAF), both CO_2 and soot emissions would be reduced, with potential indirect benefits in terms of lower contrail climate impact.

To conclude, weighting the relative importance of different aviation effects is a critical point for the assessment of most climate impact mitigation strategies. The authors of Lee et al. (2023) addressed such critical point, concluding that better quantifications of aviations effects must be available before "recommending definitive courses of action". This point is particularly relevant for the development of new propulsive technologies and aircraft design, which take decades of work and considerable investments. From this point of view, operational strategies entail lower risks, as they are applicable using the current fleet and can be adapted over time, as soon as new knowledge is available.

As long as global air traffic grows, the climate impact of short-term non-CO_2 effects remains a serious threat in the near future. In this time-frame, reducing anthropogenic global warming is crucial to avoid reaching *"tipping-points"* of the climate system, i.e., critical thresholds after which the initial perturbations from human activities are amplified by natural processes, and their impact become irreversible. *The only strategy that guarantees a prompt reduction in aviation climate impact includes a decrease in the air traffic.* As projections for the next decades promise the opposite scenario, closing the gap between the scientific understanding of CO_2 and non-CO_2 effects is a current priority, in order to achieve sustainability in the aviation sector.

8

Conclusions

"...e si mettono lì tra noi e il cielo
per lasciarci soltanto una voglia di pioggia."
Fabrizio De Andrè

Eco-efficient aircraft trajectories are defined as routes that significantly reduce aviation climate effects with small economic penalties, when compared to cost-optimal flights. In the different chapters of this thesis, this concept is explored, to provide new insights into the climate impact mitigation potential of optimized aircraft trajectories. Here, the key contributions of this doctoral project are highlighted, illustrating how it addresses the research questions presented in Chapter 1.

Q1: How can we identify eco-efficient aircraft trajectories?

This question has been the focus of the first part of the doctoral project, that resulted in the development of a decision-making tool, SolFinder 1.0, and its implementation within the air traffic optimizer AirTraf 3.0. This model development is described in details in **Chapter 4**. Here, the main characteristics of the modelling chain are highlighted, referring to the case study described in Section 4.4 to showcase its functionality.

Considering the definition of *eco-efficient* aircraft trajectories, their identification implies the resolution of multi-objective optimization problems, simultaneously minimizing objective functions that represent economic costs and climate effects of the flight. If these objective are conflicting, several optimal solutions can be found, as increments in one objective allow reductions in the other. This set of optimal solutions is called *Pareto-optimal set*. To select a single option among these optimal alternatives, higher-level information is necessary, such as preferences of the decision maker. The SolFinder module collects various strategies that take these preferences into account, in order to pick an individual solution.

SolFinder 1.0 satisfies three main requirements. First of all, it is applicable to any Pareto-optimal set resulting from the multi-objective optimization of an individual

aircraft trajectory, e.g., convex or concave Pareto fronts, single solution (when no trade-offs between the objectives are identified), etc. Moreover, SolFinder 1.0 identifies the preferred compromise solution of multi-objective optimization problems, minimizing any number of objective functions (two, in the case of bi-objective optimizations, or more). In particular, when employed to the Pareto-set resulting from the bi-objective optimization of operating cost and climate impact, it is capable of identifying eco-efficient solutions. This last requirement ensures that SolFinder 1.0 is a suitable tool to address the first research question of this thesis.

The following strategies are available in SolFinder 1.0:

- a decision-making strategy based on the VIKOR method (Opricovic et al., 2004), translating the preferences of the decision maker in mathematical terms, using weights measuring the relative importance of the objectives (w) and of group utility versus individual regret (γ);
- an option that selects the Pareto-optimal solution closest to a target percentage change in one of the objectives (e.g., +1% increase in fuel use);
- a strategy combining the previous two, by setting a limit in the percentage change in one of the objectives (e.g., operating costs) after the the decision-making method based on the VIKOR method is applied;
- a simple option that picks one of the extreme points in the Pareto-set (e.g., minimal climate effects from NO_x emissions).

All these strategies are applied in the case study presented in Section 4.4. Here, a European air traffic sample including 100 night-time flights is optimized under the atmospheric conditions computed by the EMAC model (see Chapter 3) during a 1-month simulation (1-31 January 2018). Through this example application of SolFinder, the effectiveness of the tool in identifying eco-efficient trajectories is illustrated. In fact, the strategy based on the VIKOR method achieves higher benefit over penalties ratios than a simple option aiming for a target percentage change in the objective (Figure 4.9). Note that choosing the values of the VIKOR parameters w and γ remains an arbitrary choice, as explained in Chapter 4 and Chapter 7. Therefore, the decision-maker is required to evaluate the variability of the solutions with varying w and γ (e.g., comparing the achieved changes in contrails, NO_x, and CO_2) and determine what can be considered a truly eco-efficient solution.

To conclude, SolFinder was found to be a suitable tool to identify eco-efficient trajectories via its implementation in AirTraf 3.0, completing the development of this air traffic optimizer for the resolution of multi-objective optimization problems.

Subsequently, this modelling chain has been employed to address the other research questions of this thesis, as described in the following paragraphs.

Q2: How do optimized aircraft trajectories change over the range of atmospheric natural variability?

To answer this question, we conduct multi-annual simulations with the EMAC model, including its submodels AirTraf, CONTRAIL, and ACCF (see Chapter 3). The results of these simulations are presented in **Chapter 5** and **Chapter 6**. The former focused on the variability of contrail avoidance, while the latter analysed trajectories minimizing the climate impact of NO_x emissions. The same air traffic sample is optimized in the two cases, including 100 North Atlantic flights with departure times distributed throughout the day. In both Chapters, strong seasonalities in the properties of optimized trajectories emerge.

Particularly evident is the seasonal cycle of the mean flight altitudes minimizing contrail formation and climate impact of NO_x emissions. This seasonality is driven by the variability of the climatological tropopause height over the region (North Atlantic), determining the location of the strongest vertical gradients in both persistent contrail formation and climate impact of NO_x emissions. Contrarily, mean flight altitudes in the reference scenarios remain approximately constant throughout the simulated years. In fact, these scenarios are driven by the minimization of fuel consumption, thus aircraft fly close to the highest available flight level, to reduce aerodynamic drag.

Another key finding is that the potential of mitigating the climate impact of NO_x emissions via optimal trajectories varies strongly during the year. In fact, the difference in $ATR20_{NOx}$ (Average Temperature Response over 20 years) between NO_x-climate optimal trajectories and the reference scenario reaches a maximum in winter. In summer, when $ATR20_{NOx}$ peaks due to the more active photochemistry, there is a much smaller difference in the $ATR20_{NOx}$ of the two scenarios (Figure 6.5). This is reflected in the strong variability in the shape and extension of the Pareto fronts, illustrating the trade-offs between the reduction of climate effects from NO_x emissions and operating costs (Figure 6.6). Therefore, this analysis suggests that eco-efficient trajectories tackling the climate impact of NO_x emissions would be mostly beneficial in winter, while it may not be an advantageous strategy in summer. Limitations of this analysis are associated with the estimation of the $ATR20_{NOx}$ patterns and values, and the assessment of the trade-offs with higher CO_2 emissions, as discussed in Chapter 7.

Q3: Are eco-efficient aircraft trajectories more beneficial under specific weather patterns?

Yes, some weather conditions are found to allow higher benefits at lower economic costs, considering the results presented in **Chapter 5**.

This variability is analysed by comparing the trade-offs between contrail avoidance and optimal fuel use, under different typical weather patterns occurring over the North Atlantic during winter. To distinguish the weather patterns, a well-established classification methods is employed, which is based on the similarity between the daily geopotential anomalies with those defining the North Atlantic Oscillation (NAO) and East Atlantic (EA) patterns (Irvine et al., 2013). This analysis suggests that weather conditions resembling the negative phase of the EA pattern are associated with higher reductions in persistent contrail formation via aircraft trajectory optimization (i.e., winter weather type 3, labelled as “W3”). Under W3 days, the jet stream tends to be weaker and titled, reaching latitudes further north than in other days. This results in a

higher average tropopause height and, subsequently, in a higher likelihood of forming persistent contrails at typical flight levels. Contrarily, a minimal average contrail formation in the reference scenario (fuel-optimal) and reduction achieved via contrail avoidance is found under the opposite pattern (W1), linked to a strong and zonally oriented jet stream. These findings are supported by the comparison between the potential contrail coverage computed by the EMAC submodel CONTRAIL and IAGOS observations (Figure 5.9). The relationship between penalties and benefits (eco-efficiency) shows a clear dependency with weather conditions, as illustrated by the comparison of Pareto fronts averaged under different weather classes (Figure 5.5).

Q4: How are different climate effects of aviation reduced by eco-efficient aircraft trajectories?

In this thesis, we found specific points distinguishing the reductions in different non-CO_2 effects (persistent contrails and NO_x emissions), that were achieved by changing trajectory optimization strategies. Other characteristics are common to both effects. Here, we list these key points:

- If only small increases in fuel used (and, therefore, CO_2 emissions) are allowed, eco-efficient trajectories take advantage of contrail avoidance to reduce the average temperature response over 20 years (Chapter 4).
- When larger penalties in operating costs are accepted, the air traffic optimizer identifies solutions that also reduce the climate impact of NO_x, at the cost of extra CO_2 emissions (Chapter 4).
- Compared to a reference scenario driven by the reduction of fuel consumption, trajectories avoiding persistent contrail formation or large climate impact from NO_x emissions tend to fly at lower altitudes (Chapters 5-6).
- Over the North Atlantic, the mean flight altitudes of trajectories reducing non-CO_2 effects of aviation follow a seasonal cycle. In the case of contrail avoidance, the minimal mean altitude is reached in summer, with a large variability over the air traffic sample (Chapter 5). Contrarily, NO_x-climate optimal trajectories fly at the lowest mean altitudes in winter, with small differences between different flights (Chapter 6).
- Reduction of non-CO_2 effects is obtained at lower fuel penalties via changes in flight altitude, but lateral shifts are also observed in extreme scenarios. Changes in lateral path leading to contrail avoidance show different trends depending on the local weather conditions, driven by the location of the jet stream (Chapter 5). NO_x-climate optimal trajectories tend to fly more northward than cost-optimal trajectories, to limit transport of the emitted species to lower latitudes (Chapter 6).
- Compromise solutions between extreme scenarios (e.g., minimizing fuel and contrails formed along the trajectory) ensure higher benefit per unit of extra fuel (Chapters 4-5-6).

- The shape and extension of the Pareto fronts comparing different routing strategies show large variability under different seasons and weather patterns (Chapters 4-5-6).

To conclude, the analyses presented in this thesis highlight the importance of improving the scientific understanding of the processes determining aviation climate impact. In fact, these results suggest the existence of trade-offs between the reduction of different climate impact effects via operational strategies, when benefits and penalties are computed with respect to fuel-optimal solutions. Collecting observational data to validate and improve the current models is crucial, in order to narrow the gap between the confidence levels in the estimated temperature response from CO_2 and non-CO_2 effects.

A

Appendix A: Supplementary material on SolFinder v1.0

Additional information on SolFinder v1.0 (described in Chapter 4) is provided in this appendix, based on the supplement material accompanying Castino, F., Yin, F., Grewe, V., Yamashita, H., Matthes, S., Dietmüller, S., Baumann, S., Soler, M., Simorgh, A., Mendiguchia Meuser, M., Linke, F., and Lührs, B., Decision-making strategies implemented in SolFinder 1.0 to identify eco-efficient aircraft trajectories: application study in AirTraf 3.0, Geoscientific Model Development 17(9), 4031–4052, DOI: 10.5194/gmd-17-4031-2024, 2024.

A

A.1 Background information

SolFinder library to find a solution among a set of Pareto optimal solutions, according to the preferences of the decision-maker. This library has been developed with the aim of identifying eco-efficient aircraft trajectories. The following options are available:

- option selecting a solution closest to a target change in one of the objectives
- Gray Relational Analysis (GRA, Wang et al., 2017)
- Technique for Order of Preference by Similarity to Ideal Solution (TOPSIS, Wang et al., 2017; Chen et al., 1992)
- Viekriterijumsko Kompromisno Rangiranje (VIKOR, Wang et al., 2017; Opricovic et al., 2004) method.

License: SolFinder is released under GNU Lesser General Public License v3.0 (LGPL-3.0-or-later).

© 2023 Federica Castino

A.2 Installation

```
pip install solfinder
```

A.3 Get started

```
import solfinder.MCDM as MCDM
import numpy as np

# Upload example dataset
with open(r'tests/Data_example/POBJ_20180101000005_0_51_28_41.dat', 'r') as f:
    data = np.loadtxt(f, unpack=True)

# Values of objective functions
soc = data[0] # Simple Operating Costs
atr = data[1] # ATR20 total

# Find Pareto optimal solutions using available options
index_target_05 = MCDM.Target.solution_found_with_target(MCDM.Target(),0.5,soc)
index_gra       = MCDM.GRA.solution_found_by_gra(MCDM.GRA(), data)
index_topsis    = MCDM.TOPSIS.solution_found_by_topsis(MCDM.TOPSIS(),
                  data, [0.5,0.5])
set_indices_vikor, index_vikor = MCDM.VIKOR.solution_found_by_vikor(MCDM.VIKOR(),
                                 data, 0.5, [0.5, 0.5])
```

A.4 Example application

```
import solfinder.MCDM as MCDM
import numpy as np
import matplotlib.pyplot as plt

# Upload example dataset
with open(r'tests/Data_example/POBJ_20180101000005_0_51_28_41.dat', 'r') as f:
    data = np.loadtxt(f, unpack=True)

# Values of objective functions
soc = data[0]
atr = data[1]

# Number of Pareto optimal solutions
n_sol = len(soc)

# Find Pareto optimal solutions using available options
index_target_05 = MCDM.Target.solution_found_with_target(MCDM.Target(),0.5,soc)
index_gra       = MCDM.GRA.solution_found_by_gra(MCDM.GRA(), data)
index_topsis    = MCDM.TOPSIS.solution_found_by_topsis(MCDM.TOPSIS(),
                  data, [0.5,0.5])
set_indices_vikor, index_vikor = MCDM.VIKOR.solution_found_by_vikor(MCDM.VIKOR(),
                                 data, 0.5, [0.5, 0.5])

# Plot of Pareto front and selected solutions
plt.scatter(100 * (atr - max(atr)) / max(atr),
            MCDM.Target.rel_change(soc), s=20, c='grey')
plt.scatter(100 * (atr[index_target_05] - max(atr)) / max(atr),
            100 * (soc[index_target_05] - min(soc)) / min(soc),
            s=40, c='red', label='Target +0.5% SOC')
plt.scatter(100 * (atr[index_gra] - max(atr)) / max(atr),
            100 * (soc[index_gra] - min(soc)) / min(soc),
            s=40, c='blue', label='GRA')
plt.scatter(100 * (atr[index_topsis] - max(atr)) / max(atr),
            100 * (soc[index_topsis] - min(soc)) / min(soc),
            s=40, c='orange', label='TOPSIS')
plt.scatter(100 * (atr[index_vikor] - max(atr)) / max(atr),
            100 * (soc[index_vikor] - min(soc)) / min(soc),
            s=40, c='green', label='VIKOR')
plt.xlabel(r'Change in ATR20 [%]', fontsize=16, labelpad=15)
plt.ylabel(r'Change in SOC [%]', fontsize=16, labelpad=15)
plt.title('Number of solutions: {}'.format(n_sol))
plt.legend()
plt.grid(True)
plt.show()
```

A

Output:

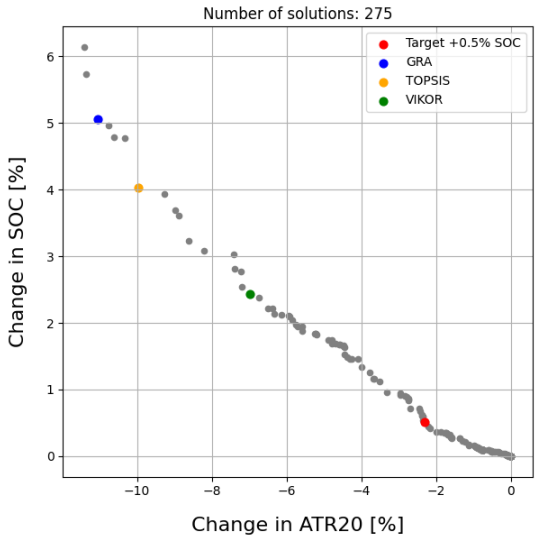


Figure A.1: Output of example application code.

B

Appendix B: Supplementary material on the analysis of contrail avoidance mitigation potential and its dependency on weather patterns

This appendix provides additional information on the analysis presented in Chapter 5, based on the supplement material accompanying Castino, F., Grewe, V., Yamashita, H., Hildebrandt, K.G., Yin, F., *Seasonal variability and weather pattern dependency of contrail avoidance in the North Atlantic,* submitted.

B

B.1 Comparison of weather pattern type frequencies

Considering the yearly variability, the frequencies of occurrence of the five weather pattern classes agree with those obtained in previous studies, as shown in Table B.1. The largest discrepancy is found with the frequency of W1. Note that different sources of atmospheric fields are used by each study, as Irvine et al., 2013 applied the weather pattern classification to ERA-Interim data, while Yamashita et al., 2021 analysed the result of EMAC simulations, nudged towards ERA-Interim data. Here, we employed the EMAC model, nudged towards ERA5 (see Section 5.2.1).

Study	**Period**	**Days in DJF)**				
		W1	W2	W3	W4	W5
Irvine et al., 2013	Jun. 1989-Feb. 2010	17	17	15	15	26
Yamashita et al., 2021	Dec. 2008–Aug. 2018	15	18	19	17	22
This study	Dec. 2015-Mar. 2018	8	18	21	12	32

Table B.1: Comparison of the frequency in the occurrence of the five weather pattern classes obtained in this study with previous studies (Irvine et al., 2013; Yamashita et al., 2021) during the meteorological winter (December, January, February).

B.2 Seasonality of potential contrail coverage over Europe

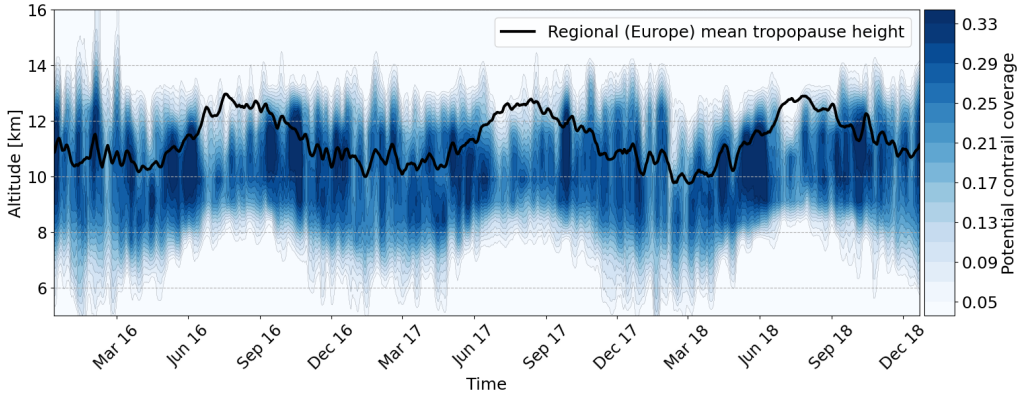


Figure B.1: Temporal and vertical variation of the average potential contrail coverage over Europe. Black line: regional mean tropopause height. A 7-day running average is applied.

B.3 Weather pattern analysis over the meteorological winter, DJF (December, January, February)

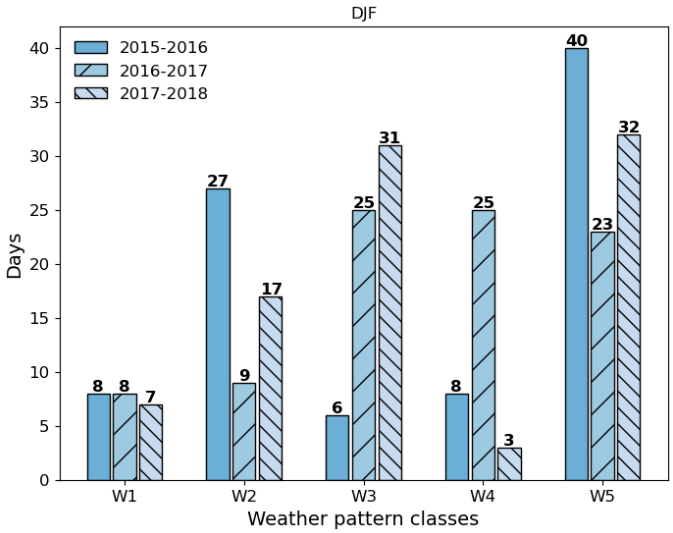


Figure B.2: Occurrence frequency of each winter weather pattern class, comparing the three winter seasons (December, January, and February of 2015-2016, 2016-2017, and 2017-2018).

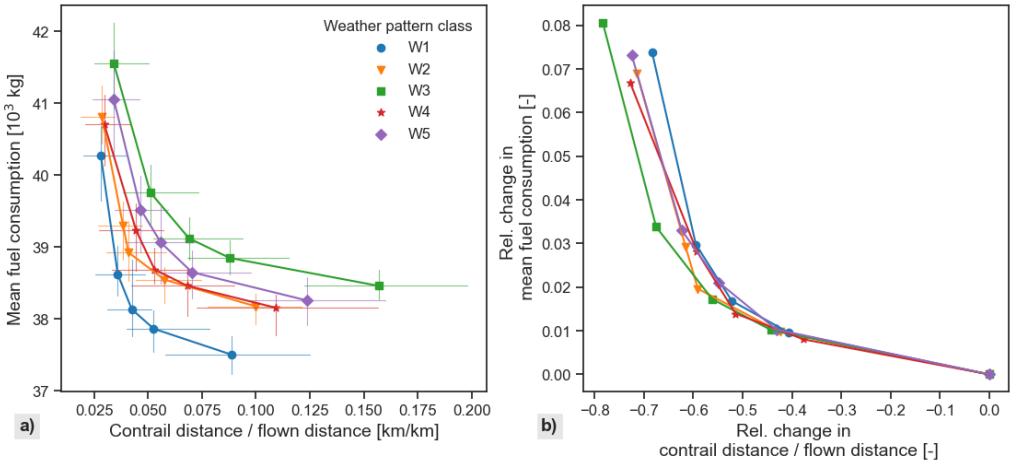


Figure B.3: As Figure 5, but relative to DJF: Comparison of the Pareto fronts obtained under different winter weather pattern classes, in terms of absolute values of the objective functions (a) and in terms of relative changes with respect to the *fuel-optimal* solution (b), averaging over the air traffic sample. The curves connect the median values over time of the different optimization strategies (*fuel-optimal*, *contrail-optimal*, and three trade-off solutions). Panel a: segments indicate the daily variability in both objectives along the Pareto fronts, extending from the first to the third quartile.

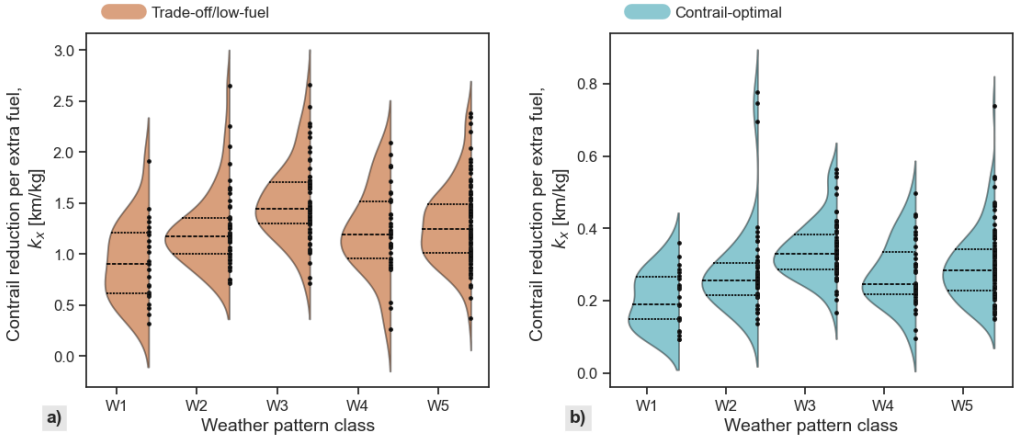


Figure B.4: As Figure 6, but relative to DJF: Distributions of k_x obtained over the simulated days, grouped by weather pattern class. Two trajectory optimization strategies are compared: trade-off solution strongly limiting fuel penalties ($w_{\text{fuel}} = 0.75$, panel a) and the extreme solution minimizing contrail distance (panel b). The dashed lines indicate quartiles, while the dots represent individual k_x values. Note that four outlier values are removed from the plot.

B.4 Vertical profiles of potential contrail coverage under different weather pattern classes

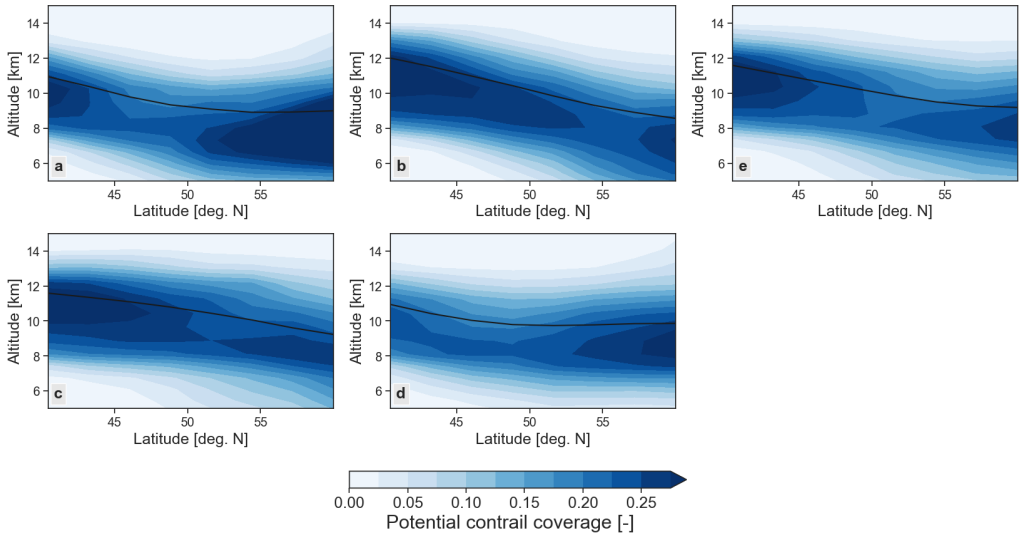


Figure B.5: Vertical section of potential contrail coverage (*potcov*) over the North Atlantic. Each panel (a-e) shows *potcov* and regional mean tropopause height averaged over all days within a weather class (W1-W5, respectively).

B.5 Vertical profiles of IAGOS data

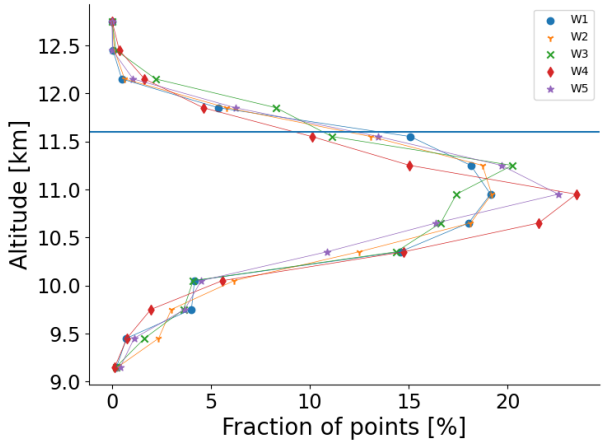


Figure B.6: Comparison of vertical profiles of IAGOS data used in this study under different winter weather types. The horizontal blue line indicates the mean altitude of *fuel-optimal* trajectories, used as reference scenario in this study.

Bibliography

Appleman, H. (1953). "The formation of exhaust condensation trails by jet aircraft". In: *Bulletin of the American Meteorological Society* 34.1, pp. 14–20.

Archer, C. L. and Caldeira, K. (2008). "Historical trends in the jet streams". In: *Geophysical Research Letters* 35.8. ISSN: 00948276. DOI: 10.1029/2008GL033614.

Barnston, A. and Livezey, R. (1987). "Classification, seasonality and persistence of low-frequency atmospheric circulation patterns." In: *Mon. Weather Rev.* 115, pp. 1083–1126.

Burkhardt, U., Bock, L., and Bier, A. (2018). "Mitigating the contrail cirrus climate impact by reducing aircraft soot number emissions". In: *Climate and Atmospheric Science* 1.1, p. 37. ISSN: 2397-3722. DOI: 10.1038/s41612-018-0046-4.

Burkhardt, U., Kärcher, B., Ponater, M., Gierens, K., and Gettelman, A. (2008). "Contrail cirrus supporting areas in model and observations". In: *Geophysical Research Letters* 35.16. ISSN: 0094-8276. DOI: 10.1029/2008GL034056.

Burris, M. A. (2015). "Cost index estimation". In: *IATA 3rd Airline Cost Conference, Geneva, Switzerland*, pp. 1–23.

Castino, F., Yin, F., Grewe, V., Soler, M., Simorgh, A., Yamashita, H., Matthes, S., Baumann, S., Dietmüller, S., Linke, F., and Lührs, B. (2021). "Seasonal Variability of Aircraft Trajectories reducing NOx-climate Impacts under a Multitude of Weather Patterns". In: *11th SESAR Innovation Days*.

Castino, F. (2023). "Code accompanying the manuscript "Decision-Making strategies implemented in SolFinder 1.0 to identify eco-efficient aircraft trajectories: application study in AirTraf 3.0"". In: *4TU.ResearchData*. DOI: 10.4121/3744b922-ffa6-4f92-ad57-dc93f94e969b.

Castino, F., Yin, F., Grewe, V., Yamashita, H., Matthes, S., Dietmüller, S., Baumann, S., Soler, M., Simorgh, A., Mendiguchia Meuser, M., Linke, F., and Lührs, B. (2024). "Decision-making strategies implemented in SolFinder 1.0 to identify eco-efficient aircraft trajectories: application study in AirTraf 3.0". In: *Geoscientific Model Development* 17.9, pp. 4031–4052. ISSN: 1991-9603. DOI: 10.5194/gmd-17-4031-2024.

Celis, C., Sethi, V., Zammit-Mangion, D., Singh, R., and P. Pilidis, P. (2014). "Theoretical Optimal Trajectories for Reducing the Environmental Impact of Commercial Aircraft

Operations". In: *Journal of Aerospace Technology and Management* 6.1, pp. 29–42. ISSN: 2175-9146. DOI: 10.5028/jatm.v6i1.288.

Chahine, M. T. (1992). "The hydrological cycle and its influence on climate". In: *Nature* 359.6394, pp. 373–380. ISSN: 0028-0836. DOI: 10.1038/359373a0.

Chen, N. Y., Sridhar, B., Ng, H., and Li, J. (2014). "Evaluating Tradeoff between Environmental Impact and Operational Costs for Enroute Air Traffic". In: *AIAA Guidance, Navigation, and Control Conference*. Reston, Virginia: American Institute of Aeronautics and Astronautics. ISBN: 978-1-62410-317-9. DOI: 10.2514/6.2014-1464.

Chen, S.-J. and Hwang, C.-L. (1992). *Fuzzy Multiple Attribute Decision Making*. Vol. 375. Berlin, Heidelberg: Springer Berlin Heidelberg. ISBN: 978-3-540-54998-7. DOI: 10.1007/978-3-642-46768-4.

Cook, A., Tanner, G., Williams, V., and Meise, G. (2009). "Dynamic cost indexing – Managing airline delay costs". In: *Journal of Air Transport Management* 15.1, pp. 26–35. ISSN: 09696997. DOI: 10.1016/j.jairtraman.2008.07.001.

Crutzen, P. J. (1979). "The Role of NO and NO2 in the Chemistry of the Troposphere and Stratosphere". In: *Annual Review of Earth and Planetary Sciences* 7.1, pp. 443–472. ISSN: 0084-6597. DOI: 10.1146/annurev.ea.07.050179.002303.

Dahlmann, K., Grewe, V., Frömming, C., and Burkhardt, U. (2016). "Can we reliably assess climate mitigation options for air traffic scenarios despite large uncertainties in atmospheric processes?" In: *Transportation Research Part D: Transport and Environment* 46, pp. 40–55. ISSN: 13619209. DOI: 10.1016/j.trd.2016.03.006.

Dee, D. P., Uppala, S. M., Simmons, A. J., Berrisford, P., Poli, P., Kobayashi, S., Andrae, U., Balmaseda, M. A., Balsamo, G., Bauer, P., Bechtold, P., Beljaars, A. C. M., Berg, L. van de, Bidlot, J., Bormann, N., Delsol, C., Dragani, R., Fuentes, M., Geer, A. J., Haimberger, L., Healy, S. B., Hersbach, H., Hólm, E. V., Isaksen, L., Kållberg, P., Köhler, M., Matricardi, M., McNally, A. P., Monge-Sanz, B. M., Morcrette, J.-J., Park, B.-K., Peubey, C., Rosnay, P. de, Tavolato, C., Thépaut, J.-N., and Vitart, F. (2011). "The ERA-Interim reanalysis: configuration and performance of the data assimilation system". In: *Quarterly Journal of the Royal Meteorological Society* 137.656, pp. 553–597. ISSN: 00359009. DOI: 10.1002/qj.828.

Dietmüller, S., Jöckel, P., Tost, H., Kunze, M., Gellhorn, C., Brinkop, S., Frömming, C., Ponater, M., Steil, B., Lauer, A., and Hendricks, J. (2016). "A new radiation infrastructure for the Modular Earth Submodel System (MESSy, based on version 2.51)". In: *Geoscientific Model Development* 9.6, pp. 2209–2222. ISSN: 1991-9603. DOI: 10.5194/gmd-9-2209-2016.

Dietmüller, S., Matthes, S., Dahlmann, K., Yamashita, H., Simorgh, A., Soler, M., Linke, F., Lührs, B., Meuser, M. M., Weder, C., Grewe, V., Yin, F., and Castino, F. (2023). "A Python library for computing individual and merged non-CO2 algorithmic climate change functions: CLIMaCCF V1.0". In: *Geoscientific Model Development* 16.15, pp. 4405–4425. ISSN: 1991-9603. DOI: 10.5194/gmd-16-4405-2023.

Dong, B., Aksenov, Y., Colfescu, I., Harvey, B., Hirschi, J., Josey, S., Lu, H., Mecking, J., Oltmanns, M., Osprey, S., Robson, J., Rynders, S., Shaffrey, L., Sinha, B., Sutton, R., and Weisheimer, A. (2025). "Key drivers of large scale changes in North Atlantic atmospheric and oceanic circulations and their predictability". In: *Climate Dynamics* 63.2, p. 113. ISSN: 0930-7575. DOI: 10.1007/s00382-025-07591-1.

Engberg, Z., Teoh, R., Abbott, T., Dean, T., Stettler, M. E. J., and Shapiro, M. L. (2025). "Forecasting contrail climate forcing for flight planning and air traffic management applications: the CocipGrid model in pycontrails 0.51.0". In: *Geoscientific Model Development* 18.2, pp. 253–286. ISSN: 1991-9603. DOI: 10.5194/gmd-18-253-2025.

Eurocontrol (2011). *User Manual for the Base of Aircraft Data (BADA) Revision 3.9, EEC Technical/Scientific Report No.12/04/10-45.*

Fichter, C., Marquart, S., Sausen, R., and Lee, D. S. (2005). "The impact of cruise altitude on contrails and related radiative forcing". In: *Meteorologische Zeitschrift* 14.4, pp. 563–572. ISSN: 0941-2948. DOI: 10.1127/0941-2948/2005/0048.

Fonseca, C. and Fleming, P. (1993). "Genetic Algorithms for Multiobjective Optimization: Formulation, Discussion and Generalization." In: *Proceedings of the ICGA-93: Fifth International Conference on Genetic Algorithms.* San Mateo, pp. 416–423.

Frömming, C., Grewe, V., Brinkop, S., and Jöckel, P. (2014). "Documentation of the EMAC submodels AIRTRAC 1.0 and CONTRAIL 1.0, supplementary material of Grewe et al., 2014, 7, 175–201". In: *Geoscientific Model Development.*

Frömming, C., Ponater, M., Dahlmann, K., Grewe, V., Lee, D. S., and Sausen, R. (2012). "Aviation-induced radiative forcing and surface temperature change in dependency of the emission altitude". In: *Journal of Geophysical Research Atmospheres* 117.19, pp. 1–15. ISSN: 01480227. DOI: 10.1029/2012JD018204.

Frömming, C., Grewe, V., Brinkop, S., Jöckel, P., Haslerud, A. S., Rosanka, S., Van Manen, J., and Matthes, S. (2021). "Influence of weather situation on non-CO2 aviation climate effects: The REACT4C climate change functions". In: *Atmospheric Chemistry and Physics* 21.11, pp. 9151–9172. ISSN: 16807324. DOI: 10.5194/acp-21-9151-2021.

Gierens, K. and Spichtinger, P. (2000). "On the size distribution of ice-supersaturated regions in the upper troposphere and lowermost stratosphere". In: *Annales Geophysicae* 18.4, pp. 499–504. ISSN: 1432-0576. DOI: 10.1007/s00585-000-0499-7.

Gierens, K., Matthes, S., and Rohs, S. (2020). "How well can persistent contrails be predicted?" In: *Aerospace* 7.12, pp. 1–18. ISSN: 22264310. DOI: 10.3390/aerospace7120169.

Gierens, K. and Vázquez-Navarro, M. (2017). "Statistical analysis of contrail lifetimes from a satellite perspective". In: *Meteorologische Zeitschrift* 27.3, pp. 183–193. ISSN: 0941-2948. DOI: 10.1127/metz/2018/0888.

Gimeno, L., Eiras-Barca, J., Durán-Quesada, A. M., Dominguez, F., Ent, R. van der, Sodemann, H., Sánchez-Murillo, R., Nieto, R., and Kirchner, J. W. (2021). "The residence time of water vapour in the atmosphere". In: *Nature Reviews Earth & Environment* 2.8, pp. 558–569. ISSN: 2662-138X. DOI: 10.1038/s43017-021-00181-9.

Gössling, S. and Humpe, A. (2020). "The global scale, distribution and growth of aviation: Implications for climate change". In: *Global Environmental Change* 65, p. 102194. ISSN: 09593780. DOI: 10.1016/j.gloenvcha.2020.102194.

Grewe, V., Frömming, C., Matthes, S., Brinkop, S., Ponater, M., Dietmüller, S., Jöckel, P., Garny, H., Tsati, E., Dahlmann, K., Søvde, O. A., Fuglestvedt, J., Berntsen, T. K., Shine, K. P., Irvine, E. A., Champougny, T., and Hullah, P. (2014a). "Aircraft routing with minimal climate impact: The REACT4C climate cost function modelling approach (V1.0)". In: *Geoscientific Model Development* 7.1, pp. 175–201. ISSN: 1991959X. DOI: 10.5194/gmd-7-175-2014.

Grewe, V., Champougny, T., Matthes, S., Frömming, C., Brinkop, S., Søvde, O. A., Irvine, E. A., and Halscheidt, L. (2014b). "Reduction of the air traffic's contribution to climate change: A REACT4C case study". In: *Atmospheric Environment* 94, pp. 616–625. ISSN: 18732844. DOI: 10.1016/j.atmosenv.2014.05.059.

Grewe, V., Dahlmann, K., Flink, J., Frömming, C., Ghosh, R., Gierens, K., Heller, R., Hendricks, J., Jöckel, P., Kaufmann, S., Kölker, K., Linke, F., Luchkova, T., Lührs, B., Manen, J. v., Matthes, S., Minikin, A., Niklaß, M., Plohr, M., Righi, M., Rosanka, S., Schmitt, A., Schumann, U., Terekhov, I., Unterstrasser, S., Vázquez-Navarro, M., Voigt, C., Wicke, K., Yamashita, H., Zahn, A., and Ziereis, H. (2017a). "Mitigating the climate impact from aviation: Achievements and results of the DLR WeCare project". In: *Aerospace* 4.3. ISSN: 22264310. DOI: 10.3390/aerospace4030034.

Grewe, V., Dameris, M., Fichter, C., and Lee, D. S. (2002). "Impact of aircraft NOx emissions. Part 2: Effects of lowering the flight altitude". In: *Meteorologische Zeitschrift* 11.3, pp. 197–205. ISSN: 0941-2948. DOI: 10.1127/0941-2948/2002/0011-0197.

Grewe, V., Matthes, S., Frömming, C., Brinkop, S., Jöckel, P., Gierens, K., Champougny, T., Fuglestvedt, J., Haslerud, A., Irvine, E., and Shine, K. (2017b). "Feasibility of climate-optimized air traffic routing for trans-Atlantic flights". In: *Environmental Research Letters* 12.3. ISSN: 17489326. DOI: 10.1088/1748-9326/aa5ba0.

Hegglin, M. I., Fahey, D. W., McFarland, M., Montzka, S. A., and Nash, E. R. (2015). *Twenty questions and answers about the ozone layer : scientific assessment of ozone depletion*. World Meteorological Organization, p. 79. ISBN: 9789966076021.

Hersbach, H., Bell, B., Berrisford, P., Hirahara, S., Horányi, A., Muñoz-Sabater, J., Nicolas, J., Peubey, C., Radu, R., Schepers, D., Simmons, A., Soci, C., Abdalla, S., Abellan, X., Balsamo, G., Bechtold, P., Biavati, G., Bidlot, J., Bonavita, M., De Chiara, G., Dahlgren, P., Dee, D., Diamantakis, M., Dragani, R., Flemming, J., Forbes, R., Fuentes, M., Geer, A., Haimberger, L., Healy, S., Hogan, R. J., Hólm, E., Janisková, M., Keeley, S., Laloyaux, P., Lopez, P., Lupu, C., Radnoti, G., Rosnay, P. de, Rozum, I., Vamborg, F., Villaume, S., and Thépaut, J.-N. (2020). "The ERA5 global reanalysis". In: *Quarterly Journal of the Royal Meteorological Society* 146.730, pp. 1999–2049. ISSN: 0035-9009. DOI: 10.1002/qj.3803.

Heymsfield, A., Baumgardner, D., DeMott, P., Forster, P., Gierens, K., and Kärcher, B. (2010). "Contrail microphysics". In: *Bulletin of the American Meteorological Society* 91.4, pp. 465–472. ISSN: 00030007. DOI: 10.1175/2009BAMS2839.1.

Hildebrandt, K. G., Castino, F., Meijer, V., and Yin, F. (2025). "Variability of ice supersaturated regions at flight altitudes: evaluation of ERA5 reanalysis using IAGOS in situ measurements". In: *EGUsphere [preprint]*. DOI: 10.5194/egusphere-2025-3048.

Hofer, S., Gierens, K., and Rohs, S. (2024). "How well can persistent contrails be predicted? An update". In: *Atmospheric Chemistry and Physics* 24.13, pp. 7911–7925. ISSN: 1680-7324. DOI: 10.5194/acp-24-7911-2024.

Hurrell, J. W., Kushnir, Y., Ottersen, G., and Visbeck, M. (2003). "An overview of the North Atlantic Oscillation". In: pp. 1–35. DOI: 10.1029/134GM01.

Intergovernmental Panel on Climate Change (IPCC) (2023). "Short-lived Climate Forcers". In: *Climate Change 2021 – The Physical Science Basis*. Cambridge University Press, pp. 817–922. DOI: 10.1017/9781009157896.008.

International Air Transport Association (IATA) (2024). *Global Outlook for Air Transport Deep Change*. Tech. rep.

IPCC (2021). "Climate Change 2021: The Physical Science Basis. Contribution of Working Group I to the Sixth Assessment Report of the Intergovernmental Panel on Climate Change". In: *Cambridge University Press* In Press, p. 3949.

Irvine, E. A., Hoskins, B. J., and Shine, K. P. (2012). "The dependence of contrail formation on the weather pattern and altitude in the North Atlantic". In: *Geophysical Research Letters* 39.12. ISSN: 00948276. DOI: 10.1029/2012GL051909.

Irvine, E. A., Hoskins, B. J., and Shine, K. P. (2014a). "A Lagrangian analysis of ice-supersaturated air over the North Atlantic". In: *Journal of Geophysical Research: Atmospheres* 119.1, pp. 90–100. ISSN: 2169-897X. DOI: 10.1002/2013JD020251.

Irvine, E. A., Hoskins, B. J., and Shine, K. P. (2014b). "A simple framework for assessing the trade-off between the climate impact of aviation carbon dioxide emissions and contrails for a single flight". In: *Environmental Research Letters* 9.6. ISSN: 17489326. DOI: 10.1088/1748-9326/9/6/064021.

Irvine, E. A., Hoskins, B. J., Shine, K. P., Lunnon, R. W., and Froemming, C. (2013). "Characterizing North Atlantic weather patterns for climate-optimal aircraft routing". In: *Meteorological Applications* 20.1, pp. 80–93. ISSN: 13504827. DOI: 10.1002/met.1291.

Jackson, R. B., Saunois, M., Bousquet, P., Canadell, J. G., Poulter, B., Stavert, A. R., Bergamaschi, P., Niwa, Y., Segers, A., and Tsuruta, A. (2020). "Increasing anthropogenic methane emissions arise equally from agricultural and fossil fuel sources". In: *Environmental Research Letters* 15.7, p. 071002. ISSN: 1748-9326. DOI: 10.1088/1748-9326/ab9ed2.

Jöckel, P., Kerkweg, A., Pozzer, A., Sander, R., Tost, H., Riede, H., Baumgaertner, A., Gromov, S., and Kern, B. (2010). "Development cycle 2 of the Modular Earth Submodel System (MESSy2)". In: *Geoscientific Model Development* 3.2, pp. 717–752. ISSN: 1991959X. DOI: 10.5194/gmd-3-717-2010.

Jöckel, P., Tost, H., Pozzer, A., Brühl, C., Buchholz, J., Ganzeveld, L., Hoor, P., Kerkweg, A., Lawrence, M. G., Sander, R., Steil, B., Stiller, G., Tanarhte, M., Taraborrelli, D., Aardenne, J. van, and Lelieveld, J. (2006). "The atmospheric chemistry general circulation model ECHAM5/MESSy1: consistent simulation of ozone from the surface to the mesosphere". In: *Atmospheric Chemistry and Physics* 6.12, pp. 5067–5104. ISSN: 1680-7324. DOI: 10.5194/acp-6-5067-2006.

Jöckel, P., Tost, H., Pozzer, A., Kunze, M., Kirner, O., Brenninkmeijer, C. A. M., Brinkop, S., Cai, D. S., Dyroff, C., Eckstein, J., Frank, F., Garny, H., Gottschaldt, K.-D., Graf, P., Grewe, V., Kerkweg, A., Kern, B., Matthes, S., Mertens, M., Meul, S., Neumaier, M., Nützel, M., Oberländer-Hayn, S., Ruhnke, R., Runde, T., Sander, R., Scharffe, D., and Zahn, A. (2016). "Earth System Chemistry integrated Modelling (ESCiMo) with the Modular Earth Submodel System (MESSy) version 2.51". In: *Geoscientific Model Development* 9.3, pp. 1153–1200. ISSN: 1991-9603. DOI: 10.5194/gmd-9-1153-2016.

Kärcher, B. (2018). "Formation and radiative forcing of contrail cirrus". In: *Nature Communications* 9.1, p. 1824. ISSN: 2041-1723. DOI: 10.1038/s41467-018-04068-0.

Kharina, A. and Rutherford, D. (2015). "Fuel efficiency trends for new commercial jet aircraft: 1960 to 2014." In: *White paper of the International Council on Clean Transportation.*

Klima, K. (2005). "Assessment of a Global Contrail Modeling Method and Operational Strategies for Contrail Mitigation". PhD thesis. Cambridge, MA, USA: Massachusetts Institute of Technology.

Köhler, M. O., Rädel, G., Shine, K. P., Rogers, H. L., and Pyle, J. A. (2013). "Latitudinal variation of the effect of aviation NOx emissions on atmospheric ozone and methane and related climate metrics". In: *Atmospheric Environment* 64.x, pp. 1–9. ISSN: 13522310. DOI: 10.1016/j.atmosenv.2012.09.013.

Köhler, M. O., Rädel, G., Dessens, O., Shine, K. P., Rogers, H. L., Wild, O., and Pyle, J. A. (2008). "Impact of perturbations to nitrogen oxide emissions from global aviation". In: *Journal of Geophysical Research Atmospheres* 113.11, pp. 1–15. ISSN: 01480227. DOI: 10.1029/2007JD009140.

Koop, T. (2004). "Homogeneous Ice Nucleation in Water and Aqueous Solutions". In: *Zeitschrift für Physikalische Chemie* 218.11, pp. 1231–1258. ISSN: 2196-7156. DOI: 10.1524/zpch.218.11.1231.50812.

Kou, G., Lu, Y., Peng, Y., and Shi, Y. (2012). "Evaluation of classification algorithms using MCDM and rank correlation". In: *International Journal of Information Technology and Decision Making* 11.1, pp. 197–225. ISSN: 02196220. DOI: 10.1142/S0219622012500095.

Lamquin, N., Stubenrauch, C. J., Gierens, K., Burkhardt, U., and Smit, H. (2012). "A global climatology of upper-tropospheric ice supersaturation occurrence inferred from the Atmospheric Infrared Sounder calibrated by MOZAIC". In: *Atmospheric Chemistry and Physics* 12.1, pp. 381–405. ISSN: 16807316. DOI: 10.5194/acp-12-381-2012.

Lee, D. S., Fahey, D. W., Skowron, A., Allen, M. R., Burkhardt, U., Chen, Q., Doherty, S. J., Freeman, S., Forster, P. M., Fuglestvedt, J., Gettelman, A., De León, R. R., Lim, L. L., Lund, M. T., Millar, R. J., Owen, B., Penner, J. E., Pitari, G., Prather, M. J., Sausen, R., and Wilcox, L. J. (2021). "The contribution of global aviation to anthropogenic climate forcing for 2000 to 2018". In: *Atmospheric Environment* 244. ISSN: 18732844. DOI: 10.1016/j.atmosenv.2020.117834.

Lee, D. S., Pitari, G., Grewe, V., Gierens, K., Penner, J. E., Petzold, A., Prather, M. J., Schumann, U., Bais, A., Berntsen, T., Iachetti, D., Lim, L. L., and Sausen, R. (2010). "Transport impacts on atmosphere and climate: Aviation". In: *Atmospheric*

Environment 44.37, pp. 4678–4734. ISSN: 13522310. DOI: 10.1016/j.atmosenv.2009.06.005.

Lee, D. S., Allen, M. R., Cumpsty, N., Owen, B., Shine, K. P., and Skowron, A. (2023). "Uncertainties in mitigating aviation non-CO2 emissions for climate and air quality using hydrocarbon fuels". In: *Environmental Science: Atmospheres* 3.12, pp. 1693–1740. ISSN: 2634-3606. DOI: 10.1039/D3EA00091E.

Lührs, B., Linke, F., Matthes, S., Grewe, V., and Yin, F. (2021). "Climate impact mitigation potential of European air traffic in a weather situation with strong contrail formation". In: *Aerospace* 8.2, pp. 1–15. ISSN: 22264310. DOI: 10.3390/aerospace8020050.

Manen, J. van and Grewe, V. (2019). "Algorithmic climate change functions for the use in eco-efficient flight planning". In: *Transportation Research Part D: Transport and Environment* 67, pp. 388–405. ISSN: 13619209. DOI: 10.1016/j.trd.2018.12.016.

Mannstein, H., Spichtinger, P., and Gierens, K. (2005). "A note on how to avoid contrail cirrus". In: *Transportation Research Part D: Transport and Environment* 10.5, pp. 421–426. ISSN: 13619209. DOI: 10.1016/j.trd.2005.04.012.

Marla, L., Vaaben, B., and Barnhart, C. (2017). "Integrated Disruption Management and Flight Planning to Trade Off Delays and Fuel Burn". In: *Transportation Science* 51.1, pp. 88–111. ISSN: 0041-1655. DOI: 10.1287/trsc.2015.0609.

Maruhashi, J., Grewe, V., Frömming, C., Jöckel, P., and Dedoussi, I. C. (2022). "Transport patterns of global aviation NOx and their short-term O3 radiative forcing – a machine learning approach". In: *Atmospheric Chemistry and Physics* 22.21, pp. 14253–14282. ISSN: 1680-7324. DOI: 10.5194/acp-22-14253-2022.

Matthes, S., Dietmüller, S., Dahlmann, K., Frömming, C., Peter, P., Yamashita, H., Grewe, V., Yin, F., and Castino, F. (2023). "Updated algorithmic climate change functions (aCCF) V1.0A: Evaluation with the climate-response model AirClim V2.0". In: *Geosci. Model Dev. Discuss. [preprint]*. DOI: 10.5194/gmd-2023-92.

Matthes, S., Grewe, V., Dahlmann, K., Frömming, C., Irvine, E., Lim, L., Linke, F., Lührs, B., Owen, B., Shine, K., Stromatas, S., Yamashita, H., and Yin, F. (2017). "A concept for multi-criteria environmental assessment of aircraft trajectories". In: *Aerospace* 4.3. ISSN: 22264310. DOI: 10.3390/aerospace4030042.

Matthes, S., Lim, L., Burkhardt, U., Dahlmann, K., Dietmüller, S., Grewe, V., Haslerud, A. S., Hendricks, J., Owen, B., Pitari, G., Righi, M., and Skowron, A. (2021). "Mitigation of Non-CO2 Aviation's Climate Impact by Changing Cruise Altitudes". In: *Aerospace* 8.2, pp. 1–20. ISSN: 22264310. DOI: 10.3390/aerospace8020036.

Matthes, S., Lührs, B., Dahlmann, K., Grewe, V., Linke, F., Yin, F., Klingaman, E., and Shine, K. P. (2020). "Climate-optimized trajectories and robust mitigation potential: Flying ATM4E". In: *Aerospace* 7.11, pp. 1–15. ISSN: 22264310. DOI: 10.3390/aerospace7110156.

Megill, L., Deck, K., and Grewe, V. (2024). "Alternative climate metrics to the Global Warming Potential are more suitable for assessing aviation non-CO2 effects". In: *Communications Earth and Environment* 5.1. ISSN: 26624435. DOI: 10.1038/s43247-024-01423-6.

Meuser, M. M., Lührs, B., Gollnick, V., Linke, F., Matthes, S., Dietmüller, S., Baumann, S., Soler, M., Simorgh, A., Yin, F., and Castino, F. (2022). "Mitigation of aviation's climate impact through robust climate optimized trajectories in intra-European airspace". In: *33rd Congress of the International Council of the Aeronautical Sciences (ICAS)*. DOI: https://doi.org/10.15480/882.4826.

Molloy, J., Teoh, R., Harty, S., Koudis, G., Schumann, U., Poll, I., and Stettler, M. E. J. (2022). "Design Principles for a Contrail-Minimizing Trial in the North Atlantic". In: *Aerospace* 9.7, p. 375. ISSN: 2226-4310. DOI: 10.3390/aerospace9070375.

Moore, R. H., Thornhill, K. L., Weinzierl, B., Sauer, D., D'Ascoli, E., Kim, J., Lichtenstern, M., Scheibe, M., Beaton, B., Beyersdorf, A. J., Barrick, J., Bulzan, D., Corr, C. A., Crosbie, E., Jurkat, T., Martin, R., Riddick, D., Shook, M., Slover, G., Voigt, C., White, R., Winstead, E., Yasky, R., Ziemba, L. D., Brown, A., Schlager, H., and Anderson, B. E. (2017). "Biofuel blending reduces particle emissions from aircraft engines at cruise conditions". In: *Nature* 543.7645, pp. 411–415. ISSN: 0028-0836. DOI: 10.1038/nature21420.

Myhre, G., Nilsen, J. S., Gulstad, L., Shine, K. P., Rognerud, B., and Isaksen, I. S. A. (2007). "Radiative forcing due to stratospheric water vapour from CH4 oxidation". In: *Geophysical Research Letters* 34.1. ISSN: 0094-8276. DOI: 10.1029/2006GL027472.

Myhre, G. and Stordal, F. (2001). "On the tradeoff of the solar and thermal infrared radiative impact of contrails". In: *Geophysical Research Letters* 28.16, pp. 3119–3122. ISSN: 00948276. DOI: 10.1029/2001GL013193.

Ng, H. K., Sridhar, B., Grabbe, S., and Chen, N. (2011). "Cross-polar aircraft trajectory optimization and the potential climate impact". In: *2011 IEEE/AIAA 30th Digital Avionics Systems Conference*. IEEE, pp. 4–1. ISBN: 978-1-61284-798-6. DOI: 10.1109/DASC.2011.6096060.

Niklaß, M., Gollnick, V., Lührs, B., Dahlmann, K., Froemming, C., Grewe, V., and Manen, J. van (2017). "Cost-Benefit Assessment of Climate-Restricted Airspaces as an Interim Climate Mitigation Option". In: *Journal of Air Transportation* 25.2, pp. 27–38. ISSN: 2380-9450. DOI: 10.2514/1.D0045.

Niklaß, M., Grewe, V., Gollnick, V., and Dahlmann, K. (2021). "Concept of climate-charged airspaces: a potential policy instrument for internalizing aviation's climate impact of non-CO2 effects". In: *Climate Policy* 21.8, pp. 1066–1085. ISSN: 1469-3062. DOI: 10.1080/14693062.2021.1950602.

Opricovic, S. (1998). "Multicriteria Optimization of Civil Engineering Systems". PhD thesis. Belgrade: University of Belgrade.

Opricovic, S. and Tzeng, G.-H. (2004). "Compromise solution by MCDM methods: A comparative analysis of VIKOR and TOPSIS". In: *European Journal of Operational Research* 156.2, pp. 445–455. ISSN: 03772217. DOI: 10.1016/S0377-2217(03)00020-1.

Pasman, H. J., Rogers, W. J., and Behie, S. W. (2022). "Selecting a method/tool for risk-based decision making in complex situations". In: *Journal of Loss Prevention in the Process Industries* 74. ISSN: 09504230. DOI: 10.1016/j.jlp.2021.104669.

Penner, J., Lister, D., Griggs, D., Dokken, D., and McFarland, M. (1999). "IPCC Report: Aviation and the global atmosphere". In: *Cambridge University Press, UK*.

Perryman, M., Besco, L., Suleiman, C., and Lucato, L. (2022). "Ready for take off: Airline engagement with the United Nations Sustainable Development Goals". In: *Journal of Air Transport Management* 103, p. 102246. ISSN: 09696997. DOI: 10.1016/j.jairtraman.2022.102246.

Peter, P., Matthes, S., Frömming, C., Jöckel, P., Bugliaro, L., Giez, A., Krämer, M., and Grewe, V. (2025). "Influence of temperature and humidity on contrail formation regions in the general circulation model EMAC: a spring case study". In: *Atmospheric Chemistry and Physics* 25.11, pp. 5911–5934. ISSN: 1680-7324. DOI: 10.5194/acp-25-5911-2025.

Petzold, A., Khan, N. F., Li, Y., Spichtinger, P., Rohs, S., Crewell, S., Wahner, A., and Krämer, M. (2025). "Most long-lived contrails form within cirrus clouds with uncertain climate impact". In: *Nature Communications* 16.1, p. 9695. ISSN: 2041-1723. DOI: 10.1038/s41467-025-65532-2.

Petzold, A., Neis, P., Rütimann, M., Rohs, S., Berkes, F., G. J. Smit, H., Krämer, M., Spelten, N., Spichtinger, P., Nédélec, P., and Wahner, A. (2020). "Ice-supersaturated air masses in the northern mid-latitudes from regular in situ observations by passenger aircraft: Vertical distribution, seasonality and tropospheric fingerprint". In: *Atmospheric Chemistry and Physics* 20.13, pp. 8157–8179. ISSN: 16807324. DOI: 10.5194/acp-20-8157-2020.

Pletzer, J. and Grewe, V. (2024). "Sensitivities of atmospheric composition and climate to altitude and latitude of hypersonic aircraft emissions". In: *Atmospheric Chemistry and Physics* 24.3, pp. 1743–1775. ISSN: 1680-7324. DOI: 10.5194/acp-24-1743-2024.

Prather, M. J., Gettelman, A., and Penner, J. E. (2025). "Trade-offs in aviation impacts on climate favour non-CO2 mitigation". In: *Nature* 643.8073, pp. 988–993. ISSN: 0028-0836. DOI: 10.1038/s41586-025-09198-2.

Rao, P., Dwight, R., Singh, D., Maruhashi, J., Dedoussi, I., Grewe, V., and Frömming, C. (2024). "The ozone radiative forcing of nitrogen oxide emissions from aviation can be estimated using a probabilistic approach". In: *Communications Earth & Environment* 5.1, p. 558. ISSN: 2662-4435. DOI: 10.1038/s43247-024-01691-2.

Rao, P., Yin, F., Grewe, V., Yamashita, H., Jöckel, P., Matthes, S., Mertens, M., and Frömming, C. (2022). "Case Study for Testing the Validity of NOx-Ozone Algorithmic Climate Change Functions for Optimising Flight Trajectories". In: *Aerospace* 9.5, p. 231. DOI: 10.3390/aerospace9050231.

Reithmeier, C. and Sausen, R. (2002). "ATTILA: atmospheric tracer transport in a Lagrangian model". In: *Tellus B: Chemical and Physical Meteorology* 54.3, p. 278. ISSN: 1600-0889. DOI: 10.3402/tellusb.v54i3.16666.

Reutter, P., Neis, P., Rohs, S., and Sauvage, B. (2020). "Ice supersaturated regions: properties and validation of ERA-Interim reanalysis with IAGOS in situ water vapour measurements". In: *Atmospheric Chemistry and Physics* 20.2, pp. 787–804. ISSN: 1680-7324. DOI: 10.5194/acp-20-787-2020.

Rieger, V. S., Mertens, M., and Grewe, V. (2018). "An advanced method of contributing emissions to short-lived chemical species (OH and HO2): the TAGGING 1.1 submodel based on the Modular Earth Submodel System (MESSy 2.53)". In: *Geoscientific Model Development* 11.6, pp. 2049–2066. ISSN: 1991-9603. DOI: 10.5194/gmd-11-2049-2018.

Roeckner, E., Brokopf, R., Esch, M., Giorgetta, M. A., Hagemann, S., Kornblueh, L., Manzini, E., Schlese, U., and Schulzweida, U. (2006). "Sensitivity of simulated climate to horizontal and vertical resolution in the ECHAM5 atmosphere model". In: *Journal of Climate* 19.16, pp. 3771–3791. ISSN: 08948755. DOI: 10.1175/JCLI3824.1.

Roosenbrand, E., Sun, J., and Hoekstra, J. (2023). "Contrail minimization through altitude diversions: A feasibility study leveraging global data". In: *Transportation Research Interdisciplinary Perspectives* 22. ISSN: 25901982. DOI: 10.1016/j.trip.2023.100953.

Rosanka, S., Frömming, C., and Grewe, V. (2020). "The impact of weather patterns and related transport processes on aviation's contribution to ozone and methane concentrations from NOx emissions". In: *Atmospheric Chemistry and Physics* 20.20, pp. 12347–12361. ISSN: 1680-7324. DOI: 10.5194/acp-20-12347-2020.

Saez Ortuno, M. A. (2022). *Climate Impact of Hydrogen Aviation*. TU Delft, Master Thesis.

Sałabun, W., Wątróbski, J., and Shekhovtsov, A. (2020). "Are MCDA Methods Benchmarkable? A Comparative Study of TOPSIS, VIKOR, COPRAS, and PROMETHEE II Methods". In: *Symmetry* 12.9, p. 1549. ISSN: 2073-8994. DOI: 10.3390/sym12091549.

Sasaki, D. and Obayashi, S. (2005). "Efficient Search for Trade-Offs by Adaptive Range Multi-Objective Genetic Algorithms". In: *Journal of Aerospace Computing, Information, and Communication* 2.1, pp. 44–64. ISSN: 1542-9423. DOI: 10.2514/1.12909.

Schmidt, E. (1941). "Die entstehung von eisnebel aus den auspuffgasen von flugmotoren". In: *Schriften der Deutschen Akademie der Luftfahrtforschung, Verlag R. Oldenbourg, Munchen* 5.44, pp. 1–15.

Schumann, U., Mayer, B., Graf, K., and Mannstein, H. (2012). "A Parametric Radiative Forcing Model for Contrail Cirrus". In: *Journal of Applied Meteorology and Climatology* 51.7, pp. 1391–1406. ISSN: 1558-8424. DOI: 10.1175/JAMC-D-11-0242.1.

Schumann, U. (1996). "On conditions for contrail formation from aircraft exhausts". In: *Meteorologische Zeitschrift* 5.1, pp. 4–23. ISSN: 0941-2948. DOI: 10.1127/metz/5/1996/4.

Schumann, U., Baumann, R., Baumgardner, D., Bedka, S. T., Duda, D. P., Freudenthaler, V., Gayet, J.-F., Heymsfield, A. J., Minnis, P., Quante, M., Raschke, E., Schlager, H., Vázquez-Navarro, M., Voigt, C., and Wang, Z. (2017). "Properties of individual contrails: a compilation of observations and some comparisons". In: *Atmospheric Chemistry and Physics* 17.1, pp. 403–438. ISSN: 1680-7324. DOI: 10.5194/acp-17-403-2017.

Shindell, D., Bréon, F.-m., Collins, W., Fuglestvedt, J., Huang, J., Koch, D., Lamarque, J.-f., Lee, D., Mendoza, B., Nakajima, T., Robock, A., Stephens, G., Takemura, T., Zhang, H., Qin, D., Plattner, G.-k., Tignor, M., Allen, S., Boschung, J., Nauels, A., Xia, Y., Bex, V., and Midgley, P. (2013). "Anthropogenic and Natural Radiative Forcing. In: Climate Change 2013: The Physical Science Basis. Contribution of Working Group I to the Fifth Assessment Report of the Intergovernmental Panel on Climate Change". In: *Cambridge University Press, Cambridge, United Kingdom and New York, NY, USA*.

Simorgh, A., Soler, M., González-Arribas, D., Linke, F., Lührs, B., Meuser, M. M., Dietmüller, S., Matthes, S., Yamashita, H., Yin, F., Castino, F., Grewe, V., and Baumann, S. (2023). "Robust 4D climate-optimal flight planning in structured airspace using parallelized simulation on GPUs: ROOST V1.0". In: *Geoscientific Model Development* 16.13, pp. 3723–3748. ISSN: 1991-9603. DOI: 10.5194/gmd-16-3723-2023.

Simorgh, A., Soler, M., González-Arribas, D., Matthes, S., Grewe, V., Dietmüller, S., Baumann, S., Yamashita, H., Yin, F., Castino, F., Linke, F., Lührs, B., and Meuser, M. M. (2022). *A Comprehensive Survey on Climate Optimal Aircraft Trajectory Planning*. DOI: 10.3390/aerospace9030146.

Smith, D. M., Scaife, A. A., Eade, R., Athanasiadis, P., Bellucci, A., Bethke, I., Bilbao, R., Borchert, L. F., Caron, L. P., Counillon, F., Danabasoglu, G., Delworth, T., Doblas-Reyes, F. J., Dunstone, N. J., Estella-Perez, V., Flavoni, S., Hermanson, L., Keenlyside, N., Kharin, V., Kimoto, M., Merryfield, W. J., Mignot, J., Mochizuki, T., Modali, K., Monerie, P. A., Müller, W. A., Nicolí, D., Ortega, P., Pankatz, K., Pohlmann, H., Robson, J., Ruggieri, P., Sospedra-Alfonso, R., Swingedouw, D., Wang, Y., Wild, S., Yeager, S., Yang, X., and Zhang, L. (2020). "North Atlantic climate far more predictable than models imply". In: *Nature* 583.7818, pp. 796–800. ISSN: 14764687. DOI: 10.1038/s41586-020-2525-0.

Søvde, O. A., Matthes, S., Skowron, A., Iachetti, D., Lim, L., Owen, B., Hodnebrog, O., Di Genova, G., Pitari, G., Lee, D. S., Myhre, G., and Isaksen, I. S. (2014). "Aircraft emission mitigation by changing route altitude: A multi-model estimate of aircraft NOx emission impact on O3 photochemistry". In: *Atmospheric Environment* 95, pp. 468–479. ISSN: 13522310. DOI: 10.1016/j.atmosenv.2014.06.049.

Spichtinger, P., Gierens, K., Leiterer, U., and Dier, H. (2003). "Ice supersaturation in the tropopause region over Lindenberg, Germany". In: *Meteorologische Zeitschrift* 12.3, pp. 143–156. ISSN: 09412948. DOI: 10.1127/0941-2948/2003/0012-0143.

Sridhar, B., Ng, H. K., and Chen, N. Y. (2011). "Aircraft Trajectory Optimization and Contrails Avoidance in the Presence of Winds". In: *Journal of Guidance, Control, and Dynamics* 34.5, pp. 1577–1584. ISSN: 0731-5090. DOI: 10.2514/1.53378.

Staples, M. D., Malina, R., Suresh, P., Hileman, J. I., and Barrett, S. R. (2018). "Aviation CO2 emissions reductions from the use of alternative jet fuels". In: *Energy Policy* 114, pp. 342–354. ISSN: 03014215. DOI: 10.1016/j.enpol.2017.12.007.

Stenke, A., Grewe, V., and Ponater, M. (2008). "Lagrangian transport of water vapor and cloud water in the ECHAM4 GCM and its impact on the cold bias". In: *Climate Dynamics* 31.5, pp. 491–506. ISSN: 09307575. DOI: 10.1007/s00382-007-0347-5.

Stevenson, D. S. and Derwent, R. G. (2009). "Does the location of aircraft nitrogen oxide emissions affect their climate impact?" In: *Geophysical Research Letters* 36.17, pp. 4–8. ISSN: 00948276. DOI: 10.1029/2009GL039422.

Stevenson, D. S., Doherty, R. M., Sanderson, M. G., Collins, W. J., Johnson, C. E., and Derwent, R. G. (2004). "Radiative forcing from aircraft NOx emissions: Mechanisms and seasonal dependence". In: *Journal of Geophysical Research D: Atmospheres* 109.17. ISSN: 01480227. DOI: 10.1029/2004JD004759.

Teoh, R., Schumann, U., Majumdar, A., and Stettler, M. E. (2020). "Mitigating the Climate Forcing of Aircraft Contrails by Small-Scale Diversions and Technology Adoption". In: *Environmental Science and Technology* 54.5, pp. 2941–2950. ISSN: 15205851. DOI: 10.1021/acs.est.9b05608.

Wallace, J. and Gutzler, D. (1981). "Teleconnections in the geopotential height field during the northern hemisphere winter." In: *Mon. Weather Rev.* 109, pp. 784–812.

Wang, Z. and Rangaiah, G. P. (2017). "Application and Analysis of Methods for Selecting an Optimal Solution from the Pareto-Optimal Front obtained by Multiobjective Optimization". In: *Industrial & Engineering Chemistry Research* 56.2, pp. 560–574. ISSN: 0888-5885. DOI: 10.1021/acs.iecr.6b03453.

Wild, O., Prather, M. J., and Akimoto, H. (2001). "Indirect long-term global radiative cooling from NOx emissions". In: *Geophysical Research Letters* 28.9, pp. 1719–1722. ISSN: 00948276. DOI: 10.1029/2000GL012573.

Wilhelm, L., Gierens, K., and Rohs, S. (2022). "Meteorological Conditions that Promote Persistent Contrails". In: *Applied Sciences (Switzerland)* 12.9. ISSN: 20763417. DOI: 10.3390/app12094450.

Williams, V., Noland, R. B., and Toumi, R. (2003). "Air transport cruise altitude restrictions to minimize contrail formation". In: *Climate Policy* 3.3, pp. 207–219. ISSN: 1469-3062. DOI: 10.3763/cpol.2003.0328.

Woollings, T., Czuchnicki, C., and Franzke, C. (2014). "Twentieth century North Atlantic jet variability". In: *Quarterly Journal of the Royal Meteorological Society* 140.680, pp. 783–791. ISSN: 0035-9009. DOI: 10.1002/qj.2197.

Yamashita, H., Grewe, V., Jöckel, P., Linke, F., Schaefer, M., and Sasaki, D. (2016). "Air traffic simulation in chemistry-climate model EMAC 2.41: AirTraf 1.0". In: *Geoscientific Model Development* 9.9, pp. 3363–3392. ISSN: 19919603. DOI: 10.5194/gmd-9-3363-2016.

Yamashita, H., Yin, F., Grewe, V., Jöckel, P., Matthes, S., Kern, B., Dahlmann, K., and Frömming, C. (2020). "Newly developed aircraft routing options for air traffic simulation in the chemistry–climate model EMAC 2.53: AirTraf 2.0". In: *Geoscientific Model Development* 13.10, pp. 4869–4890. ISSN: 19919603. DOI: 10.5194/gmd-13-4869-2020.

Yamashita, H., Yin, F., Grewe, V., Jöckel, P., Matthes, S., Kern, B., Dahlmann, K., and Frömming, C. (2021). "Analysis of aircraft routing strategies for north atlantic flights by using airtraf 2.0". In: *Aerospace* 8.2, pp. 1–19. ISSN: 22264310. DOI: 10.3390/aerospace8020033.

Yin, F., Grewe, V., Castino, F., Rao, P., Matthes, S., Dahlmann, K., Dietmüller, S., Frömming, C., Yamashita, H., Peter, P., Klingaman, E., Shine, K. P., Lührs, B., and Linke, F. (2023). "Predicting the climate impact of aviation for en-route emissions: the algorithmic climate change function submodel ACCF 1.0 of EMAC 2.53". In: *Geoscientific Model Development* 16.11, pp. 3313–3334. ISSN: 1991-9603. DOI: 10.5194/gmd-16-3313-2023.

Yin, F., Grewe, V., Frömming, C., and Yamashita, H. (2018a). "Impact on flight trajectory characteristics when avoiding the formation of persistent contrails for transatlantic flights". In: *Transportation Research Part D: Transport and Environment* 65, pp. 466–484. ISSN: 13619209. DOI: 10.1016/j.trd.2018.09.017.

Yin, F. and Rao, A. G. (2020). "A review of gas turbine engine with inter-stage turbine burner". In: *Progress in Aerospace Sciences* 121, p. 100695. ISSN: 03760421. DOI: 10.1016/j.paerosci.2020.100695.

Yin., F., Grewe., V., Manen, J. v., Matthes., S., Yamashita., H., Linke., F., and Lührs, B. (2018b). "Verification of the ozone algorithmic climate change functions for predicting the short-term NOx effects from aviation en-route". In: *Proceedings of the International Conferenceon Research in Air Transportation (ICRAT)*. Barcelona, Spain.

Zhou, X., Dhomse, S. S., Feng, W., Mann, G., Heddell, S., Pumphrey, H., Kerridge, B. J., Latter, B., Siddans, R., Ventress, L., Querel, R., Smale, P., Asher, E., Hall, E. G., Bekki, S., and Chipperfield, M. P. (2024). "Antarctic Vortex Dehydration in 2023 as a Substantial Removal Pathway for Hunga Tonga-Hunga Ha'apai Water Vapor". In: *Geophysical Research Letters* 51.8. ISSN: 0094-8276. DOI: 10.1029/2023GL107630.

Acknowledgments

Leafing through this thesis feels like time-travelling through years of research, which have enriched me in so many different ways. I remember how excited I was at the idea of meeting and collaborating with such remarkable researchers, as I arrived in Delft to start my PhD. I was right to be that thrilled: I have indeed had the privilege of getting to know countless extraordinary people. And in the end, this dissertation would have never been printed without the invaluable contribution and support of all those that joined me in this journey. I will try to acknowledge them here, knowing that this list can never be complete.

My first words of gratitude go to my supervisors, Feijia Yin and Volker Grewe, for giving me the opportunity to explore such an exciting topic. This thesis is the fruit of many hours of discussions and several rounds of manuscript revisions: I truly appreciate the attention and time that you dedicated to this project. No matter the distance between my workplace and yours (just a few meters from Feijia's, about 750 km from Volker's), you were both present at every step of the process. Thank you for your valuable guidance and encouragement.

A special thank you also goes to Hiroshi Yamashita. I cannot express how grateful I am for your constant support from the very beginning of this journey, and for developing and adapting AirTraf towards the resolution of multi-objective optimization problems. Thank you for sharing your expertise, and for always being available to discuss the modelling approach in all its details. I would also like to acknowledge the contribution of the other coauthors of the papers included in this dissertation. I met most of these exceptional colleagues when I joined the FlyATM4E team at the beginning of my PhD trajectory: Manuel Soler and Abolfazl Simorgh from Universidad Carlos III de Madrid; Sigrun Matthes, Simone Dietmüller, Sabine Baumann, Maximilian Mendiguchia Meuser, Florian Linke, and Benjamin Lührs from the Deutsches Zentrum für Luft- und Raumfahr (DLR). I learnt so much from our collaboration, and I will be forever grateful to all of you. Lastly, the final segment of this journey has been enriched by the close collaboration with Katarina Grubbe Hildebrandt. Thank you for sharing your extensive knowledge of the IAGOS datasets since you joined the team as a MSc student and, later on, for becoming such a great office mate. I know that all the knitting tips you gave me will be very useful when I give this craft a second chance!

I have been incredibly lucky to be surrounded by so many wonderful colleagues and students at TU Delft. All of them contributed directly or indirectly to the completion of this dissertation. In particular, I would like to thank: Vincent, for the brilliant ideas shared during our stimulating conversations, and for the valuable feedback that helped improve my description of the CONTRAIL submodule in this thesis; my office mate, Anique, for cheering for me through all ups and downs, and helping me with the translation of the Dutch summary opening this thesis; Pratik, for the many discussions about our research projects that enriched this thesis, as well as for the engaging chats about politics and jazz; Jakob, for offering many useful programming tips, and for the

generosity and attention shown in and outside the office; Jin, for the interesting conversations on the impact of aviation NO_x emissions, and for his humour; Monica and Patrick, for the warm welcome during my visit to the DLR institute in Oberpfaffenhofen; Amy, for becoming my kindest neighbour by moving to Scheveningen, and for making so many memories more special; Kathrin, for cheering me up with snacks and sweets when I was stuck with a high fever at the conference hotel; Harjot, for the moments shared travelling between Delft and The Hague, and during a memorable summer school; Jurriaan, for the laughs at the TAC and EGU conferences; Irina, for hosting an unforgettable barbecue; Camilo, for involving me in his quest through Tuscany's historical archives; Rebekka, for turning painting the walls of her new house into such a fun and memorable day; Colin, for welcoming me in the ANCE group as my first office mate; Wessel, Angela and Ahmad, for their creativity and remarkable findings shared during our meetings, while working on their MSc thesis; the brilliant BSc students I had the privilege to coach, as they followed the DSE (*Design Synthesis Exercise*) and *Test, Analysis and Simulation* courses; Lisette, Marloes, Marc and Jose, for clarifying and taking care of every administrative obstacle; the HPC12 and DelftBlue support teams, which quickly answered my emails whenever a technical issue became an obstacle to run my simulations; Heather, for all the tips and reviewing my data management plan; Margaret, for the key recommendations as a Graduate School teacher and career advisor; Roberto, for the endless fun while attending the Paris Air Show; Thymen, Clémentin and Manas, for the fresh ideas and results we discussed during and after many climate group meetings; Anandini, for lifting the office mood with the funniest jokes; Andrei and Josephine, for the daily lunch memes; Flavio, Salil, Bieke, Renatto, Luccas, Esther and Qian, for the interesting conversations during countless lunches and coffee breaks. Lastly, a big thank you goes to the members of the BeCoM team, for the knowledge they shared and the fruitful discussions on modelling and avoiding the formation of contrails.

Outside the office, there have been so many generous people who have helped me overcome the challenges I met along the way. Among them, my volleyball teammates at Kratos hold a special place, as they welcomed me when I first arrived in Delft. Our trainings and matches have so often been an antidote to the physical and mental tension accumulated at the end of long workdays. I am so thankful to all of you for the fun we had playing together.

I am forever grateful to Mirabel and to all the members of the meditation group that she leads every Monday evening. You have inspired one of the propositions accompanying this thesis, teaching me precious lessons about the importance of silence, attention and trust.

I would have never chosen this path, if it wasn't for the amazing teachers I was lucky to encounter during my school years. In particular, I wish to thank Daniela and my high school professors of Physics and Mathematics, for the contagious passion and enthusiasm that stimulated my curiosity for these subjects.

No matter how far they lived from Delft, so many friends have made me feel their warm support during this journey. With Margherita, Sara, Yang, Mari, Sonia, and of course my paranymphs Louise and Ombretta, I have shared houses, adventures, good and bad days, and lived so many unforgettable moments. Thank you for being such great listeners in difficult times, and the best at finding reasons to celebrate and ways to have fun.

Well before I started working on this thesis, my family has played a fundamental role in paving the way for this achievement. It became a reality only because of the unconditional and constant support shown by my grandparents Umberto, Silvana, Elvio and Alba, my parents Patrizia and Rino, and my sister Chiara. No physical distance has ever made me feel distant from you.

When you start a PhD, they tell you to be ready for unexpected turns of events. The luckiest of them has definitely been meeting Luca: I cannot begin to explain the role you have played in the completion of this thesis, and how you supported and encouraged me day after day. I am so grateful for how you keep my passion for science alive with your endless excitement for peculiar clouds, weirdly behaving animals, archaeological tools, and any other unexpected wonder that we find while spending time in nature. Thank you for showing me the magic hidden in everyday life, that reveals itself when you observe with curious eyes and an open mind.

Federica,
Bussum, July 2026

Curriculum Vitæ

Federica Castino

25 February 1995 — Born in Sanremo, Italy.

Education

2020-2024 — **Doctor of Philosophy (PhD) in Aerospace Engineering**
Delft University of Technology
Delft, the Netherlands
Thesis: Eco-efficient aircraft trajectories to reduce aviation non-CO_2 climate effects under varying atmospheric conditions
Promotors: Prof. dr. V. Grewe
Dr. F. Yin

2018-2020 — **Master of Science (MSc) in Climate Physics**
Utrecht University
Utrecht, the Netherlands

2014-2017 — **Bachelor of Science (BSc) in Physics**
Università degli Studi di Torino
Turin, Italy

2009-2014 — **Secondary Education**
Liceo Scientifico A. Aprosio
Ventimiglia, Italy

List of Publications

In this thesis

1. **Castino, F.**, Yin, F., Grewe, V., Yamashita, H., Matthes, S., Dietmüller, S., Baumann, S., Soler, M., Simorgh, A., Mendiguchia Meuser, M., Linke, F., and Lührs, B., *Decision-making strategies implemented in SolFinder 1.0 to identify eco-efficient aircraft trajectories: application study in AirTraf 3.0,* Geoscientific Model Development 17(9), 4031–4052, DOI: 10.5194/gmd-17-4031-2024, 2024.

2. **Castino, F.**, Grewe, V., Yamashita, H., Hildebrandt, K.G., Yin, F.: *Seasonal variability and weather pattern dependency of contrail avoidance in the North Atlantic,* under review.

3. **Castino, F.**, Yin, F., Grewe, V., Soler, M., Simorgh, A., Yamashita, H., Matthes, S., Baumann, S., Dietmüller, S., Linke, F., and Lührs, B., *Seasonal Variability of Aircraft Trajectories reducing NO_x-climate Impacts under a Multitude of Weather Patterns,* 11th SESAR Innovation Days, 2021.

Other publications

1. Simorgh, A., Soler, M., González-Arribas, D., Matthes, S., Grewe, V., Dietmüller, S., Baumann, S., Yamashita, H., Yin, F., **Castino, F.**, Linke, F., Lührs, B., and Meuser, M. M., *A Comprehensive Survey on Climate Optimal Aircraft Trajectory Planning,* Aerospace, 9(3), 146, DOI: 10.3390/aerospace9030146, 2022.

2. Meuser, M. M., Lührs, B., Gollnick, V., Linke, F., Matthes, S., Dietmüller, S., Baumann, S., Soler, M., Simorgh, A., Yin, F., and **Castino, F.**, *Mitigation of aviation's climate impact through robust climate optimized trajectories in intra-European airspace,* 33rd Congress of the International Council of the Aeronautical Sciences (ICAS). DOI: 10.15480/882.4826, 2022.

3. Yin, F., Grewe, V., **Castino, F.**, Rao, P., Matthes, S., Dahlmann, K., Dietmüller, S., Frömming, C., Yamashita, H., Peter, P., Klingaman, E., Shine, K. P., Lührs, B., and Linke, F. *Predicting the climate impact of aviation for en-route emissions: the algorithmic climate change function submodel ACCF 1.0 of EMAC 2.53.* Geoscientific Model Development, 16(11), 3313–3334, DOI: 10.5194/gmd-16-3313-2023, 2023.

4. Simorgh, A., Soler, M., González-Arribas, D., Linke, F., Lührs, B., Meuser, M. M., Dietmüller, S., Matthes, S., Yamashita, H., Yin, F., **Castino, F.**, Grewe, V., and Baumann, S., *Robust 4D climate-optimal flight planning in structured airspace using parallelized simulation on GPUs: ROOST V1.0,* Geoscientific Model Development 16(13), 3723–3748, DOI: 10.5194/gmd-16-3723-2023, 2023.

5. Dietmüller, S., Matthes, S., Dahlmann, K., Yamashita, H., Simorgh, A., Soler, M., Linke, F., Lührs, B., Meuser, M. M., Weder, C., Grewe, V., Yin, F., and **Castino, F.**, *A Python library for computing individual and merged non-CO2 algorithmic climate change functions: CLIMaCCF V1.0,* Geoscientific Model Development 16(15), 4405–4425, DOI: 10.5194/gmd-16-4405-2023, 2023.

6. Simorgh, A., Soler, M., Matthes, S., Dietmüller, S., Yamashita, H., **Castino, F.**, Yin, F., *Robust 4D climate-optimal aircraft trajectory planning under weather-induced uncertainties: Free-routing airspace,* Transportation Research Part D: Transport and Environment, 131, DOI: 10.1016/j.trd.2024.104196, 2024.

7. Simorgh, A., Soler, M., **Castino, F.**, Yin, F., Cerezo-Magaña, M., *Concept of robust climate-friendly flight planning under multiple climate impact estimates,* Transportation Research Part D: Transport and Environment, 131, DOI: 10.1016/j.trd.2024.104215, 2024.

8. Hildebrandt, K. G., **Castino, F.**, Meijer, V., and Yin, F., *Variability of ice supersaturated regions at flight altitudes: evaluation of ERA5 reanalysis using IAGOS in situ measurements,* EGUsphere [preprint], DOI:10.5194/egusphere-2025-3048, 2025.

